# On the Origin of the Extracellular Potential in the Nucleus Laminaris of the Barn Owl

D i s s e r t a t i o n

zur Erlangung des akademischen Grades

d o c t o r r e r u m n a t u r a l i u m

(Dr. rer. nat.)

im Fach Biologie

eingereicht an der
Mathematisch-Wissenschaftlichen Fakultät I
der Humboldt-Universität zu Berlin

von
**M.Sc. Paula T. Kuokkanen**

Präsident der Humboldt-Universität zu Berlin:
Prof. Dr. Jan-Hendrik Olbertz

Dekan der Mathematisch-Wissenschaftlichen Fakultät I:
Prof. Dr. Andreas Herrmann

Gutachter:
1. Prof. Dr. Catherine E. Carr
2. Prof. Dr. Richard Kempter
3. Prof. Dr. Hermann Wagner

**Tag der mündlichen Prüfung:** 07.03.2012

*Dedicated to my dear Anja.*
*Bleib immer eine Barfüsslerin.*

## Abstract

The barn owl is a good night hunter and mainly localizes the prey with its auditory system. The auditory localization in the horizontal plane, based on interaural time differences, depends on the auditory brainstem circuit consisting of nucleus magnocellularis (NM) and nucleus laminaris (NL). An extracellular field potential (EFP), named neurophonic, can be recorded in the NL. It has a very high temporal precision of below 10 microseconds and replays the stimulating sound up to 9 kHz.

In this thesis I study how an EFP with such a precision can be generated. Furthermore, what can we learn about the system and about the origin of the neurophonic in NL from these recordings? The answers will help connecting the neural activity to the EFP also in general.

Firstly, hundreds of sources, all firing with a high rate and in a highly phase-locked manner, are needed to generate the neurophonic in NL. The number of the neurons in NL and the magnitude of their output currents are not high enough to alone give rise to the neurophonic. The majority of the neural sources conveys the input from NM to NL, i.e., the currents from the nodes of Ranvier in the afferent axons from NM, and the synaptic currents to the dendrites of the NL neurons.

Furthermore, the neurophonics in response to monaural stimulation sum up linearly and predict accurately the neurophonics in response to binaural stimulation. This implies that the non-linear response of the NL neurons usually cannot be detected in the neurophonic, but that there might be a minor contribution from a single NL neuron when in the immediate vicinity of the electrode.

All in all, the neurophonic in the barn owl's NL seems to reflect the inputs to the nucleus, whereas usually the output is well represented in the EFP. Even in the homologue nuclei in chick and mammals the neurophonic is thought to reflect the output instead of the input. Thus, the exceptionality of the barn owl might be needed for the high precision in its NL.



Keywords: Auditory brainstem, Auditory localization, Barn owl, Modeling

## Zusammenfassung

Schleiereulen sind gute Nachtjäger und finden ihre Beute vor allem durch den Hörsinn. Die auditorische Lokalisierung in der horizontalen Ebene basiert dabei auf interauralen Zeitdifferenzen. Diese werden im Hirnstamm durch das Netzwerk von nucleus magnocellularis (NM) und nucleus laminaris (NL) in Orte umkodiert. Im NL kann ein extrazelluläres Potential (EP), das Neurophonpotential (NP) gemessen werden. Dieses hat eine erstaunliche zeitliche Präzision von unter 10 Mikrosekunden, und spiegelt den für die Stimulation benutzten Ton bis zu Frequenzen von 9 kHz wider.

Wie kann eine solche Präzision erzeugt werden, und was kann man über den Ursprung des Potentials in dieser neuronalen Struktur lernen? Um diese Fragen zu klären, studiere ich in vivo gemessene NPs. Dadurch kann in Zukunft die Verbindung von neuronaler Aktivität und EP besser verstanden werden.

Hunderte neuronale Stromquellen, die alle kohärent mit einer hohen Feuerrate aktiv sind, sind nötig, um ein solches NP zu erzeugen. Dabei sind Anzahl und Stromstärke der Neuronen im NL nicht ausreichend, um das NP zu erzeugen. Der Hauptanteil der Quellen besteht aus den Signalen, die den Input des NL formen: die Ströme der Ranvierschen Schnürringe entlang der Axone aus dem NM, sowie die synaptischen Ströme zu den Dendriten von NL Neuronen.

Weiterhin können NPs, die als Antwort auf monaurale Stimulierung aufgenommen wurden, linear addiert werden, um die Antwort auf binaurale Stimulation zuverlässig vorherzusagen. Leichte Abweichungen von der Vorhersage könnten damit erklärt werden, dass einzelne, sehr nah an der Elektrode befindliche Neurone nichtlinear zum NP beitragen.

Im Gegensatz zu anderen bisher untersuchten neuronalen Strukturen – auch homologer Hirnregionen – spiegelt das NP der Schleiereule Eingangs- statt Ausgangssignale wider. Dieser strukturelle Unterschied könnte erklären, wieso das Schleiereulengehirn höhere Genauigkeit erreicht, als das anderer Tiere.



Schlagworte: Auditorisches Hirnstamm, Hörlokalisierung, Schleiereule, Modellierung

# Contents

# 1. Introduction

The projection of the world in our brain is shared by several physiological and computational neuronal maps. One of these maps relates to the space around us, as reflected by the auditory input we receive. In other words, the auditory input gives us important cues about what happens where in our environment. In the animalkind, one of the specialists in sound localization is the barn owl. This night predator can localize its prey with little visual input, i.e., mainly based on the auditory input, with accuracy of few degrees. The neural correlates of this process acquire, and have been shown to have, a temporal precision finer than 20 microseconds. This accurary is one of the highest found among neural systems, which makes the owl an excellect system of studying temporal precision. It is a challenge to understand how the brain represents such precise temporal events. One of the most intriguing questions is how such representations can be achieved despite a large variability at all levels of processing.

The basics of the underlying mechanism of the sound localization in the barn owl were already discovered over three decades ago. The horizontal localization of a sound relies on the network formed by nucleus magnocellularis (NM) and nucleus laminaris (NL) in the brainstem of the birds, and it is based on the relative time difference that a sound has upon arrival to the ears (interaural time difference, ITD). For example, when the ears of the owl are stimulated with a pure tone, the neural activity in both aforementioned nuclei is locked to the stimulus tone such that a neuron will fire an action potential only in a certain phase of the stimulus tone, but not necessarily every cycle of the tone. This mechanism called phase-locking is realized in these nuclei up to exceptionally high frequencies (9 kHz). Furthermore, not only the activity of the cells is phase-locked, but also the extracellular potential, representing the activity of an ensemble of neurons, is highly correlated with the stimulus sound. Replayed in a loud-speaker, the extracellular potential sounds very much like the input sound, and thus it has been named the 'neurophonic' potential.

In this thesis I address the question of how the neurophonic potential in NL is generated. It has at least three main spectral components (low: $< 2$ kHz or $< 1$ kHz and $1 - 2$ kHz, middle: $2 - 3$ kHz and high: $> 3$ kHz), and my studies aim at revealing their origin. My hypothesis is that axons originating from the NM neurons and innervating NL are the origin of the high-frequency component, and that the activity of the NL neurons corresponds to the sub-dominant low-frequency component. I address this question by analyzing neurophonic recordings as well as by computational and mathematical modeling of extracellular potentials.

In chapters 2 and 3 I introduce the basic properties of the phenomena studied in this thesis, namely the neural correlates of auditory localization in the barn owl and the extracellular field potentials (EFPs). The chapter 2 starts with mechanisms of ITD detection and advances to the physiology of the barn owl auditory system. I concentrate especially on the high-frequency region of NL. The chapter 3 focuses on the EFP and on what is known about the neurophonic potential and its speciality with respect to other EFPs. I also describe shortly the modeling methods I use to generate the neurophonic computationally and discuss gaps of knowledge in the field.

Chapters 4 to 6 describe the results of this thesis. To test the hypothesis about the origin of the neurophonic potential, several aspects of this potential were analysed. In chapter 4, I present an advanced analysis of *in-vivo* data in response to monolateral acoustic stimulation with tones, numerical simulations of the neurophonic potential, and analytical results. I describe the neurophonic as an inhomogeneous Poisson process with a periodic firing rate that is convolved with a generic spike wave form. With the help of the model, I show how the signal-to-noise ratio (SNR) of the neurophonic potential depends on the number of independent sources generating the potential, their mean activity measured by the firing

rate, as well as the phase-locking of the action potentials. I show that several hundreds of independent sources are needed to generate such an SNR as found in the data. I argue that these sources are mainly related to the input to NL (pre-synaptic activity in NL). I also argue that the output from NL (post-synaptic activity) alone is not enough to produce such an SNR, and that the output has a minor role in the generation of the neurophonic potential.

In the 5th chapter I analyze responses to monaural and binaural tone stimulation. Based on my previous results, I assume that the responses to monolateral stimulation of each side are independent. Thus, linear summation of monaural responses should predict the binaural responses. I predict analytically with a high accuracy both the phase-locked response features and the features that are not phase-locked. In particular, I show that the ITD tuning, the magnitude and the phase of the neurophonic can be predicted by the sum of the monaural responses with the phase shift corresponding to the ITD. This supports the hypothesis that the neurophonic reflects mainly the inputs to NL. I also show that only few deviations from the linear prediction, possibly reflecting the post-synaptic activity in the NL, can be detected in the neurophonic.

In chapter 6 I analyze the shape of the neurophonic spectrum. I show that mainly the average level of the spectrum changes between the spontaneous activity and the driven responses and that changes in the shape of the spectrum are small. The minor changes indicate that the NL neurons' activity induces spectral changes in a narrow frequency band usually situated at low frequencies ($< 1$ kHz). The activity in the NM axons has broader effects across the frequencies. There is an overall increase of the spectum with the activation of the NM axons, with a broad peaks at $1 - 2$ kHz and at $3 - 4$ kHz. These results support the hypothesis that the generative mechanism of the neurophonic is the input to NL, whereas the NL neurons only play a minor role. The results also support the hypothesis that the NL neurons underlay the low-frequency component observed at about $< 1$ kHz.

The 7th chapter is a general discussion, setting the findings of previous chapters to a broader context. Also further open questions are discussed.

The appendices A and B explain in more detail some of the mathematical analysis, as well as the electrophysiological techniques used to record neurophonic.

In summary, in this thesis I study the origin of the neurophonic potential in the nucleus laminaris in the auditory brainstem of the barn owl. With my findings I contribute to the understanding of the fine temporal processing of the brain and more generally to the understanding of the summation of neural cotributions to an extracellular field potential.

# 2. Sound Localization in the Barn Owl

The ability of the brain to find the direction of a sound source is called auditory localization or sound localization. This chapter is a short introduction to sound localization, especially in the barn owl. I start with the mechanisms of auditory localization in general, and advance to the physiology of the barn owl's auditory system. I concentrate on the regions processing the temporal information of the high-frequency sounds for two main reasons. Firstly, because the electrophysiological data analyzed in this thesis is from a region processing high-frequency sounds, and, secondly, because the temporal fine structure of the sounds are of outmost importance to the neural processing in auditory localization.

## 2.1. Cues and Mechanism for Sound Localization

The owls are night predators - thus, despite them having excellent night vision (Harmening et al., 2007), the auditory localization of prey is essential for survival. Their ability of auditory localization is stunning, making the auditory system of the owl an interesting subject of research. The barn owl is specialized in auditory localization in relatively high frequencies (up to 10 kHz), and is thus well adapted in localizing the vocalizations of its prey (Payne, 1971).

### 2.1.1. Differences in time and intensity

There are several changes happening to a sound waveform as it arrives to both ears (see Fig. 2.1). Depending on the location of the sound source, there is a relative delay in the arrival of the sound to the

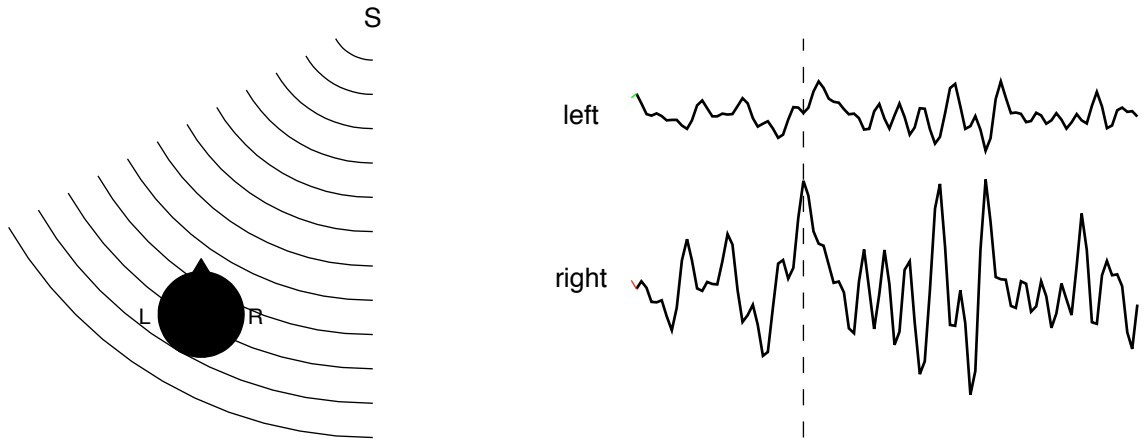


Figure 2.1.: Interaural time and intensity differences. I illustrate a situation in which a sound source $s$ is located at the rigth hand side of the head. Compared to the sound arriving at the right ear, the sound on the left ear is delayed (due to a longer distance) as well as attenuated (due to the shadow of the head as well as due to the shape of the outer ear). From Arthur (2002).

ear which is farther away from the sound source, resulting in an *interaural time difference* (ITD). Also the amplitude of the sound is smaller on the ear which is shadowed by the head, resulting in an *interaural intensity difference* (IID) (Moiseff, 1989a;b; Arthur, 2004). Furthermore, the asymmetric shape of the external ears (pinnae) changes the spectrum of sounds before they enter the ear canal. For example in humans, the pinnae are asymmetric with respect to front-back and up-down, allowing us to localize the elevation of a source with respect to the horizontal plane. In owls, the ears are furthermore asymmetric with respect to each other, the left ear is directed below and the right ear above the horizontal plane (Norberg, 1977; Knudsen and Konishi, 1979).

The brains of different animals uses the aforementioned cues (ITD, IID and spectral cues) for the sound localization in different combinations. The set of cues used depends much on the hearing range of the species and the neurophysiology of their auditory system. For example in the human, low-frequency tones ($< 800$ Hz) are localized mainly based on the time differences in the carrier of a tone, whereas at high frequencies ($> 1600$ Hz) the IID and the spectral cues, as well as the time differences in the envelope of the tone play the most important role (Blauert, 1997; a.o.).

In the barn owl, the ITDs are used solely to localize the tones in the horizontal plane independent of the frequency of the stimulus (Knudsen and Konishi, 1979; Coles and Guppy, 1988), while the IID is used for the vertical localization (elevation) (Payne, 1971; Moiseff, 1989a). Such a strict division, combined with the ability to use ITDs at high frequencies, is yet another reason to use the barn owl as a model system.

In what follows, I introduce the mechanism of ITD detection at high stimulus frequencies ($3-10$ kHz) in the barn owl. After showing *how* the task at hand can be solved, I advance to introduce the *neural components and circuitry* that are involved in performing the task. I review shortly the anatomy and the physiology of the auditory brainstem of the barn owl, focusing in the cochlear *nucleus magnocellularis* (NM) and the *nucleus laminaris* (NL) forming the circuit to detect the ITDs. From now on, NL refers to NL in the owl, unless explicitly stated otherwise.

### 2.1.2. Mechanism of ITD detection: Jeffress model

One of the first models introducing a possible mechanism to neurally implement ITD detection was proposed by Jeffress (1948) (Fig. 2.2), prior to any physiological or anatomical studies on avian or mammal auditory systems performing the auditory localization. Even more astonishing is the fact that the prerequisites of the model are fulfilled in barn owl auditory brainstem much like they were originally proposed.

In the Jeffress model, there are three general assumptions about the neural components and signals making the ITD detection possible: 1) Monaural channels (e.g. axons) that originate from the cochlear nuclei convey temporal information about the stimulus waveform in the spike times, and these axons converge on a binaural nucleus. 2) Binaural neurons act as coincidence detectors, i.e., they release action potentials (spikes) only if they receive coincident excitatory input from both monaural channels, i.e., via the afferent axons. 3) Each binaural neuron is tuned to a particular best ITD. The tuning can be achieved by afferent axons working as delay lines, running from facing sided to opposite directions through the binaural nucleus. Thus, the binaural neurons form a mapping of the (horizontal) space, based on ITDs (Fig. 2.2) (Jeffress, 1948; Joris et al., 1998; a.o.).

The prerequisites of the Jeffress model are fulfilled in the high-frequency region ($3-10$ kHz) of NL in barn owl (Knudsen and Konishi, 1978a; Moiseff and Konishi, 1981; Konishi et al., 1985; Takahashi and Konishi, 1986; Proctor and Konishi, 1997), which I will describe in detail in the next section. However, in the low frequency region ($< 2$ kHz) of the owl and in corresponding nuclei of chicks and mammals only some of the prerequisites of the Jeffress model are met. Hence, it has been argued that the unifying principle of the ITD detection across animals is not fully described by the the Jeffress model but rather by an optimal coding principle (McAlpine, 2005; Harper and McAlpine, 2004).

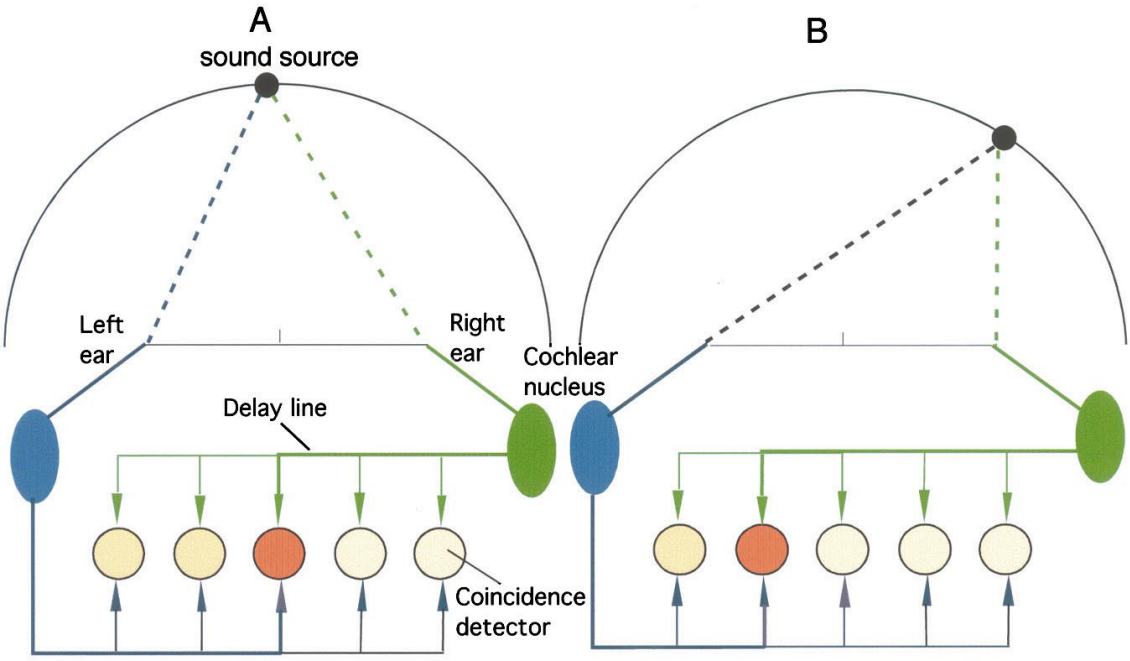


Figure 2.2.: Jeffress model. The axon bundles from left and right ears (blue and green arrow-lines) convey the neuronal activity. They run in parallel (here horizontally) forming delay lines and make synaptic contacts (marked by arrows) to neurons (white and red spheres). The neurons act as coincidence detectors. Thus, the firing rate is maximal for coincident stimuli from both sides and varies continuously with the stimulus angle (A and B show two different stimulus angles). *A:* When the sound source is located directly ahead, the delays to the right ear and to the left ear are equal. The neuron receiving coincident input (here in the middle) has a high firing rate. *B:* If the sound source shifts more to the rigth-hand side, the delay to the left ear will be longer, and thus a different neuron will become active. From Konishi (2000).

## 2.2. Interaural Time Difference Detection in the Barn Owl

The barn owl auditory brainstem (especially NL) can detect interaural time differences with microsecond precision, which corresponds to a behavioral precision of 1.5° in the direction of the head (Knudsen et al., 1979). How are such small time differences detectable in the neural level? Here I introduce the physiological properties of the barn owl auditory system that are though to enable this precision.

### 2.2.1. From outer ear to auditory nerve – from sound waves to spikes

The sound waves are mechanically filtered first by the facial ruff, then by the earflaps (outer ear) and the ear canal. The spectral transformation of the sound from a specific location due to this filtering is called *head-related transfer function* (HRTF). Then the sound waves are conveyed through the ear canal to the papilla where the basilar membrane converts sound waves to a neural representation in frequency space.

Because of the asymmetry of owl's outer ears (Norberg, 1977; Knudsen and Konishi, 1979), also the spectral changes (including attenuation) are different for each ear, even if the sound source is right

ahead[1]. This asymmetry affects mostly the vertical axis, and it results in a subsequent asymmetry in the internal representation of the sound intensities depending on the location of the sound source. Thus, the intensity cue (IID) is used for vertical localization (Payne, 1971; Moiseff, 1989a), while the ITD is used only for the horizontal localization at all biologically relevant frequencies (3 kHz $\leq f \leq$ 10 kHz (Knudsen and Konishi, 1979; Coles and Guppy, 1988)). The barn owl does hear and localize even higher frequencies ($\leq$ 13 kHz (Dyson et al., 1998)), but not quite as well as compared to most relevant frequencies (Knudsen and Konishi, 1979).

#### Basilar membrane: frequency representation

The sounds are transformed from mechanical movement to neural signals by the hair cells on the basilar membrane in the papilla of the birds, the equivalent of the cochlea of mammals. Each hair cell is each tuned to a small range of frequencies. The frequency eliciting a response at a specific location of the basilar membrane with the lowest sound pressure level is called the *characteristic frequency (CF)* of this location. The frequency tuning at each location is typically sharp. The division of CFs along the basilar membrane is such that the high sound frequencies are transformed to neural activity in the basal end of the basilar membrane; the lower frequencies continue towards its apical end. The graded potential across the hair cells receptor membrane is transformed to stochastic spike trains of the auditory nerve (AN) (Neubauer et al., 2009). A hair cell is connected to an AN fiber with the first synapse of the auditory system, specialized in releasing tonic neurotransmitter at high rates, locked to a specific phase of the stimulus frequency (Carr, 1986; Fuchs, 2005; Khimich et al., 2005; a.o.).

Generally in vertebrates, the length of the basilar membrane allocated for each octave is constant or increases slightly with frequency (Köppl et al., 1993; a.o.). The owl, however, shows specializations of the membrane: The basilar membrane is much longer than that of typical birds. The low CFs show similar organization to that of a typical bird's basilar membrane, but the length devoted to each octave increases toward high frequencies (Köppl et al., 1993). The highest CFs in the owl are $\approx$ 13 kHz, about one octave higher than what is typically found in birds. The highest octave at the basal end, $\geq$ 5 kHz, occupies more than half of the papillar length (Köppl, 1997b; Köppl et al., 1993).

The *tonotopic* organization, originating from the basilar membrane, is conserved throughout the auditory brainstem, auditory thalamus (Proctor and Konishi, 1997) and possibly also in the auditory cortex (Cohen and Knudsen, 1999). Within the framework of this study, the tonotopic organization is relevant in that for a given recording location the neural representation and responses to sound stimuli always show also a preference to a small range of stimulus frequencies.

### 2.2.2. Auditory nerve and its input to Nucleus Magnocellularis

Information about both the intensity and the temporal fine structure of a sound stimulus are still present in the auditory nerve (i.e., AN, eight nerve) responses (see also Figure 2.3). The timing of the stimulus is conveyd by the phase of the neural response. Other response features, such as spike counts, spike discharge rate (i.e., firing rate, meaning the number of spikes in a given time period) and response latency, code for the stimulus intensity (Sullivan and Konishi, 1984; Köppl and Yates, 1999). I first describe the general properties of the AN and its responses, and then turn to the pathway related to the ITD detection.

[1] All natural stimuli arriving to owl's ears are modified by the HRTFs before the ITD and IID cues are extracted. Stimuli used to generate the data analyzed in this thesis were presented through head-phones and thus were unaffected by the HRTF. The transformation of the stimulus amplitude by the HRTF is strong, resulting in a non-monotonic relationship between IID and elevation for high frequencies in the periphery (Keller et al., 1998). The transformation of the phase (and ITD) is not strong, and the phase remains a monotonic, almost linear function of the azimuth (Keller et al., 1998). Thus, the use of headphones does not affect our results.

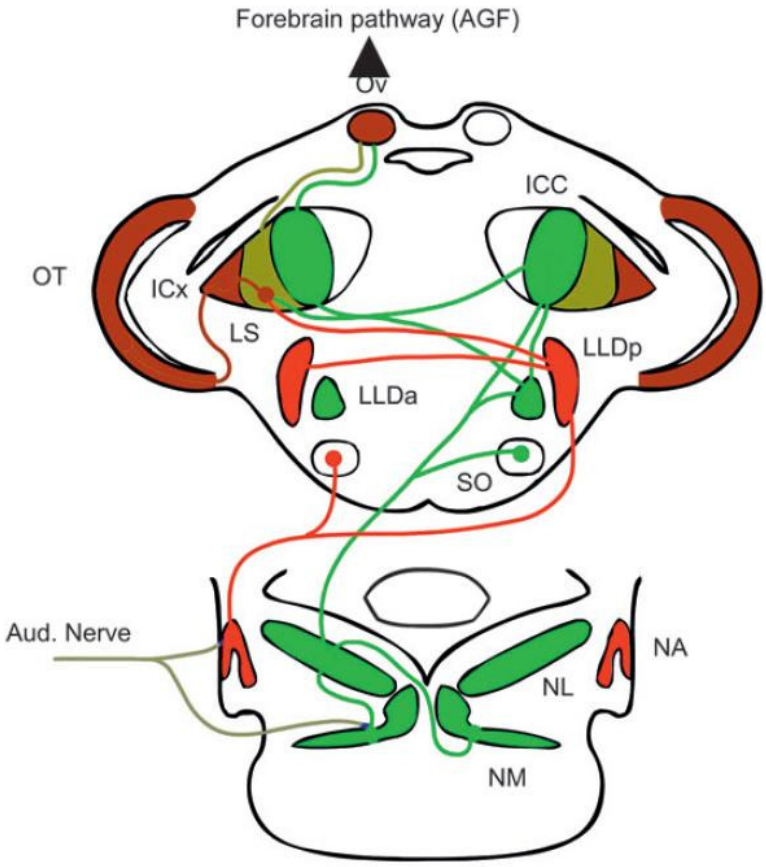


Figure 2.3.: The temporal auditory pathway of the barn owl. A schematic diagram of the pathways mediating sound localization with ITD. Auditory nerve afferents bifurcate and send collaterals ipsilaterally to both the time pathway (in green), including the nucleus magnocellularis (NM) and laminaris (NL) as well as the intensity pathways (in red), incorporating the nucleus angularis (NA). The inhibition to NA and to the NM-NL circuit is provided by ipsilateral superior olivary nuclues (SON, back-projections not shown). Interaural time and intensity difference pathways converge on subnuclei of the inferior colliculus (IC). IC projects to both the midbrain (including optic tectum, OT) and to the forebrain pathways, each of which contains space-specific neurons. LLDa, pars anterior of the dorsal nucleus of the lateral lemniscus; LLDp, pars posterior of the dorsal lateral lemniscus; LS, lateral shell of the ICC, core (i.e., central nucleus) of the inferior colliculus; ICx, external nucleus of the inferior colliculus. From Pena and DeBello (2010). Note that the SON input from NL has been hypothesized to be ipsilateral instead of contralateral as shown (Yang et al., 1999).

### Spiking properties of the auditory nerve

There is a monotonous relationship between the stimulus amplitude and the firing rate of the AN fibers, ranging from $40 - 100$ Hz for spontaneous activity (with no sound stimulus present) to $100 - 600$ Hz for saturated activity (stimulated with a loud sound but the onset response excluded) (Köppl and Yates, 1999; Neubauer et al., 2009). The highest firing rates in each range apply for lowest stimulus frequencies ($\approx 2$ kHz), and the lowest firing rates for the highest frequencies ($\approx 8$ kHz). There are different spontaneous rates among similar frequencies (similar to mammals), originating from a local nonlinearity associated with each fiber's properties (Köppl and Yates, 1999), for there is only one ribbon per synapse (Neubauer et al., 2009). In comparison in mammals, the different spontaneous rates are due to global amplification and a varying number of ribbons per synapse (Köppl and Yates, 1999; Khimich et al., 2005).

The spikes in the AN show a tendency to phase-lock to a particular phase of the stimulus (Kiang, 1965; Köppl, 1997b). For a pure tone stimulus, this means that spikes most frequently occur at a certain phase of the tone, but not necessarily every cycle of the tone. In the barn owl, the temporal fine structure of the stimulus sound waveform is preserved up to 10 kHz (Köppl, 1997b), and the jitter (or the temporal dispersion) decreases with increasing frequency, indicating enhanced temporal synchrony (Köppl, 1997b; Carr and Köppl, 2004). However, the higher the stimulus frequency $f_{\text{stim}}$, the more difficult it is to achieve a high phase-locking (the temporal jitter with respect to the duration of one cycle $T = 1/f_{\text{stim}}$). As a result, even though the temporal jitter decreases from low to high frequencies, the phase-locking is reduced (Köppl and Carr, 1997). The phase-locking can be described for example by the *vector strength* (i.e., mean resultant length). Each spike is represented by a vector whose angle corresponds to the phase at which the spike occured. Then all these phase-vectors are summed and the sum is normalized by the number of spikes. The length of the resultant vector describes how phase-locked the responses are. For spikes that all occured in the same phase, the vector strength is one, and for spikes occuring in random phases the vector strength is zero. The vector strength for the spikes in the AN ranges from $> 0.8$ to about 0.2 for 1 kHz and 9 kHz, respectively (Köppl, 1997b).

The barn owl is specialized in stabilizing and enhancing the phase-locking needed for the sound localization, and has for example an unusually high number of afferent AN fibers, in comparison to other avians ($\approx 31000$ vs. 8000 fibers in chick) (Köppl et al., 1993; Fischer, 1994).

### Separation of the phase and level pathways

The AN fibers split into two principal collaterals terminating in the cochlear nucleus magnocellularis (NM) and in the cochlear nucleus angularis (NA) (Takahashi et al., 1984) (Fig. 2.3). This serves also as a functional split between the two pathways of ITD and IID detection, respectively (Takahashi et al., 1984; a.o.).

The AN terminal in the NM forms a specialized ending in the high frequency region (Carr and Boudreau, 1991). The synapse is very large, partially enveloping the magnocellular cell body. The synapses convey the phase-locked spiking of the AN to the NM somata with a very high precision. Each endbulb has multiple chemical synaptic contacts to the target neuron, forming a secure and efficient connection. These connections enable the phase-locking to stay similarly high from AN to the NM (Carr and Köppl, 2004; Köppl, 1997b). Each branch of the AN fiber forms $3 - 6$ endbulbs to NM neurons with similar CF, and each NM neuron receives $1 - 4$ endbuld synapses (Carr and Boudreau, 1991). The AN input is received directly by the somatic spines and even by the initial segment of the single axon (Carr and Boudreau, 1993a). Such endbulb synapses have also been observed in higher order auditory neurons of mammalian time coding pathways (Brew and Forsythe, 1995; Wu, 1999), and are called the endbulb of Held or the calyx of Held (Brawer and Morest, 1975).

In the low CFs (about $< 700$ Hz), there are bouton-like terminals (Köppl, 1994) from the AN to NM, possibly indicating a gradient of the size of the synapses (a.o. synaptic properties) along the tonotopic axis in the NM (Fukui and Ohmori, 2004). The temporal precision present in the AN is not

preserved in NM at these low frequencies (Köppl, 1997b). In the IID pathway, the AN projects to the nucleus angularis with small synapses (Carr and Boudreau, 1991) and also here the temporal precision is decreased in comparison to high CF region of NL (Sullivan and Konishi, 1984).

### 2.2.3. Auditory brainstem

Together, NM and NL form the ITD detecting and mapping circuit (Fig. 2.4). There are only three neural elements in NL: firstly the axons originating from NM, secondly the axons mediating tonic $\gamma$-aminobutyric acidergic (GABAergic) inhibition from the neurons in the superior olivary nucleus (SON, Fig. 2.3), and thirdly one type of neurons within NL. I describe first the monaural inputs from NM to NL, the function of the NM axons as delay lines within NL and the coincidence detection preformed by the NL neurons. In the end I describe the input from SON.

#### Nucleus magnocellularis

The NM neurons are specialized for the encoding and conveying temporal information. Their morphology and physiology are adapted to this task, as they have a large spherical somata, one thick axon and few dendrites (Jhaveri and Morest, 1982). At the high CFs, there are further adaptations such as the low-voltage threshold $K^+$ currents, and thus high CF neurons have a smaller time constant, a more negative resting potential, and a higher threshold current and threshold in comparison to low CFs (Carr, 1993; Fukui and Ohmori, 2004). The small time constant is likely to enable the neurons to respond accurately to high-frequency stimuli Reyes et al. (1994); Zhang and Trussell (1994). Adaptations related to the synaptic input were mentioned earlier.

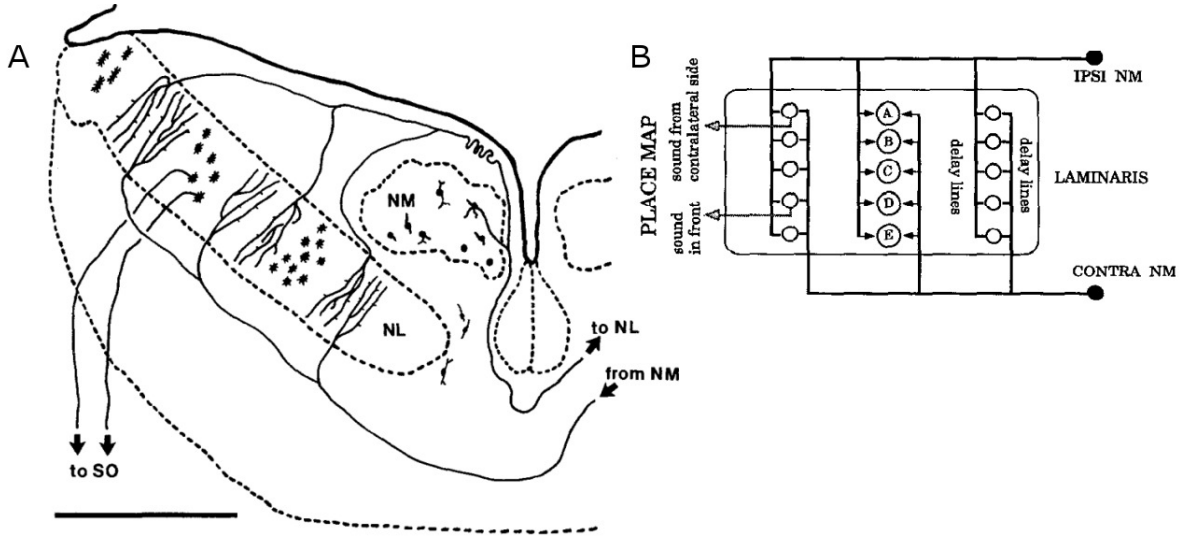


Figure 2.4.: Circuitry of NL. *A:* Magnocellular projections to nucleus laminaris. Both ipsi- and contralateral NM neurons project to NL, and NL neurons project to ipsilateral SON and to contralateral inferior colliculus (not shown). Scale bar = 1 mm. From Carr and Boudreau (1993a). *B:* A schematic of the Jeffress model realized in the owl brainstem. Axons from NM enter NL at several locations along the NL surface. The axons act as delay lines subsequently forming several ITD-based topographical maps. NM, nucleus magnocellularis; NL, nucleus laminaris; SO, superior olivary nucleus. From Carr (1993).

Apart from the phase-locked excitation, there are also few perisomatic GABAergic terminals conveying inhibitory input from local interneurons and from tonicly firing SON neurons (Carr et al., 1989) both at high and low frequencies. The inhibition might serve as a gain control adapting the response of the neurons to different stimulus levels.

The firing rate of NM neurons is relatively high for both spontaneous and sustained activity ($\approx$ 200 Hz and $\approx$ 400 Hz, respectively) (Köppl, 1997a; Peña et al., 1996), and temporal jitter of the spikes is low, $< 50$ $\mu$s (Takahashi et al., 1984; Köppl, 1997b), corresponding to a vector strength of about 0.4 for CF = 5 kHz. Similar precision is found in responses up to 9 kHz stimulus frequencies (Takahashi et al., 1984; Köppl, 1997b). The peak firing rate of a neuron at stimulus onset can be as high as 1500 Hz (Carr and Boudreau, 1993a). These high firing rates probably serve to produce sufficient input to NL in each cycle of a tone even for very high frequencies.

## Magnocellular input to nucleus laminaris: delay lines

Each NM neuron projects bilaterally to NLs (Sullivan and Konishi, 1984) (Fig. 2.4). Each neuron has one axon dividing into two main branches, one projecting to the ipsilateral and the other to the contralateral NL. A bundle of axons from the ipsilateral NM travels along the dorsal border of NL, whereas the bundle from the contralateral side travels along its ventral border (Takahashi and Konishi, 1988a). Thus, the borders of NL are composed of the afferent NM fibers and glial cells (Carr and Konishi, 1990). After reaching the specific isofrequency band, each axon branches to several primary collaterals, all entering NL at different points along the (respective) border but within the same frequency band (Fig. 2.4A shows a frequency band of ca. 5 kHz). The collaterals from contra- and ipsilateral sides interdigitate in NL and function as delay lines (Fig. 2.4B) (Carr and Konishi, 1988; 1990).

For the inputs to exhibit the correct delay within NL, they have to be finely tuned. This tuning has been proposed to be performed by the late myelination of the NM axons, after the owl's head has reached its adult size (Cheng and Carr, 2007). The late myelination enables a precise tuning of the fibers and a (Hebbian) learning of the correct delays for each of the neurons (Leibold et al., 2001a;b; Kempter et al., 2001).

The axonal conduction velocity depends on the degree of myelination of the NM axons and influences the ITD maps in NL. Within NL, the velocity in the NM axons has been estimated to be very low, in the range from $3 - 5$ m/s (Carr and Konishi, 1990; Peña et al., 2001) to about 10 m/s (Sullivan and Konishi, 1986). In comparison, the conduction velocity of large and fast axons e.g. from the cat hind limb motoneurons is in the range of $60 - 120$ m/s (Hursh, 1939; Kernell and Zwaagstra, 1981). The low velocity has been hypothesized to result from the short internodal distance ($58 \pm 5.3$ $\mu$m) and small fiber diameter ($3.18 \pm 0.74$ $\mu$m) (Carr and Konishi, 1990; Carr and Boudreau, 1993a). The low conduction velocity might be tuned so that the physiologically relevant ITDs are present in NL. The higher the condunction velocity, the wider the physical space (i.e., size of NL along the NM axons) that is needed to cover the same time (ITD) range. Thus, the higher the conduction velocity, the smaller is the range of ITDs represented within NL.

The delays in NL seems to be introduced solely by the delay lines (Peña et al., 2001; Lautemann et al., 2008; Fischer and Peña, 2009; Singheiser et al., 2010). Other possible sources of the delays have been proposed in other animals, such as the cochlear delay or the frequency mismatch of the inputs (Joris et al., 2006; a.o.). However, the frequency match of the CFs of the inputs from ipsi and contralateral sides converging to a NL neuron is $\leq$ 200 Hz even at high CFs. (Peña et al., 2001). Moreover, there is no systematic delay correlated with the frequency mismatch of the inputs (Fischer and Peña, 2009). Thus, with the highly tuned input to NL neurons and the slow conduction velocities within NL, tonotopic and topographic ITD mapping is formed.

### Convergence of the input axons to the neurons in the nucleus laminaris

NL is an ellipsoidal nucleus, except in its caudal, low frequency region, where it gets thinner and forms a fold at its lateral edge (Carr and Konishi, 1990). Its main (high frequency) part has been estimated to have a dorso-ventral depth of 700 $\mu$m, a mediolateral width of $\approx 3$ mm, and an antero-posterior length of 3.5 mm (Takahashi and Konishi, 1988a; Carr and Konishi, 1990). NL neurons are sparsely distributed, the mean distance between neighboring NL cells is about $75 \pm 8\mu$m (Carr and Boudreau, 1993a). However, aforementioned estimates do not account for example for the shrinkage in prepared tissue, and might need to be re-evaluated. In total, there are about 13,000 neurons in NL (Winter and Schwartzkopff, 1961; Kubke et al., 2004). If the volume of NL is divided by the total number of neurons, the density of the neurons in the 5 kHz region is about $2,000$ mm$^{-3}$.

The density of the NM axons is high within NL (Carr and Konishi, 1990). Each NM axon makes connections with ca. 100 NL neurons, whereas each NL neuron is connected by 45-150 axons (Takahashi and Konishi, 1988a; Carr and Boudreau, 1993a). This convergence of the inputs enables a further improvement in the phase-locking between NM to NL neurons (Carr and Konishi, 1990; Köppl, 1997b). Furthermore, it may enable a cycle-by-cycle representation of the sound in the input to NL neurons even at very high frequencies.

### Coincidence detection: properties of the neurons in nucleus laminaris and their output

NL neurons code for the ITD with their firing rate (Sullivan and Konishi, 1986) (Fig. 2.5). For coincident input to all synapses (at the favourable ITD) the firing rate rises up to $300 - 500$ Hz, wherease the input at the unfavourable ITD only elicits firing rates of 180 Hz (Peña et al., 1996). For a monaural stimulation, the firing rates are typically in the range of $210 - 240$ Hz (Carr and Konishi, 1990; Peña et al., 1996). The NL neurons get high synaptic input even if no stimulus is present because of the relatively high spontaneous firing rate of the NM neurons. However, the spontaneous rate of the NL neurons is relatively low, 50 Hz (Carr and Konishi, 1990).

The NL neurons do not respond to synaptic inputs that are not coincident because of the outward rectifying current – the DC component of any input current is nullified and only the amplitude of the frequency modulated AC component modifies the firing rate (Reyes et al., 1994). An outward rectifying current is activated when the voltage increases above the resting potential, reducing the effective membrane resistance and shortening the duration of EPSPs of the NM and NL neurons (Oertel, 1983; Manis and Marx, 1991; Reyes et al., 1994; 1996; Trussell, 1999).

The responses of the NL neurons are modulated with the interaural phase difference (IPD) rather than with the absolute interaural time difference (Moiseff and Konishi, 1981). This results in an ambiguity in ITDs, since the IPD can be more than one cycle. However, the output of the NL neurons converges higher in the auditory brainstem which solves the ambiguity, as explained on the page 13 more detailed: for stimuli including several frequencies only one absolute delay matches the phase delays of all frequencies (Peña and Konishi, 2000). Furthermore, there is a *physiological* range of ITDs that can occur for a given species, defined by the size of the head and the subsequent maximum ITD.

The NL neurons have an oval/ellipsoid soma, a thick axon and a small, compact dendritic tree (in the high CF region $> 3$ kHz) (Carr et al., 1989). The first node of Ranvier is located $\approx 60$ $\mu$m from the soma and the initial segment of the axon is myelinated (Carr and Boudreau, 1993b). Thus, the soma of the NL neuron is hypothesized to be passive, and spikes to be initiated in the first node of Ranvier (Kuba et al., 2005; Ashida et al., 2007; Funabiki et al., 2011). The spike initiation in the first node has been shown to decrease the time constant of the spike initiation in chick NL (Kuba et al., 2006). This short time constant ($\approx 10$ $\mu$s) can enable coincidence detection of inputs with a precision of $\approx 25$ $\mu$s even if arriving EPSPs were ten times broader (Gerstner et al., 1996). As a result of the short time constant, the NL neurons are well phase-locked to the stimulus. The vector strength of the output is high, e.g. $\leq 0.5$ for frequencies of 5 kHz (Peña et al., 1996).

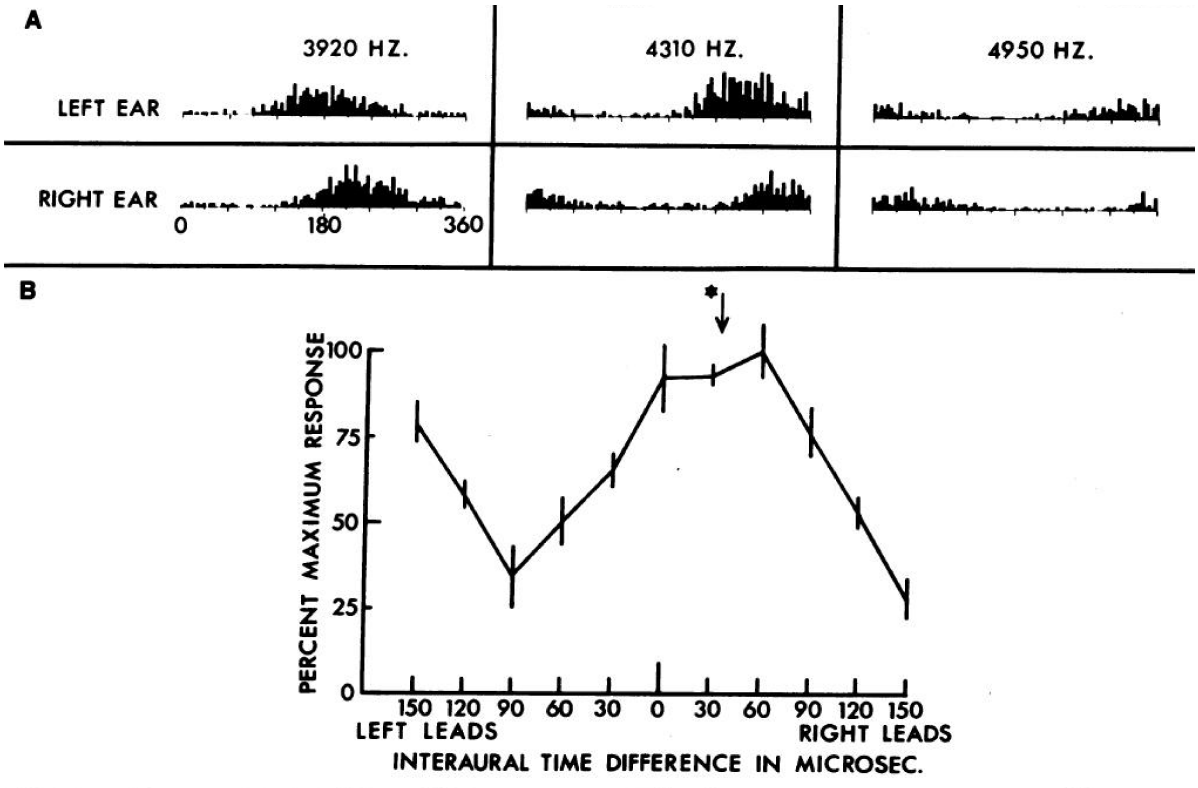


Figure 2.5.: Response in the axon of one laminaris neuron to monaural and binaural tonal stimuli recorded extracellularly. *A:* Monaural stimulation elicits phase-locked responses in the laminaris neurons. Histograms for the responses to monaural stimulation at three different stimulus frequencies are calculated over one period of the sound stimulus. They show that the response to left ear stimulation always lead the response to right ear stimulation by about 40 $\mu$s. *B:* The normalized response to binaural stimulation as a function of the interaural time difference shows a maximum when the delays in A are equalized, i.e. when the rigth ear stimulation leads the left one by 40 $\mu$s. From Sullivan and Konishi (1986).

### Inhibitory input to the nucleus laminaris

The firing rate of NL neurons depends on the sound intensity of the stimulus in a sigmoidal manner. At intensities above the saturation of the firing rate with intensity, neither the ratio of monaural firing rate to binaural, nor the ITD-rate tuning are affected by the intensity (Peña et al., 1996). There are GABAergic projections from SON to NL that have been hypothesized to protect NL neurons from losing their sensitivity even if the stimulus has a varying input intensity (Peña et al., 1996; Viete et al., 1997; Burger et al., 2005).

SON receives excitatory inputs ipsilaterally from NL and NA (Conlee and Parks, 1986; Takahashi and Konishi, 1988a; Lachica et al., 1994; Yang et al., 1999), and putatively inhibitory input from contralateral SON (Monsivais et al., 2000; Burger et al., 2005). It projects ipsilaterally back to both NL and NA, as well as to the ipsilateral NM, using GABA (Takahashi and Konishi, 1988b; Carr et al., 1989; Carr and Boudreau, 1993a; Lachica et al., 1994; Yang et al., 1999; Monsivais et al., 2000; Coleman et al., 2011). Thus, SON modulates the activity of NL and NM bilaterally (Nishino et al., 2008; Fukui et al., 2010) firstly via the direct ipsilateral projections and secondly via the bilateral connection between SONs or

via the projections to ipsilateral NM which in turn projects to contralateral NL (Burger et al., 2005; Dasika et al., 2005; Coleman et al., 2011). Each NL cell receives 30-50 perisomatic GABAergic terminals from SON neurons either to the dendrites or to the soma (Carr et al., 1989). There is no tonotopical variation in the density of the terminals in the main body of NL, but the low frequency region has, similarly to NM, a much higher density of the terminals than the main body (Takahashi and Konishi, 1988b; Carr et al., 1989).

The neurons in SON integrate excitatory inputs over a long time window and provide NL neurons with depolarizing GABAergic input. The effects of GABA to the excitability of the NL neurons can be either excitatory (small GABA concentration) or inhibitory (high concentration) (Brückner and Hyson, 1998). The mechanism of the inhibition is not clear but has been proposed to be related to the activation of the outward rectifying current (Reyes et al., 1994; 1996). The temporal averaging of SON neurons due to long integration time results in firstly a decorrelation of the temporal information in the signal and secondly a tonic inhibitory effect related to the sound intensity at the ipsilateral ear (Yang et al., 1999).

### Read-out of the space map: inferior colliculus

The main output of NL goes to the inferior colliculus (IC, earlier also called nucleus mesencephalicus lateralis pars dorsalis, MLD), where both intensity and time-pathways converge (Knudsen and Konishi, 1978a;b; Takahashi and Konishi, 1988a;b) (see Fig. 2.3). There are to two main areas in IC: central and external inferior colliculus (ICc and ICx, respectively). The ICc can be further subdivided to core (ICcc) and its medial and lateral shells.

The main projections from NL are to the contralateral core (ICcc) (Takahashi and Konishi, 1988a) and ITD is the main determinant of the activity in ICcc neurons (Bremen et al., 2007). Each ICcc neuron receives input from several NL neurons and thus averages over the inputs to acquire smooth ITD-rate functions with a large dynamic range on the first presentation (Christianson and Peña, 2006). The smoothing also serves for further noise reduction. Even though the phase information of the spike times is lost in this process, the spectro-temporal information about the stimulus is preserved throughout the ITD pathway (Christianson and Peña, 2007). The ICcc also receives input from the ipsi- and contralateral NLs (Takahashi and Konishi, 1988b) via the anterior part of the dorsolateral lemniscal nucleus (LLDa, see Fig. 2.3) (Adolphs, 1993). In the core, there is a topographical mapping of the ITD and the stimulus frequency (Wagner et al., 1987; Christianson and Peña, 2007). Mapping in the 3rd dimension is not known as of now. Most of the ICcc neurons seem to represent the central positions $\leq 50°$ in front of the owl (Wagner et al., 1987).

The medial shell of the core processes information from the contralateral intensity pathway (Takahashi and Konishi, 1988a). The lateral shell of the core gets excitatory input both from the contralateral intensity pathway and from the contralateral ICcc mediating averaged information from the ITD pathway (Takahashi and Konishi, 1988a). In the lateral shell the frequency tuning is broader than in NL, indicating that the phase ambiguity can partially be solved here (Wagner et al., 1987; Mazer, 1998).

The ICx gets its main input from the IC lateral shell neurons representing both intensity and time-information. Also tonotopically organized inputs from the ICcc (the ITD pathway) project to ICx. The frequency tuning of the neurons in ICx is very broad and the tonotopic mapping is no more present, which enables solving the phase ambiguity with means of side peak suppression (Knudsen and Konishi, 1978b; Takahashi and Konishi, 1986; Mazer, 1998). The location of a stimulus is mapped topographically (Knudsen and Konishi, 1978a;b), representing in two dimensions the elevation (IID) and the azimuth (ITD) of the stimulus (Moiseff and Konishi, 1981). The function of the third dimension is not known (Wagner et al., 1987).

### 2.2.4. Conclusions about the high frequency ITD detection

In the high frequency region of the auditory brain stem of the barn owl, the prerequisites of the Jeffress model have been found. The NM axons deliver monaural, phase-locked input to NL and work as delay lines. The neurons in NL act as coincidence detectors and map the ITDs topograhically. Altogether, the highly preserved phase-locking of the input to NL up to high stimulus frequencies and the extremely fast spike initiation with small time constant make NL neurons very good coincidence detector neurons.

In this chapter I summarized the known response properties of the neurons in NM and NL. However, NL neurons in barn owl are very difficult to record intracellularly (Sullivan and Konishi, 1986). Thus, either the bundle of NL output axons (Moiseff and Konishi, 1983; Sullivan and Konishi, 1986) or the extracellular field potential in NL has been used to characterize the response properties of NL (Sullivan and Konishi, 1986; Wagner et al., 1987; 2005; 2009). The extracellular frequency-following potential in NL (and many other areas in the auditory brainstem of mammals and avians) hase been named *neurophonic*. The most characteristic feature of the neurophonic in NL is that it also exhibits ITD tuning (Sullivan and Konishi, 1986).

The source of the neurophonic in NL of the owl is not clear, even though it has been though the reflect the computations performed by NL, similarly to cats and chicks. However, there are considerable differences between NL of the owl and NL of other avians as well as the mammalian medial superior olivary nucleus (MSO) dedicated to the same task in the larger mammals. Such differencies are for example the organization and the morphology of the coincidence detection neurons, as well as the inhibition needed in mammals for the coincidence detection per se (as opposed to the intensity invariance in the owl) (Grothe, 2003; a.o.). The specialized anatomy of the NL in the barn owl might also be reflected in the extracellular field potential.

Extracellular potentials and specifically the neurophonic potential, as well as their possible sources will be introduced in the next chapter.

# 3. Extracellular Field Potential

In this chapter I concentrate on the extracellular field potential (EFP), its ingredients and open questions about its generative mechanism. Although the origin of the intracellular potentials is relatively well understood, the way in which the membrane currents contribute to the extracellular potential is less clear and still much under discussion. The geometry, the morphology and the possible symmetry of neurons and neural networks largely define which neuronal signals contribute the most to an EFP. The properties of the extracellular medium also affect the EFP. In addition, understanding other population measures of neural activity such as electroencephalogram (EEG), BOLD-signal recorded in a functional magnetic resonance imaging (fMRI) and magnetoencephalogram (MEG) signals is closely related to the analysis of EFP and its sources, as reviewed by (Logothetis et al., 2001; Buzsáki, 2002; Buzsáki and Draguhn, 2004; Logothetis and Wandell, 2004).

I also describe the neurophonic potential, which is an extracellular potential that can be recorded in the auditory brainstem of many animals. The neurophonic closely resembles the auditory input, a property for which the potential got its name. In the nucleus laminaris (NL) of the barn owl, the neurophonic shows an extraordinary phase-locking to sound stimulus frequencies of up to 9 kHz. Owls present an excellent model system for studying the EFP because NL is large, homogeneous, and well organized. At the end of the chapter I introduce some of the methods with which extracellular potentials can be modeled.

## 3.1. General Properties of the Extracellular Field Potential

The extracellular field potential (EFP) is the net potential due to all the (electrical) transmembrane currents from different neural sources flowing from and into the extracellular space. The current sources include axonal nodes of Ranvier, synapses and the soma of the neurons, among others. The voltage of a recording electrode always needs to be compared to a reference voltage, and the position of both electrodes can be crucial for their difference, which is the recorded EFP. The EFP can be divided into different frequency components, that reflect different types of activity (Fig. 3.1). Usually, the high frequencies ($> 500$ Hz) are thought to reflect the single- or multi-unit activity (SUA and MUA, respectively), i.e., the spiking activity of near-by somata (Logothetis et al., 2001; Galindo-Leon and Liu, 2010; Pettersen et al., 2008). The lower frequencies ($< 300$ Hz) are thought to reflect the synaptic currents, their return currents and population spikes (Mitzdorf, 1985; Nunez and Srinivasan, 2006), but individual spikes or spike times can not be identified. However this does not mean that the spikes do not contribute power to the low frequencies. Thus, once the spike times have been identified from the high-pass filtered MUA recording, the reconstruction of the spike wave form should be done with very wide filtering (e.g. $1 - 5000$ Hz) (Gold et al., 2007) to avoid distortion of the extracellular spike shape. The extracellular spike wave form is important e.g. when reconstructing a MUA recording from spike times, or when identifying spikes in an extracellular recording by spike waveform templates.

I describe first the idealized summation of the transmembrane currents in the extracellular medium and then the contribution of dipole- and line current sources to the EFP. In order to provide a more realistic description of the EFP, I also discuss some properties of a more realistic, non-idealized, extracellular medium.

### 3.1.1. Summation of currents in the extracellular space

Identifying the origin of an EFP can be difficult. Macroscopic potentials and currents measured in the extracellular space cannot always be mapped in a one-to-one manner back to their neural origin. In contrast, the linear summation of the microscopic *current source densities* (CSDs, $I_m$ in units of [A/m$^3$]) provides a direct link to the macroscopic potential in a given location (Mitzdorf, 1985; Pettersen et al., 2010), as follows.

The membrane current source density is equivalent to the divergence of the extracellular current density $\vec{J}$ [A/m$^2$] (Nicholson and Freeman, 1975; a.o.):

$$\vec{\nabla} \cdot \vec{J} = I_m \quad . \tag{3.1}$$

The extracellular current density also can be related to the electric field $\vec{E}$ [V/m] and to the (induced) potential $\Phi$ [V]. Firstly, for a linear extracellular medium, Ohm's law holds:

$$\vec{J} = \sigma \cdot \vec{E} \quad , \tag{3.2}$$

where $\sigma$ is the conductivity [S/m] of the extracellular medium. It should be noted that if capacitive effects of the medium on the currents are included, the conductivity becomes a comlex, frequency-dependent quantity (Nunez and Srinivasan, 2006). For the frequency-dependent conductivity, the equation above applies only in frequency space (Bédard and Destexhe, 2009; Pettersen et al., 2010).

Secondly, the quasi-static approximation of Maxwell's equations gives the connection to the potential $\Phi$:

$$\vec{E} = -\vec{\nabla}\Phi \quad . \tag{3.3}$$

This *quasi-static approximation* neglects the time derivatives of the electric and magnetic fields. From the Eqs. (3.1), (3.2) and (3.3) we get the contribution of a transmembrane current $I_0$ located at distance $r_0$ from the location of the electrode $\vec{r}$ to the extracellular potential $\Phi$ (Nunez and Srinivasan, 2006;

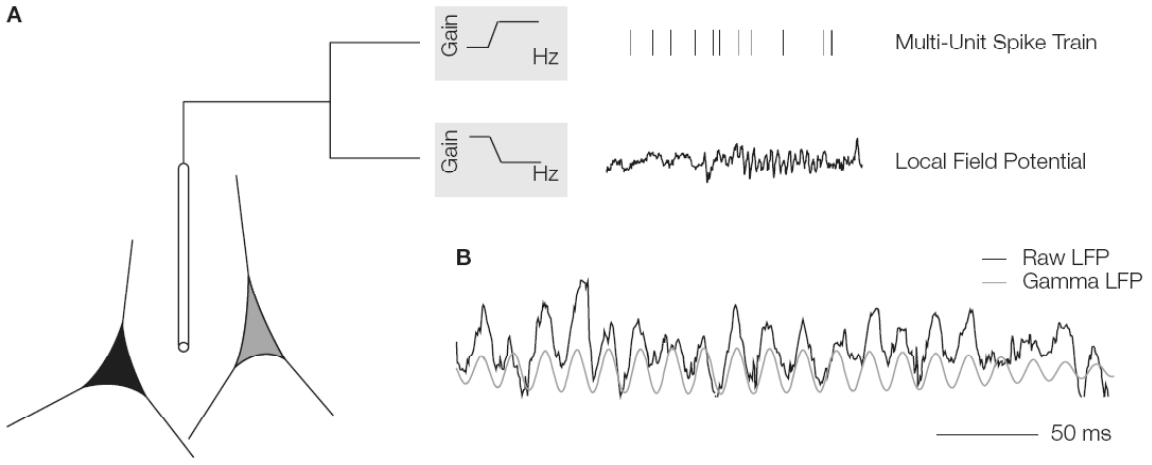


Figure 3.1.: Extracellular field potential. *A:* An extracellular electrode records the potential originating from near-by neural current soures. By low- or high-pass filtering, multi-unit activity or the local field potential can be detected in the potential. *B:* By band-pass filtering, also oscillatory activity e.g. in the gamma-band (here in the visual cortex of an awake primate) can be extracted from the original potential. From Berens et al. (2008).

Pettersen et al., 2010; a.o.):

$$\Phi_0(\vec{r},t) = \frac{1}{4\ \pi\ \sigma}\frac{I_0(t)}{r_0} \quad . \tag{3.4}$$

Furthermore, we can linearly add up the current sources $I_n$ located in $r_n$

$$\Phi(\vec{r},t) = \frac{1}{4\ \pi\ \sigma}\sum_{n=1}^{N}\frac{I_n(t)}{r_n} \quad . \tag{3.5}$$

Due to distance-weighted averaging of the currents in Eq. (3.5), the individual currents can be considerably larger than the resulting current density and the extracellular potential.

The previous equations rely on several assumptions. The extracellular medium is assumed to be linear, its conductivity is assumed to be frequency independent and its capacitive, inductive, magnetic and propagative effects are assumed to be negligible. The validity of these assumptions is discussed later in this chapter.

The main sources for the extracellular currents are synaptic, somatic and axonal currents of the neurons, as discussed next. Other possible current sources, such as glial cells, generate very slow currents in comparison, and their contribution is negligible (Mitzdorf, 1985).

### 3.1.2. Dipole sources

Dipole currents are one of the most typical current structures in the extracellular medium. A dipole appears in the extracellular field whenever a current sink (positive current to the extracellular medium) and source (negative current) co-occur by means of a common transmembrane current. In the dipole, the same current flows into one of the poles and out from the other. The electric field that a dipole current source creates, depends apart from the currents, on the distance between the poles. There are several kinds of dipole sources in the neuronal tissue. On one hand, axon terminals and synapses can induce dipoles of a very small spatial extent. On the other hand, a pyramidal neuron with the spike initiated in the soma and most of the passive (capacitive and ohmic) *return currents* entering the apical dendrites can create a dipole with its poles separated by hundreds of micrometers (Lindén et al., 2010; a.o.).

In the far-field approximation (Fig. 3.2 A), the potential measured at distances $r_1$ and $r_2$ from a sink-source pair, respectively, induced by a current $I_d$ flowing into the sink and out of the source is (Nunez and Srinivasan, 2006):

$$\Phi(\vec{r}) = \frac{I_d}{4\ \pi\ \sigma}\left(\frac{1}{r_1} - \frac{1}{r_2}\right) \quad , \tag{3.6}$$

or this geometry can be approximated by

$$\Phi(\vec{r},\theta) \approx \frac{I_d}{4\ \pi\ \sigma}\ \frac{d}{r^2}\cos(\theta) \quad , \tag{3.7}$$

where $\theta$ is the angle between the axis of the dipole and the line from the electrode at $\vec{r}$ to the middle of the dipole, $r$ is the distance from the middle of the dipole to the electrode and $d$ is the separation of the poles. From the latter approximation it is clear that the amplitude of the potential from a dipole source decays proportionally to $1/r^2$.

The morphology of the dendritic tree affects the electrical properties of neurons, particularly with respect to the amplitude decay of the potential of the induced dipole (Pettersen and Einevoll, 2008). Despite a neuron having a simple geometric shape, the amplitude decay of the potential may deviate from quadratic. The dendritic tree may also impose a low-pass filtering to the currents and extracellular potential (Lindén et al., 2010). Because of these filtering properties and of the frequency dependent conductivity, the size of the dipole induced by a sink-source pair depends on the frequency of the currents

involved. Firstly, e.g. in a pyramidal cell, the fraction of apical input current that propagates to soma depends on its frequency: for low frequencies a larger fraction will propagate further than for high frequencies. Secondly, the (passive) return currents are low-pass filtered by the dendritic tree so that far away from the synaptic input current the EFP includes more low frequencies than EFP recorded close to the input current (Pettersen and Einevoll, 2008; Lindén et al., 2010).

Now I will discuss the different dipole sources of the neural tissue, as well as the specific situation in the NL neurons (for more details of the physiology, see also section 2.2.3). During spike initiation, there are two kinds of dipoles mainly effecting the EFP. Firstly, the dipoles created by the synaptic currents and their return currents mainly to other dendrites but possibly also to the soma and, secondly, those created by the spike and the corresponding return currents to the dendrites. Note that in this chapter NM and NL refer to the those of the owl, unless stated otherwise.

### Synaptic activation

The effect of the synaptic activation on the membrane currents and the induced EFP much depends on the geometry of a neuron.

Active ionic currents enter the cell at synapses with an excitatory synaptic activation, whereas return currents equal in amplitude leave the cell at proximal and more distant sites (Mitzdorf, 1985). For a pyramidal neuron (Fig. 3.2 B) this creates a large dipole, whereas for a neuron that is geometrically more dense, the dipole can be much smaller both in its spatial extent and in the amplitude of the potential (Fig. 3.3 A). The same holds for the inhibitory post-synaptic potentials, except that the polarity of the dipole is reversed. However, the sites at which excitation and inhibition enter the cell can differ spatially and temporally (Wirth and Lüscher, 2004; a.o.) and thus the dipoles induced by excitation or inhibition differ futher. Because of the linear summation of the currents, a layer of similarly oriented neurons with similar input pattern produce much larger EFPs than neurons having either a variable spatial orientation or temporal input pattern (Fig. 3.2 C). Also capacitive currents can be created, being proportional to the membrane capacitance and the temporal change in the membrane voltage (Malmivuo and Plonsey, 1995; a.o.).

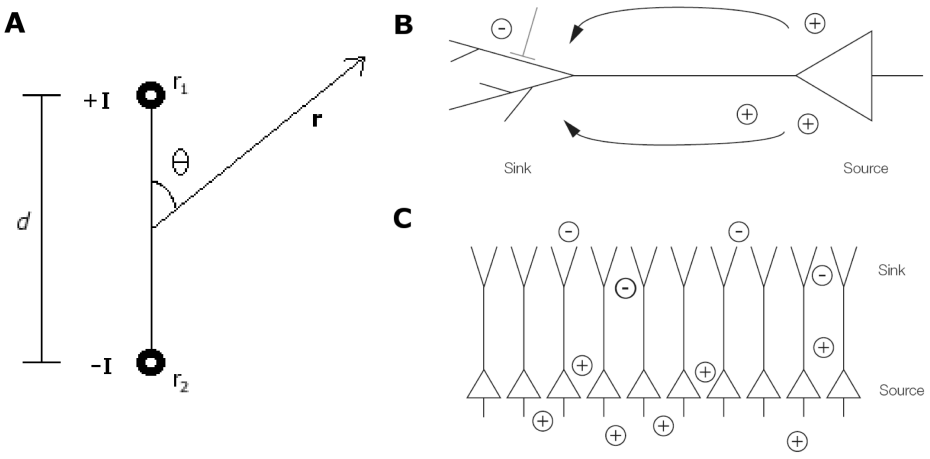


Figure 3.2.: Dipole. *A:* Current is flowing from $\vec{r}_1$ $(+I)$ to $\vec{r}_2$ $(-I)$. The distance between the sink and the source is $d = |\vec{r}_1 - \vec{r}_2|$ and the electrode is located at $\vec{r}$. The angle between axis of the dipole and the location electrode is $\theta$. *B:* In a pyramidal cell, the a synaptic potential creates a sink at the dendrites and a source at the soma. *C:* In a layer of pyramidal cells, synchronous synaptic currents can create strong dipoles. *B–C* from Berens et al. (2008).

In the NL neurons, the dendrites do not have a tree-like structure but are stubby ($5 \pm 1.9$ $\mu$m long and $2 - 3$ $\mu$m wide), and most synapses from NM axons project to them. Furthermore, the dendrites are not polarized to any direction with respect to the cell body (Carr and Boudreau, 1993a). Thus the spatial input pattern is not polarized but rather uniform. Each neuron receives excitatory input from about 100 NM neurons that all fire in a phase-locked manner with a high firing rate. Thus, there are simultaneous inputs through many synapses in each cycle of a sound stimulus. Furthermore, the return currents probably exit the neuron in the soma in a rather homogeneous manner, and these multiple simultaneous dipoles might cancel out each other.

Each NL neuron also receives about 120 GABAergic synapses (Carr and Boudreau, 1993a), delivering tonic, not phase-locked inhibition. Similarly to the excitatory inputs, the EFP due to the inhibition is likely to cancel out because the inhibitory synapses in the small dendritic tree do not exhibit systematic arrangement but are distributed nearly homogeneously. In NL neurons, the sites of inhibition and excitation are similar, possibly further reducing the magnitude of the EFP. However, an EFP created by the inputs to one NL neuron has not been modeled or measured so far.

#### Action potentials

The firing of an action potential (AP) releases extracellular currents at the site of AP initiation in three temporal phases. The first phase is a small passive depolarizing current, followed by the hyperpolarizing net effect of the active sodium and potassium currents and the local depolarizing capacitive current (Mitzdorf, 1985; Gold et al., 2006; 2007; Lindén et al., 2010). The return currents enter the cell in the dendritic tree and the magnitude of all passive return currents is in total equal to the currents of the AP. However, the spatial distribution of the current density is unlikely to be homogeneous in the whole dendritic tree, and thus, locally the magnitude of the EFP due to (local) return currents can exceed the magnitude of the EFP due to the (local) active currents of the AP. The morphology of the dendrites defines the spatial extent and magnitude of the electric field, which might deviate from a dipole, being e.g. quadrupolic (Lindén et al., 2010).

In the NL neurons, the spike is not initiated in the soma or the axon initial segment, but in the first node of Ranvier, located about 60 $\mu$m apart from the soma. Because of the small dendritic tree, the return currents of a spike can be approzimated to enter the oval soma. Thus, a spike in an NL neuron initiates a dipole field with its poles about 60 $\mu$m apart. Because the intracellular amplitude of the spike is small (about 15 mV), also the extracellular field probably stays small. The axons of the NL neurons are oriented all to the same direction with respect to the soma, approximately orthogonal to the frequency layer. The NL neurons are sparsely located in the NL, and because the spatial fall-off of a dipole is fast, the dipoles' fields (perpendicular to the axis of the dipole) do not overlap with large amplitude. The NL neurons are not organized as a monolayer. The summation of the fields parallel to the axis of the dipole only has an effect on the 'borders' of the frequency layer. Perpendicular to the axis of the dipole, the summation of the fields might have an effect on the borders of laminaris.

Unfortunately the extracellular spike waveform of NL neurons are difficult to record because of the large amplitude of neurophonic (see also section 3.2). There are few intracellular recordings of the spike waveform published so far (Carr and Konishi, 1990) and thus its spectrum is not available. The duration of the spike has been estimated to be short, about 200 $\mu$s (Carr and Konishi, 1990; Ashida et al., 2007).

### 3.1.3. Active nerve conductor sources — line sources

A spike waveform has a triphasic extracellular spatial profile, as discussed before. This applies also to spikes travelling along an axon, resulting in a source-sink-source distribution. At a given time point, the spike advancing in an axon has reached some node of Ranvier. The currents in a given node of Ranvier are first positive, then negative and then again positive, but smaller (Fig. 3.3 B, top).

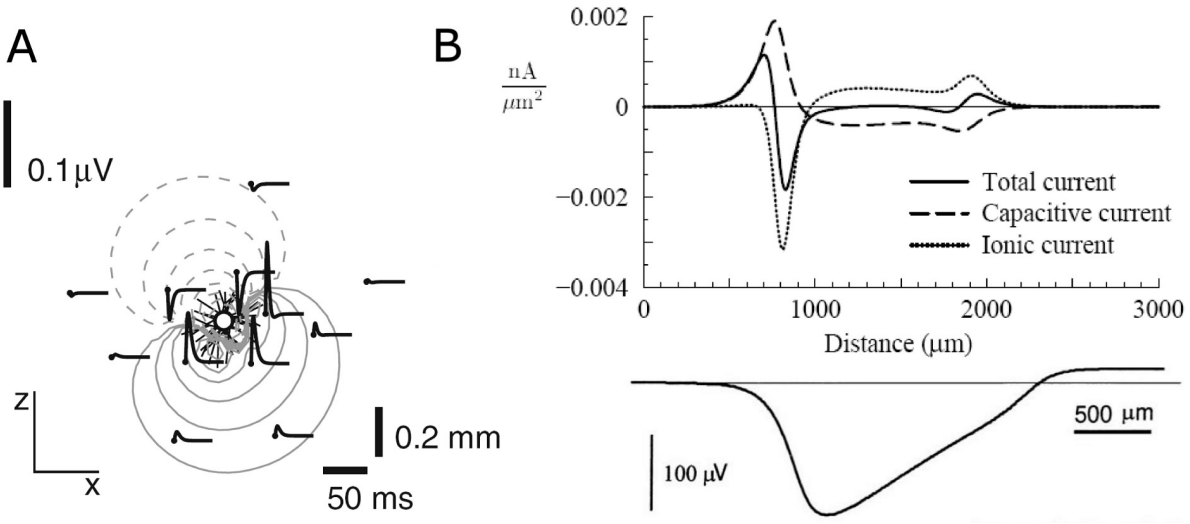


Figure 3.3.: Extracellular potentials induced by a spike. *A:* An EFP resulting from a single excitatory synaptic input to a stellate cell body with purely passive soma and passive, slightly asymmetric dendritic tree. The EFP amplitude decays by a factor 2 between each contour line. From (Lindén et al., 2010). *B:* An axonal spike. Top: A schematic picture of the currents flowing at one instant of time, the spike is advancing to the left. Current density as a function of position along an unmyelinated axon (diameter: 1 $\mu$m, conduction velocity: 0.44 m/s, the spike has been generated using a Hodgkin-Huxley model). From (Holt, 1998). Bottom: Potential from an axon in shealt, i.e., myelinated axon. Otherwise the parameters of the axons are the same. The EFP is proportional to the membrane potential and inversely proportional to the square of the sheath diameter. From (Holt and Koch, 1999). The proportion of top and bottom figures showing the currents and the EFP is not exactly 1 : 1, nor is their allignment exact.

Again, we can sum up all the currents at one location linearly (Eq. 3.5). As the spike advances in the axon, the 'valley' of the EFP also advances in space (Fig. 3.3 B). The conduction velocity with which the spike advances plays a great role in the spatial extent of this valley. Also the extracellular currents from each node of Ranvier are typically very small; for CA1 neurons they are two orders of magnitude smaller than somatic currents (Gold et al., 2006). Furthermore, usually the axons are not regularly oriented in the extracellular space nor are the spikes travelling in them temporally coherent. Thus, most of the axonal currents cancel out, and do not play a large role in the extracellular potentials. Furthermore, line current sources make only a local effect on EFP. At small distances ($\leq 100$ $\mu$m) from the line current sink, the decay of the EFP amplitude is slow, about $1/r$, but at farther away from the sink the decay can be more rapid than $1/r^3$ (Pettersen and Einevoll, 2008).

In the NL there is a high density of parallel axons conducting synchronous and temporally coherent spikes. Because of the currents' summation, this might induce a volley of input activity advancing through NL. This 'volley principle' was introduced already by Wever and Bray (1930) for the auditory nerve fibers. Such a volley might make a significant contribution to the EFP. The intracellular spike waveform in the axons of the NM neurons has been rarely published (Carr and Konishi, 1990) and the tranformation of the intracellular potential to the extracellular might be frequency-dependent and thus not be linear. Furthermore, the spectrum of the extracellular spikes from NM axons is not known.

### 3.1.4. Extracellular medium

The distance over which electrical signals in the extracellular medium give rise to the EFP depends much on the properties of the extracellular medium, on the synchrony of the neural current sources and on the morphology of these sources. The synchrony of the sources depends e.g. on the connectivity in a given nucleus, and was discussed for NL in the previous sections 3.1.2 and 3.1.3. Now I discuss the most important properties of the extracellular medium.

According to simplifying assumptions often used, extracellular space is (or can be approximated to be) homogeneous, and isotropic and its conductance properties scalar or even constant (Pettersen et al., 2010; a.o.). However, this need not be true for a all neural tissues, and the deviation from these approximations might have a significant effect on the way currents sum up to give rise to the EFP.

#### Filtering properties of the extracellular medium

There is controversy about how substantial the filtering properties of the extracellular medium on different frequencies are. Spikes are regularly only seen in the vicinity of the recording electrode, leading to a perception of fast attenuation of high frequencies in the extracellular medium. Slower events have been reported to be visible over few hundred micrometers (see below).

The attenuation in the voltage due to filtering of the extracellular matter has been measured to be flat, about $2-3$ dB for the frequency increase from 10 Hz to 5 kHz (Logothetis et al., 2007) in the monkey cortex, independently of the depth or the direction of the measurement. In the transition from the white to the gray matter the orientation of an electrode array plays a role, but the attenuation is within a similar range. Also the phase of the oscillatory voltage (e.g. spike) can change due to the filtering. A moderate phase shift of a few degrees has been measured from low to high frequencies. This shift is comparable to that in saline bath or with an ohmic resistor (Logothetis et al., 2007).

On the other hand, there are measurements of the gray matter (Gabriel et al., 1996) as well as theoretical considerations of the extracellular medium (Bédard et al., 2004) showing that a non-constant extracellular conductivity and permittivity may result in a low-pass filter. The transfer function between the intracellular membrane potential and the local field potential indicates a frequency dependent impedance (from 3 to 500 Hz) in order to match the intra- and extracellular measurements (Bédard et al., 2010). Furthermore, the morphology of the dendritic tree has been shown to influence the filtering of the trans-membrane currents, changing the size of the induced dipole in a frequency-dependent manner (Pettersen and Einevoll, 2008; Lindén et al., 2010) (see also 3.1.2).

#### Recording radius of an electrode

In the cortex, several studies have shown that more than 95% of the LFP signal originates within 250 $\mu$m of the recording electrode (Katzner et al., 2009; Xing et al., 2009). Whether this is true for all (especially higher) frequencies is unclear (Kajikawa and Schroeder, 2011) but single- or multi-unit activity (characterized by higher frequency components than LFP) can be collected only from the close vicinity of the recording electrode. For distances larger than 140 $\mu$m the spikes are indistinguishable from the background noise (Henze et al., 2000). The electrode impedance and geometry do not seem to affect LFP recordings considerably (Nelson and Pouget, 2010).

As a general rule, the amplitude of the EFP caused by a dipole source decays with $1/r^2$, and that caused by a line-source with $1/r$ in the vicinity of the conductor but with $1/r^3$ in the far field (Nunez and Srinivasan, 2006; Pettersen and Einevoll, 2008). However, the morphology of individual neurons can affect their contribution to the EFP more than the general rule. In the vicinity of a neuron the morphology of the dendritic tree influences the decay of the EFP amplitude. The amplitude decay of EFP from dipoles can be e.g. exponential (Rall, 1962) or $1/r$ (Pettersen and Einevoll, 2008). Far away from the neuron, the decay can be as steep as $1/r^5$ (Pettersen and Einevoll, 2008). Thus, each neural

structure must be studied individually, and strong generalizations about the origin of the EFP can be difficult to make.

## 3.2. Neurophonic Potential in Barn Owl Nucleus Laminaris

The neurophonic potential, which is the central phenomenon studied in this thesis, is an EFP with a broad bandwidth. The data analyzed in this thesis has been band-pass filtered at $100 - 13,000$ Hz. Such frequencies normally reveal single-unit activity. However, single-unit activity cannot be identified in the neurophonic (Sullivan and Konishi, 1986). This suggest that signals from too many sources are mixed together in the neurophonic to be detectable individually.

### Short history

In the auditory system, an EFP that is well correlated with the acoustic stimulus is termed neurophonic potential or simply 'neurophonic' (Weinberger et al., 1970). The neurophonic has been observed in the auditory nerve (Wever and Bray, 1930; Snyder and Schreiner, 1984), in the cochlear nucleus (Marsh et al., 1970; Worden and Marsh, 1968), in nucleus laminaris (NL) (Sullivan and Konishi, 1986; Schwarz, 1992a; Wagner et al., 2005; Köppl and Carr, 2008), in the lateral and medial superior olive (Boudreau, 1965; Weinberger et al., 1970; Bojanowski et al., 1989; Marsh et al., 1974), and in the inferior colliculus (Marsh et al., 1974).

The origin of neurophonic potentials in the auditory system is still a matter of debate. In chicken NL as well as cat medial superior olive, the neurophonic is highest in amplitude in the vicinity of the densely packed neuron layer, and therefore hypothesized to originate from post-synaptic activity (Guinan et al., 1972; Schwarz, 1992a; Köppl and Carr, 2008; Mc Laughlin et al., 2010a). In contrast, in NL of the barn owl, a prominent neurophonic is found throughout the tonotopically organized nucleus, where axon density is high and neuron density is low. Owls present an excellent model system for studying the EFP because NL is large, homogeneous, and well organized. This nucleus has a dorso-ventral depth of about 700 $\mu$m, a medio-lateral width of about 2 mm, and an antero-posterior length of 3.5 millimeters. Compact NL neurons are sparsely and evenly distributed with a mean distance of about 100 $\mu$m (Carr and Konishi (1990) 75 $\mu$m is not corrected for shrinkage). In the high-frequency region ($> 2.5$ kHz), NL neurons have very short stubby dendrites (Carr and Boudreau, 1993a). Functionally, NL neurons encode interaural time differences (ITD), which provides the main cue for azimuthal sound-localization (Moiseff and Konishi, 1981; Poganiatz et al., 2001). NL neurons detect the coincident arrival of phase-locked spikes from the ipsi- and contralateral nucleus magnocellularis (NM) (Carr and Konishi, 1990). Despite our detailed knowledge, and the comparatively simple nature of the circuit in NL, the origin of the neurophonic in NL of the barn owl has remained elusive.

### Characteristics of the neurophonic in NL

In the barn owl, the neurophonic potential in NL is characterized by an outstanding temporal precision; the neurophonic responses to click stimuli exhibit a standard deviation (SD) of the phase delay of about 10 $\mu$s (Wagner et al., 2005; 2009). Acoustic clicks produce robust and reliable responses: Essentially identical responses emerge over hundreds of repetitions of the same click stimulus (Wagner et al., 2005; 2009). The neurophonic potential from pure tone stimulation is smooth and oscillatory (Sullivan and Konishi, 1986) with amplitudes in the millivolt range. The implication of these properties is that a large number of spiking neuronal sources should contribute to the neurophonic. Even if each source has a firing rate in the range of hundreds of spikes per second, many sources are necessary in each stimulus cycle to generate a reliable and oscillatory time course. A more precise statement, however, requires a more quantitative approach.

## 3.3. Modeling the Extracellular Field Potential

There are several approaches in modeling extracellular potentials, from large to small scale modeling. In the large scale models there are e.g. the mean field approach and back-tracking current sources, which is often used to trace the sources of EEG (Nunez and Srinivasan, 2006; a.o.). In the small scale models the currents from individual (more or less) realistic neurons or the effects of individual channels in the membrane are considered (Gold et al., 2006; 2007; Pettersen and Einevoll, 2008; Lindén et al., 2010; a.o.). Point processes, such as the Poisson process used in this thesis, are in the midway of these approaches, allowing as well for individual sources as for statistical analysis of their mean fields and effects (Bédard et al., 2006; Rasch et al., 2009).

### 3.3.1. Point processes

A point process is defined as a mapping from probability space to a set of discrete measurements (Bartlett, 1978)[a.o.]. It is a stochastic process generating e.g. a sequence of events, such as spikes, that follow a given probability distribution. A renewal process restricts this definition so that the probability of an event only depends on the immediately preceding event, but not on the entire previous history. A Poisson process is a point process with no dependence on the preceding events, and thus all events are statistically independent (Dayan and Abbott, 2001) and the resulting spectrum is flat Lindner (2006). The Poisson process can be further categorized either as a stationary, i.e., homogeneous Poisson process in which the probability of the occurrence of a spike is constant over time, or as an inhomogeneous Poisson process with a time-dependent probability distribution.

The Poisson process is a stochastic way of spike time generation, and the same result is achieved either by generating the firing pattern of each source by a separate process or combining the generation of all the sources to a single process. This means that the probability distribution for each source is identical to the sum of the probability distributions.

Refractory periods often occur in the spiking of a neuron since the neuron cannot release action potentials with an arbitrarily high rate for biophysical reasons. The refractory period between the events can be taken into account also in the Poisson process by adding an absolute delay after each event. The refractory period affects the output spike-rate in a frequency-dependent manner, influencing for example the second and higher harmonics of the output spectrum in comparison to the poisson process with no refractoriness (Deger et al., 2010; 2011). However, the spike time probability distribution for a large number of sources with high spike rates can be approximated with a Poisson process with no refractory period.

In the modeling part of this thesis, I use the Poisson process with no refractory period to create spike times, which are then represented by a $\delta$-function. I convolve the spike times with a spike wave form to model a continuous extracellular voltage composed of the voltages of several independent sources.

#### The underlying probability distribution of a Poisson process

The Poisson process can be either homogeneous or inhomogeneous – in the latter case the firing rate is time dependent. The most efficient way to generate an inhomogeneous Poisson process is to first generate spike times (or interspike intervals) for a homogeneous Poisson process with a maximum rate that will be present in the inhomogeneous case, and then 'thin out' the homogeneous spike train (i.e. rejection sampling) so that the spike rate corresponds to the given, time-dependent (inhomogeneous) function (see, e.g. Dayan and Abbott (2001; pp. $25-31$)).

For a constant (homogeneous) firing rate, the Poisson process generates *every sequence of $n$ spikes over a fixed time interval with equal propability.* The probability that exactly $n$ spikes occur within a time interval $T$, where $r$ is the rate and $T$ is the duration of a trial, is given by the Poisson distribution

(Dayan and Abbott, 2001):

$$P_T[n] = \frac{(rT)^n}{n!} \exp(-rT) \quad , \tag{3.8}$$

making $rT$ the expected number of spikes. Now the probability of an interspike interval (ISI) falling between $\tau$ and $\tau + \Delta t$ is (Dayan and Abbott, 2001)

$$P[\tau \leq t_{i+1} - t_i < \tau + \Delta t] = r\Delta t \exp(-r\tau) \quad , \tag{3.9}$$

where $r\Delta t << 1$. The spike times can be generated either for each time point (in a spike/no spike -manner) or by drawing the ISIs from the probability distribution in Eq. (3.9), which is a more efficient computationally. The spike times are generated by an iterative rule $t_{i+1} = t_i - \ln(x_{rand})/r_{max}$, where $0 < x_{rand} < 1$ is a random number drawn from a uniform distribution, and $r_{max}$ is the maximum firing rate.

To select the spike times of the inhomogeneous process, one can first create spike times of a homogeneous Poisson process, in which $r_{max}$ is larger than the maximum of the estimated inhimogeneous firing rate $r_{est}(t)$. Then, for each spike time, the normalized estimated rate $r_{est}(t_i)/r_{max}$ is compared to another random number from the uniform distribution, and the spike is kept only if $r_{est}(t_i)/r_{max} \geq x_{rand}$; otherwise the spike is removed. The spikes created can be convolved with a spike waveform to form a continous voltage trace (for details, see subsection 4.3.3 'Computational model'.

## 3.4. Open Questions

Finding out which neural sources contribute to the neurophonic potential will be a big step towards understanding more about the relation of the activity of single neural components and the extracellular field potential. The neurophonic potential in mammals and in chicks has been observed mainly in the vicinity of the thin layer of neurons in NL/MSO (Schwarz, 1992a;b; Mc Laughlin et al., 2010a), and thus the neurophonic has been associated with the currents conveying information about the activity of these neurons, i.e., the output from the nucleus. However, this might not be the case in the owl, for the morphologies of the structures have substantial differences. For example, the NL neurons in the owl are not organized to a thin layer but are homogeneously distributed across ca. 700 $\mu$m thick nucleus. Thus, this thesis will help understand the influence of the morphology of a neural structure on the EFP.

As a first step it is important to reveal which sources are of utmost relevance for the neurophonic in the owl NL. This means making a separation between the sources that must contribute to the neurophonic to keep its characteristic signatures, and those sources that might contribute but in a smaller order of magnitude. In the next chapter, I study the neurophonic in response to monaural stimulation in order to extract the essential neural sources contributing to it.

How is it possible to assess other contributions from further neural sources to the EFP? The relationship of the neurophonics in response to monaural and to binaural stimulation is yet unclear but analyzing it allows studying the contribution from minor sources. Depending on the contributions from both the essential as well as from the minor sources to the neurophonic, the neurophonic response and its spectrum will change. In the chapter 5 I analyze this relationship in data in order to reveal the minor sources contributing to the neurophonic. I extend this analysis in the chapter 6 to the data presented in frequency-domain by its specturm, which allows for further conclusions about the contributions.

# 4. Monaural Signal-to-Noise Ratio in the *Nucleus Laminaris*

This chapter concentrates on the question of how can a neurophonic potential be formed in NL of the barn owl — what are the minimum requirements of initiating the data recorded (Kuokkanen et al., 2010)[1].

## 4.1. Summary

The neurophonic is a sound-evoked, frequency-following potential that can be recorded extracellularly in nucleus laminaris of the barn owl. The origin of the neurophonic, and thus the mechanisms that give rise to its exceptional temporal precision, has not yet been identified. Putative generators of the neurophonic are the activity of afferent axons, synaptic activation of laminaris neurons, or action potentials in laminaris neurons. To identify the generators, we analyzed the neurophonic in the high-frequency ($> 2.5$ kHz) region of nucleus laminaris in response to monaural pure-tone stimulation. The amplitude of the neurophonic is typically in the millivolt range. The signal-to-noise ratio reaches values beyond 30 dB. To assess which generators could give rise to these large, synchronous extracellular potentials, we developed a computational model. Spike trains were produced by an inhomogeneous Poisson process and convolved with a spike waveform. The model explained the dependence of the simulated neurophonic on parameters such as the mean rate, the vector strength of phase locking, the number of statistically independent sources, and why the signal-to-noise ratio is independent of the spike waveform and subsequent filtering of the signal. We found that several hundred sources are needed to reach the observed signal-to-noise ratio. The summed coherent signal from the densely packed afferent axons and activation of their synapses on laminaris neurons are alone sufficient to explain the measured properties of the neurophonic.

## 4.2. Introduction

Extracellular field potentials (EFP) are important assays of neural function. Exact connections between the EFP and its neuronal generators, however, are unclear. EFPs were thought to originate exclusively from synaptic events (Buchwald et al., 1965; Mitzdorf, 1985), until recent studies showed that they could also be composed of slow waveforms, including the after-potentials of somato-dendritic spikes and membrane-potential oscillations (for review, see Logothetis and Wandell (2004)). Unfiltered EFP from many kinds of neuronal tissue reveal individual action potentials as well as slower changes in potential (e.g. Arezzo et al. (1977)).

In the auditory system, an EFP that is well correlated with the acoustic stimulus is termed neurophonic potential or 'neurophonic' (Weinberger et al., 1970) (see also the section 3.2: 'Neurophonic Potential'). Identification of the source(s) of the neurophonic is important since they may reflect the computations

[1] Results presented in this chapter have been published in (Kuokkanen et al., 2010) and are a collaboration with several researchers. I did the data analysis, the modeling, the analytical calculations and wrote the manuscript. The experimental data was recorded by Catherine Carr and Hermann Wagner in their laboratories in University of Maryland, US and in RWTH Aachen, Germany.

performed in NL, which are essential for the localization of high-frequency sounds up to 10 kHz. Potential contributors to the neurophonic in the barn owl NL include the afferent axons from NM, synapses from NM axons onto NL neurons, and NL neurons and their afferent axons. To narrow down the source(s) of the neurophonic in owl NL, we developed and applied a new analysis technique for tone-driven responses. More specifically, we used the signal-to-noise ratio (SNR) to quantify the neurophonic potential in a way that is independent of its absolute amplitude and other characteristics, all of which may vary considerably across different recordings and different animals. We then modeled the neurophonic potential as a sum of the contributions from different sources, taking into account physiological boundary conditions in NL. Such a model allowed us to numerically simulate the neurophonic potential and to analytically calculate its properties such as the SNR, and its dependence upon model parameters. A quantitative comparison of model and experiment then led to a lower bound for the number of statistically independent sources that must contribute to the neurophonic potential. Finally, we were also able to estimate the spatial range over which an electrode collects a signal by including the different geometries related to axonal, synaptic, and somatic sources in the model.

## 4.3. Materials and Methods

### 4.3.1. Experimental paradigm

Owl data were recorded as explained in the Appendix B (Neurophonic Recordings). Data set 1 was analyzed for the results following. The anatomical analyses are described in the section B.3.

### 4.3.2. Analysis of the measured neurophonic

#### Fourier transform and power spectral density

To characterize the neurophonic, we calculated the Fourier transform for time-discrete data points $x_l$ where $l = 1, ..., n$ is a sample index and $n$ is the total number of samples. For a time resolution $\Delta_t$ and $T = n\ \Delta_t$ being the width of the analyzed time window, the Fourier transform of $x_l$ is

$$\tilde{x}_f = \sqrt{T}\frac{1}{n}\sum_{l=1}^{n} x_l \exp(-i\ 2\pi\ l\ f\Delta_t) \quad , \tag{4.1}$$

where the frequency $f$ is an integer multiple of $1/T$. The frequency resolution therefore depends on the length $T$ of the analyzed time window; we always took an 80-ms time interval, which corresponds to a frequency resolution of 12.5 Hz. Also the stimulus frequencies were always multiples of 12.5 Hz. The temporal resolution of the recorded data was $\Delta_t = 1/48077$ s or 20.80 $\mu$s. The data were re-sampled to $50,000$ Hz (MATLAB-function 'interp1' with default settings, MathWorks, Natick, MA) to have an integer number of samples in the 80-ms segment.

The power spectral density (PSD) at frequency $f$ is the square of the absolute value of the Fourier transform,

$$P(f) = |\tilde{x}_f|^2 \quad . \tag{4.2}$$

The PSD has units of the data squared, divided by frequency; for example, $\mathrm{mV}^2/\mathrm{kHz}$ for the EFP. We calculated the PSD using the MATLAB-function 'periodogram'.

In our recordings of the neurophonic in the barn owl NL, the largest response amplitude was typically obtained when the stimulus frequency was close to the best frequency (BF, see definition in the section 4.4) at the recording site. Only those recording sites at which the PSD showed a clear, distinct peak at that particular stimulus frequency, were accepted for further analysis. A response peak in the PSD of at least 0.16 $\mathrm{mV}^2/\mathrm{kHz}$ was needed to fulfill this criterion.

### Signal-to-noise ratio

The signal-to-noise ratio (SNR) is the ratio of the signal PSD to that of the noise PSD. For tonal stimuli, we assumed to find the signal PSD at the stimulus frequency, $f = f_{\text{stim}}$, and the noise PSD at neighboring frequencies $f \neq f_{\text{stim}}$. Thus,

$$\text{SNR}(f) = \frac{P(f_{\text{stim}})}{P(f)} \quad \text{for } f \approx f_{\text{stim}} \text{ but } f \neq f_{\text{stim}} \quad . \tag{4.3}$$

To estimate the noise level, we averaged the noise PSD amplitudes over an interval of 1 kHz around the stimulus frequency. The signal level is defined as the PSD level at the stimulus frequency minus the noise level.

We have defined signal and noise in the frequency domain, but separation of the two components is also possible in the time domain. The common way to extract the signal component from a response in the temporal domain is to average over many trials obtained with an identical stimulus. This procedure reduces the noise while retaining the signal. However, here we recorded only $3-5$ trials for each stimulus frequency at each site. An average over such a low number of trials was insufficient to considerably reduce the noise. Therefore, we took advantage of having periodic stimuli (tones with frequency $f_{\text{stim}}$): each trial contained many stimulus cycles of length $1/f_{\text{stim}}$, typically hundreds.

To estimate the signal, we selected an 80-ms interval of the response to be analyzed, for example from 10 ms to 90 ms after stimulus onset. The signal component was assumed to be cyclic with period $1/f_{\text{stim}}$. To average across cycles of a waveform that had a sampling frequency of 50,000 Hz, we re-sampled the 80-ms interval to 10, 20 or 40 sampling points per stimulus period; for $f_{\text{stim}} > 5$ kHz, we used only 10 or 20 sampling points per period. Re-sampling enabled us to average the response cycle-by-cycle (as well as across trials), which yielded the 'cyclic-mean' waveform (Fig. 4.4 B). Using the cyclic-mean waveform, we generated a signal waveform of 80 ms length by concatenating identical copies of the cyclic-mean and restoring the original sampling frequency (Fig. 4.4 C). To extract the noise, we subtracted the 80-ms signal waveform from the original response (Fig. 4.4 D).

## 4.3.3. Computational model of the neurophonic in NL

One aim of modeling the neurophonic potential was to numerically simulate a voltage signal that resembles the experimentally measured one. A similar model has been used by Ashida et al. (2007) to analyze the intracellular potential in NL neurons. Here we describe the time course of the extracellular field potential $V(t)$ as the sum of waveforms from $N$ sources,

$$V(t) = \sum_{n=1}^{N} A_n \sum_i k_n(t - t_{i,n}) \quad , \tag{4.4}$$

where $t$ is time and $A_n$ is the relative amplitude of source $n$ for $n = 1, ..., N$. The symbol $k_n$ denotes the time-dependent kernel describing the spike waveform associated with the source $n$, and $t_{i,n}$ is the time of the $i^{th}$ spike of source $n$. In what follows, we drop the index $n$ of the kernel and consider only one source type, i.e., one spike waveform, at a time.

The distributions of amplitudes $A_n$ were chosen to simulate two cases. In the first and simplest case, amplitudes $A_n$ were identical for all sources, i.e., there was no distance dependence decay of amplitudes. In such an idealized scenario, all sources were located at a similar distance from the tip of the electrode. In the second case, we assumed a spatially uniform distribution of sources. Furthermore, the amplitude of a source decayed with its distance $r$ from the electrode tip. For a neuronal dipole, the generic geometric configuration of a cell where current sink and source are spatially separated, the amplitude $A_n(r)$ was proportional to $1/r^2$ (Logothetis et al., 2007) for large $r$.

The kernel function $k(t)$ was chosen such that its PSD roughly matched the measured PSD in

Figure 4.3D. The kernel's phase spectrum was estimated from typical extracellular spike waveforms as presented, for example, by Gold et al. (2006). To fulfill these criteria in a simple model, we approximated the shape of the spike waveform $k$ with a Gabor function

$$k(t) \propto \exp\left(-\frac{t^2}{2\rho^2}\right)\cos(2\ pi\ f_g\ t + \phi) \quad , \tag{4.5}$$

with width $\rho = 0.09$ ms, oscillation frequency $f_g = 3.9$ kHz, and phase $\phi = 0.8$ rad (Fig. 4.6B). Absolute peak amplitudes of the kernels were in the range of 100 $\mu$V (Gold et al., 2006). We assumed that the shapes of the kernels k are equal for all sources of one specific type (axon, synapse, or neuron). Any filtering resulting from the experimental setup was assumed to be included in the form of the kernel, i.e., the form of the kernel was assumed to undergo the same filtering as the data. Furthermore, we neglected the small equipment noise included in the spectrum.

The time $t_{i,n}$ denotes spike number $i$ in source $n$. Spikes were generated through an inhomogeneous Poisson process with a time-dependent rate $p(t)$. To describe the sustained phase of a neurophonic driven by a monaural tone at frequency $f_{\text{stim}}$, we accounted for three constraints as motivated by the physiology of NL: First, the time-dependent rate $p(t)$ oscillated with the stimulus frequency $f_{\text{stim}}$. Second, spikes were phase locked to the stimulus with some vector strength. Because different sources could be locked to a tonal stimulus at different absolute phases, the resulting vector strength of spikes from a population of sources might be smaller than the individual vector strengths of single sources. To take such a phase jitter into account, we described phase locking by a population vector strength $v$ (also called synchronization index), which was then taken as the vector strength of each source where all sources were assumed to be locked to the same stimulus phase. Third, we assumed that spikes in all sources were mutually independent, i.e., each individual source generateds spikes according to an inhomogeneous Poisson process.

To describe the spiking probability for a tonal stimulus at frequency $f_{\text{stim}}$, we used a $1/f_{\text{stim}}$ -periodic sum of Gaussian functions (wrapped Gaussian function as, e.g. in Fig.4.6A; see also Jammalamadaka and SenGupta (2001)) forming the Poisson rate

$$p(t) = \frac{\lambda}{f_{\text{stim}}} \sum_{m=-\infty}^{\infty} G_\sigma(t - \frac{m}{f_{\text{stim}}}) \quad , \tag{4.6}$$

where $\lambda$ is the mean rate of the Poisson process, $m$ is running numbering of the Gaussians and

$$G_\sigma(x) = \frac{1}{\sigma\sqrt{2\pi}} \exp\left(-\frac{x^2}{2\sigma^2}\right)$$

denotes a normalized Gaussian with zero mean and standard deviation (SD) $\sigma > 0$. The phase locking of spikes, as quantified by the vector strength $v$, was related to the width $\sigma$ of the Gaussian through (Kempter et al., 1998b):

$$v = \exp\left[-\frac{1}{2}\left(2\pi f_{\text{stim}}\right)^2 \sigma^2\right] \quad . \tag{4.7}$$

To describe the spontaneous activity in the absence of a tonal stimulus, we took $v = 0$, that is, the Poisson firing rate is constant: $p(t) = \lambda$. Numerical simulations of these computational models of the neurophonic in NL are illustrated in Figs. 4.6, 4.7, 4.9 and 4.10.

### 4.3.4. Mathematical analysis of the computational model

To interpret the measured neurophonic data, we compared it to the simulated neurophonic. It was important to know how, for example, the cyclic-mean amplitude and the SNR of the simulated neuro-

phonic depended on simulation parameters, i.e. the spike waveform $k$, the population vector strength $v$, the stimulus frequency $f_{\text{stim}}$, the number $N$ of sources and their mean firing rate $\lambda$. Model spikes were generated by an inhomogeneous Poisson process. To understand the behavior of the numerical simulations of the model, we analyzed the model mathematically.

The analysis was simplest for kernels being equal for all sources. The expected amplitude of the cyclic-mean response was approximated by the amplitude $a$ of the first harmonic, that is, the Fourier transform at $f = f_{\text{stim}}$. of the simulated neurophonic. This approximation was reasonable for $v$ less than about 0.5 because then higher harmonics could be neglected. With the definition of the Fourier transform in Eq. (4.1), we found that the amplitude $a$ is (Kempter et al., 1998b)

$$a = 2N\lambda v|\tilde{k}(f_{\text{stim}})| \quad , \tag{4.8}$$

indicating its linear dependence on $N$, $\lambda$, and $v$ (Fig. 4.7B). Note that the Fourier transform of a square-integrable function, for example the spike waveform $k$, is defined as

$$\tilde{k}(f) = \int_{-\infty}^{+\infty} k(t)\ \exp(-i\ 2\pi\ f\ t)\ \mathrm{d}t \quad . \tag{4.9}$$

In the following equations, the absolute value of this Fourier transform is important in order to derive PSDs. For a kernel as in Figure 4.6B with a peak amplitude of 100 $\mu$V, we obtained $|\tilde{k}(5\text{ kHz})| = 1.46 \cdot 10^{-2}$ mV/kHz.

Since the signal power at the stimulus frequency $f_{\text{stim}}$ was equal to $T \cdot a^2/4$ (derived from Eqs. (4.1) and (4.2) for a sinusoidal signal with an amplitude $a$), we then found from Eq. (4.8) that the PSD at the stimulus frequency, $f = f_{\text{stim}}$, is

$$P(f_{\text{stim}}) = N^2\lambda^2 v^2 |\tilde{k}(f_{\text{stim}})|^2 T \quad , \tag{4.10}$$

where $T$ is the duration of the analyzed response, which is 80 ms throughout this paper. For $f \neq f_{\text{stim}}$, the PSD could be calculated similarly[2] (see also Snyder and Miller (1991)) but had a different dependence on the parameters. In summary, we found

$$P(f) = \begin{cases} N^2\lambda^2 v^2 |\tilde{k}(f)|^2 T & \text{for} \quad f = f_{\text{stim}} \\ N\lambda |\tilde{k}(f)|^2 & \text{for} \quad f \neq f_{\text{stim}} \end{cases} \quad . \tag{4.11}$$

From the definition of the SNR in Eq. (4.3) we found

$$\text{SNR} = N\lambda v^2 T \quad . \tag{4.12}$$

Note that the SNR is independent of the kernel $k$. The SNR linearly depends on the number $N$ of independent sources (Fig. 4.7A) and the mean population firing rate $\lambda$, and quadratically depends on the vector strength $v$. Similar analytical expressions of the SNR for inhomogeneous Poisson spike trains have been derived previously in the context of stochastic resonance (e.g. McNamara and Wiesenfeld (1989); Wiesenfeld et al. (1994); Gammaitoni et al. (1998); Shimokawa et al. (1999); Hohn and Burkitt (2001); Lindner et al. (2009)). Because the rate $\lambda$ and the vector strength $v$ may depend on the stimulus frequency $f_{\text{stim}}$ , the SNR may also depend on $f_{\text{stim}}$, as seen in SNR tuning curves (Fig. 4.4F).

Solving Eq. (4.12) for $N$, we obtained

$$N = \frac{\text{SNR}}{\lambda v^2 T} \quad , \tag{4.13}$$

which allowed us to estimate the number $N$ of sources that contribute to the neurophonic from

[2]The PSD of the noise spectrum is derived in Appendix A.1

experimentally accessible quantities. We note that $N$ in Eq. (4.13) provides a lower bound; weakening the model assumptions, for example by allowing that the kernels are different for different sources or that sources are not independent, only increased the necessary number of sources to reach a certain SNR, even if $\lambda$, $v$, and $T$ are unchanged.

To demonstrate the effect of non-identical kernels for different sources, we analytically calculated the cyclic-mean amplitude $a$ and the SNR for the case of distance-dependent kernel amplitudes $A_n(r)$. We therefore assumed a uniform distribution of sources in space. The density of the sources is $3/(4\pi r_S^3)$, where $2 \cdot r_S$ is a measure for the mean distance between neighbors. We further assumed that the kernel of a source at distance $r_S$ from the electrode had the form $k(t)$ and relative amplitude $A_n(r_S) = 1$; cf. Eq. (4.4). We finally assumed that the kernel amplitudes decreased with distance $r$ to the electrode via $1/\mathrm{r}^2$ (Logothetis et al., 2007), that is, $A_n(\mathrm{r}) = (r_S/\mathrm{r})^2$, but the waveform $k(t)$ remained unchanged.

We derived the resulting cyclic-mean amplitude a in two steps. First, we calculated the amplitude resulting from a thin spherical shell around the electrode, and, second, we added contributions from shells. A shell at radius $r$ and with infinitesimal thickness $\mathrm{d}r$ had a volume $4\pi\ r^2\mathrm{d}r$. Multiplying this volume by the density $3/(4\pi\ r_S^3)$ of sources resulted in $3r^2\mathrm{d}r/r_S^3$ sources. The sources' amplitude was $(r_S/r)^2$ , and amplitudes of all sources were equal because they were at equal distance $r$ from the electrode. The resulting contribution $\mathrm{d}a$ to the total amplitude was

$$\mathrm{d}a = 6\frac{\mathrm{d}r}{r_S}\lambda v|\tilde{k}(f_{\mathrm{stim}})| \quad . \tag{4.14}$$

This equation is analogous to Eq. (4.8), in which we replaced the number $N$ of sources by $3r^2\mathrm{d}r/r_S^3$ and the amplitude factor 1 by $(r_S/r)^2$. We integrated this equation to sum up contributions of sources within a sphere of radius $R$, which yielded the expected amplitude $a$ of the first harmonic of the summed signal,

$$a(R) = 6\frac{1}{r_S}\lambda v|\tilde{k}(f_{\mathrm{stim}})| \int_{r_S}^{R} \mathrm{d}r \quad . \tag{4.15}$$

The upper integration limit was $R$, which typically was much larger than $r_S$. As the lower integration limit we chose $r_S$, and not 0. The difference is negligible for large numbers of sources; however, this choice was necessary to avoid divergent integrals in the calculation of the noise power at distances $r < r_s$ at which the $1/r^2$ dependence of amplitudes does not hold (see below). Therefore, the expected cyclic-mean amplitude is

$$a(R) = 6\ \lambda\ v|\tilde{k}(f_{\mathrm{stim}})| \left(\frac{R}{r_S} - 1\right) \tag{4.16}$$

where $R/r_S = N^{1/3}$ connects the radius $R$ of the sphere to the number $N$ of sources within this sphere (Fig. 4.7B). The signal power at the stimulus frequency $f_{\mathrm{stim}}$ was, as before, equal to $T \cdot a(R)^2/4$, and thus

$$P(f_{\mathrm{stim}}) = 9\ \lambda^2\ v^2\ |\tilde{k}(f_{\mathrm{stim}})|^2 \left(\frac{R}{r_S} - 1\right)^2\ T \quad . \tag{4.17}$$

It increased almost quadratically with increasing R, and therefore was *global*.

To calculate the noise power, we summed noise contributions from thin spherical shells, similar to above approach for the amplitude. By analogy to Eq. (4.11) for $f \neq f_{\mathrm{stim}}$ , we replaced the number $N$ of sources by $3r^2\mathrm{d}r/r_S^3$ and the amplitude factor 1 by $(r_S/r)^4$ , where the 4th power accounts for the fact that we summed up noise powers (and not amplitudes). An integration yielded the noise power

$$P(f) = 3\ \lambda\ |\tilde{k}(f)|^2 \int_{r_S}^{R} \frac{r_S}{r^2}\mathrm{d}r = 3\ \lambda\ |\tilde{k}(f)|^2 \left(1 - \frac{r_S}{R}\right) \quad , \tag{4.18}$$

which saturated with increasing $R$, and was therefore *local*. Then, the signal-to-noise ratio was

$$\mathrm{SNR} = 3\ \lambda\ v^2\ T \frac{R}{r_S}\left(\frac{R}{r_S} - 1\right) \quad . \tag{4.19}$$

Because $N = (R/r_S)^3$, we found from Eq. (4.19) the dependence of the SNR on $N$:

$$\mathrm{SNR} = 3\ \lambda\ v^2\ T N^{1/3}\left(N^{1/3} - 1\right) \tag{4.20}$$

for $N\ >\ 1$ (Fig. 4.7A), or, equivalently,

$$N = \frac{1}{8}\left(1 + \sqrt{1 + \frac{4 \cdot \mathrm{SNR}}{3\ \lambda\ v^2\ T}}\right)^3 \tag{4.21}$$

## 4.4. Results

In this manuscript, we characterize the general structure of the neurophonic potential in the nucleus laminaris (NL) of owls, using newly developed analysis tools. We derive a computational model that explains its most salient properties. Finally we focus on the possible origin of the neural responses.

### 4.4.1. Properties of the neurophonic

We analyzed extracellular field potential (EFP) recordings from 378 sites in the auditory brainstem of 6 anesthetized barn owls. Neurophonic responses to tones were recorded in the mid-to-high best frequency (BF) region ($>$ 2.5 kHz) of the tonotopically organized NL. When the frequency of the tonal stimulus was close to the BF at the recording site, the response typically contained a strong oscillatory component (Fig. 4.1A, B). For the quantitative analysis, we only accepted recording sites that exhibited a response peak in the power spectral density (PSD) of at least 0.16 $\mathrm{mV}^2$/kHz (see section 4.3 for details). Responses at 47 sites did not fulfill this criterion, leaving responses at 331 sites. All but one of the recording sites with non-oscillatory responses were from the same owl (owl 120).

#### General temporal structure of the neurophonic potential

After a short transient response at the onset (Fig. 4.1B), the driven response reached a tonic level that lasted for the duration of the stimulus (Fig. 4.1C). The neurophonic potential was notable for both its coherence and large amplitude, and displayed a smooth time course without unitary events; single units could not be isolated. After the end of the tonal stimulus, the spontaneous activity was reduced for about ten milliseconds (Fig. 4.1D) before it returned to the pre-stimulus level. The spontaneous activity was smaller in amplitude than the driven activity (Fig. 4.1E). In what follows we focus on the sustained responses and analyze 80-ms intervals from 10 to 90 ms after stimulus onset (black line in Fig. 4.1A) and 10 to 90 ms after the stimulus offset at 100 ms.

#### Amplitude of the neurophonic potential in the time domain

To quantify the magnitude of the EFP amplitude, we used the standard deviation (SD). In the example shown in Figure 4.1, the SD of the sustained component of the neurophonic potential, averaged over the 80-ms interval, was 0.34 mV. For the whole sample, when the stimulus frequency was equal to the BF of each recording site, the SD varied between 0.02 mV and 2.66 mV with a median of 0.37 mV (Fig. 4.2A).

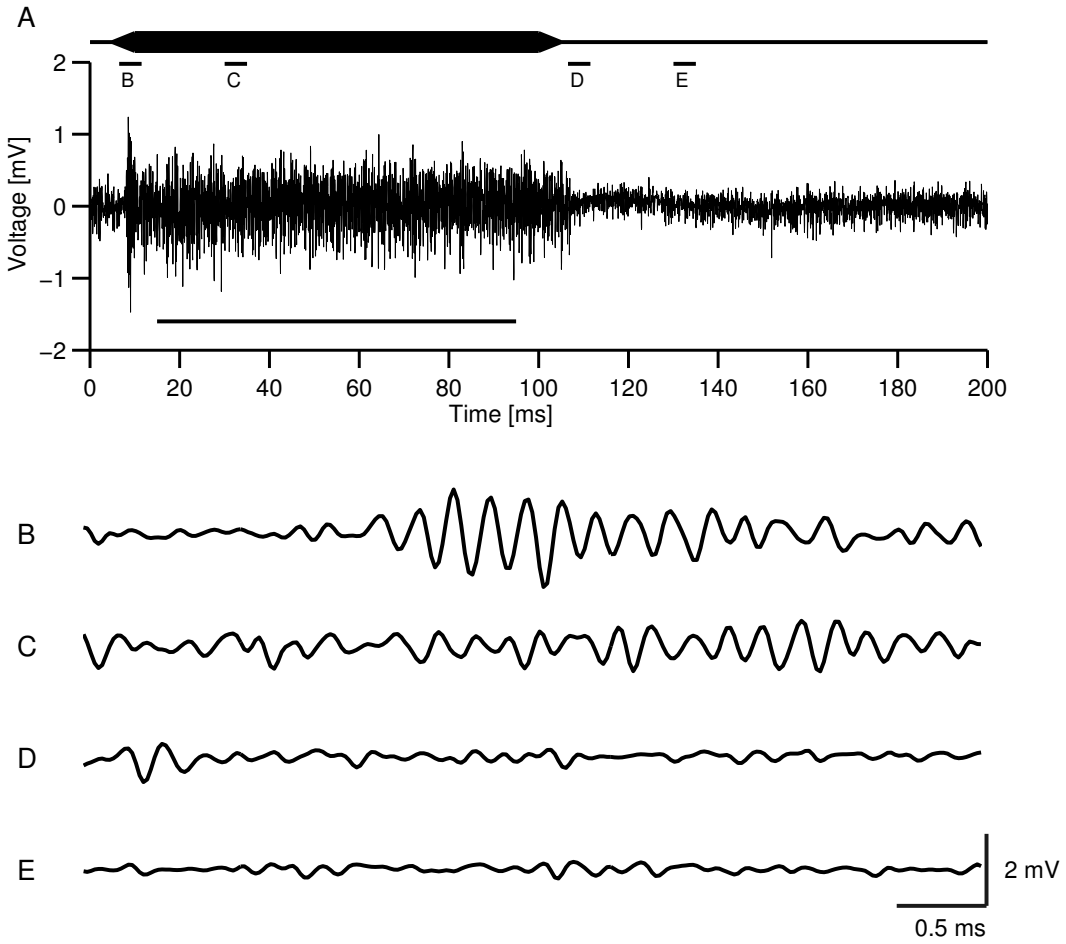


Figure 4.1.: Neurophonic potential. *A:* Stimulation scheme (top) and response (bottom). The black line at the bottom shows the segment of the response analyzed in this manuscript. *B–E:* Five-millisecond intervals of the neurophonic (as labeled in *A*) at an expanded time scale. *B:* Response onset, $1.5 - 6.5$ ms after stimulus onset. *C:* Driven response, $25 - 30$ ms after stimulus onset. *D:* Recovery, $1.5 - 6.5$ ms after stimulus offset. *E:* Spontaneous activity, $25 - 30$ ms after stimulus offset. The example shown is from recording site 17.10 in owl 502 for a tonal stimulus at 5.0 kHz and intensity of 60 dB SPL.

Likewise, the spontaneous activity was characterized by its SD (average over all repetitions of 80-ms intervals: 0.15 mV in Fig. 4.1). For the whole sample, the SD of the spontaneous activity varied between 0.01 mV and 0.97 mV with a median of 0.17 mV (Fig. 4.2B). The SDs for driven (at BF) and spontaneous activity (Fig. 4.2A and B) were highly correlated ($r = 0.946$, $p < 10^{-100}$). Both distributions of the SD had several modes because values in different owls covered different ranges, possibly also because of variation in electrode impedance. This high variability of the SD impedes a direct comparison of the EFP across animals. The analysis tools developed later in this manuscript overcome this problem.

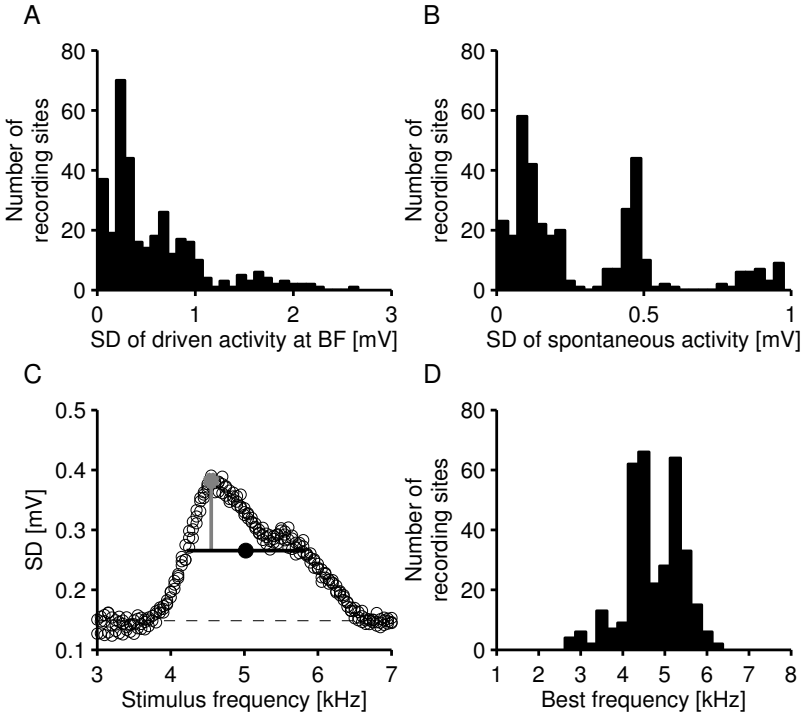


Figure 4.2.: Response amplitudes and frequency tuning. *A, B:* Histograms of SDs of *A* the tone-driven, and *B* the spontaneous activity for all analyzed recording sites ($n = 331$). For both driven and spontaneous activities, 80-ms intervals were analyzed. For the driven activity, the stimulus frequency was equal to the best frequency of that recording site. *C:* Iso-intensity tuning curve of recording site 17.10 in owl 502; SD of the neurophonic 15–95 ms after stimulus onset as a function of stimulus frequency. The maximum SD (0.38 mV at 4.55 kHz) is marked with a light gray circle and a vertical gray line. The horizontal continuous line shows the width (1.61 kHz) of the curve at half-height (SD = 0.27 mV), and the black dot indicates the mid-point of the line, which defines the BF (5.02 kHz). The horizontal dashed line depicts the level of SD of spontaneous activity ($0.149 \pm 0.004$ mV). Stimulus frequencies ranged from 3 to 7 kHz with 50 Hz resolution. *D:* Histogram of all BFs ($n = 331$).

## Best frequencies

Iso-intensity tuning curves were assembled to further characterize recording sites: We derived SDs of the neurophonic in response to stimulation with tones at different frequencies (Fig. 4.2C). In general, the SDs as a function of the stimulus frequency showed a clear maximum and a monotonic decay on both sides of the maximum until the spontaneous level was reached. At some recording sites, like the one shown in Figure 4.2C, the decrease was non-monotonic and had a second, smaller peak.

Iso-intensity tuning curves defined the BF at a recording site as follows: a line at half height of a tuning curve was derived from its peak value and the mean value of the spontaneous levels. The midpoint of the line at half height yielded the BF, which was 5.0 kHz in the example shown in Figure 4.2C. The BFs in the whole sample ranged from 2.8 to 6.3 kHz (mean ± standard deviation: $4.7 \pm 0.7$ kHz, Fig. 4.2D). Furthermore, there was a low but significant correlation between the BF and SD at BF ($r = 0.26$, $p < 10^{-6}$); however, the distribution of BFs was unimodal. In the following, further properties of the neurophonic will be derived for tonal stimulation at the BF if not stated otherwise.

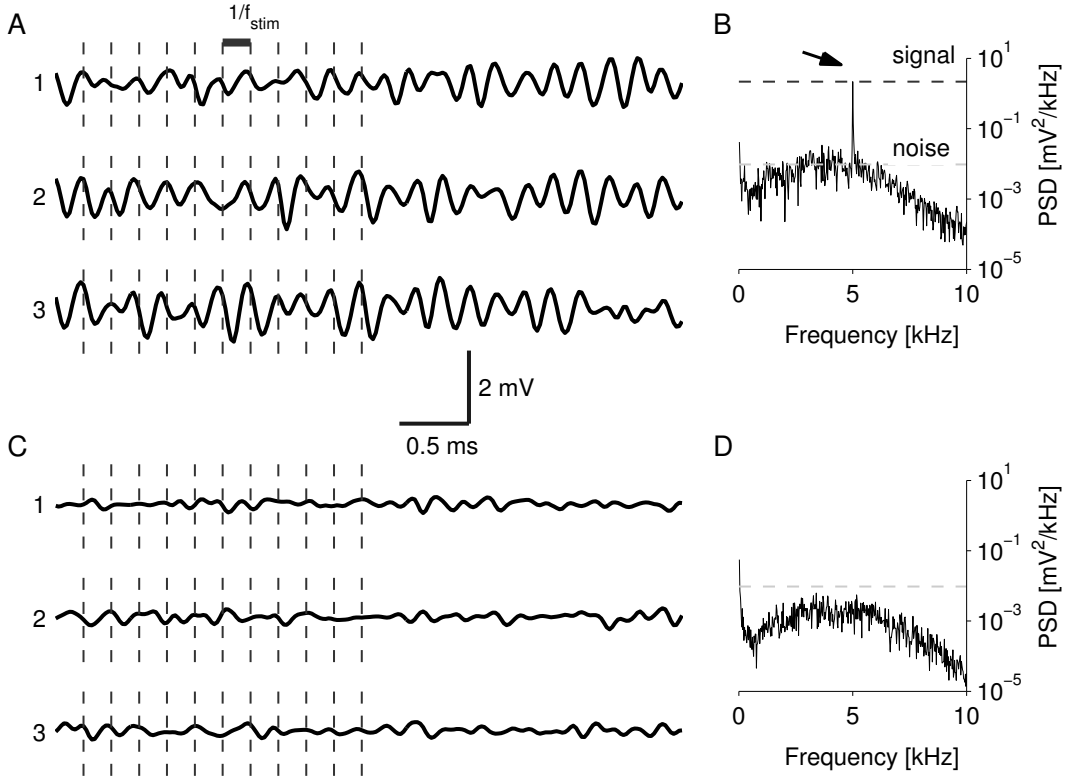


Figure 4.3.: Trial-to-trial variability in driven and spontaneous activity and power spectral density (PSD) of the neurophonic. *A:* Three repetitions of the driven response, 25–30 ms after stimulus onset. *B:* Mean PSD of the driven response in *A*, based on activity 15–95 ms after the onset of the tone; note the large signal peak at the stimulus frequency $f_{\mathrm{stim}}$ (arrow and black dashed line at 2.18 $\mathrm{mV}^2$/kHz) and the average noise level (gray dashed line at 0.01 $\mathrm{mV}^2$/kHz). *C:* Spontaneous activity at the same recording site as in *A*, 25–30 ms after stimulus offset. *D:* Mean PSD of the spontaneous response. The dashed line shows the same level as in *B* (noise). The shown example is from recording site 17.10 in owl 502. In *A* and *B*, a tonal stimulus at 5.0 kHz at intensity of 60 dB SPL was applied.

### Amplitude of the neurophonic potential in the frequency domain

In response to tones at BF, the time course of the neurophonic was similar across trials. In particular, responses were locked to the periodic stimulus (Fig. 4.3A), while spontaneous activity was not coherent (Fig. 4.3C).

To characterize the phase locking of the EFP, we computed the power spectral density (PSD, in units of $\mathrm{mV}^2$/kHz). In the example depicted in Figure 4.3B, the PSD exhibited a large peak at the stimulus frequency ('signal level'). The level of the PSD in this frequency bin was 2.181 $\mathrm{mV}^2$/kHz, much larger than the average level in surrounding frequency bins ('noise level', about 0.01 $\mathrm{mV}^2$/kHz ).

Let us briefly discuss the shape of the PSD as a function of frequency, disregarding the signal peak. In the example shown in Figure 4.3B, the level increased from 0.5 to 3 kHz by about one order of magnitude, had a shallow maximum between 3 and 5 kHz, and decreased by about two orders of magnitude from 5 to 10 kHz, which was the highest frequency considered in this analysis. The PSD was noisy and did not

display any further salient features. Spectra obtained at other recording sites had similar properties.

The PSD of the spontaneous activity (Fig. 4.3D) closely resembled the shape of the PSD of the driven activity (Fig. 4.3B), apart from the absence of the peak at the stimulus frequency. The average level was lower in the spontaneous PSD: about $2.5 \cdot 10^{-3}$ mV$^2$/kHz at 5 kHz. Similar shapes but different levels of driven (without the signal peak) and spontaneous PSDs were also typical for the whole sample.

### Separation of signal and noise

We separated the signal and the noise in the time domain, even though the separation in the frequency domain would be equivalent for responses in which the signal is sinusoidal (see section 4.3 for details). The separation yielded the cyclic-mean response in the temporal domain, as well as the level of the signal and the noise PSDs in the frequency domain. In the example shown in Figure 4.4A-C, the amplitude of the sinusoidal cyclic-mean response was 0.32 mV. In the population, the cyclic-mean amplitude ranged from 0.01 mV to 2.80 mV with a median of 0.31 mV and an interquartile range of 0.44 mV.

The PSD of the reconstructed sinusoidal signal showed a dominant peak at the stimulus frequency $f_{\text{stim}}$ (Fig. 4.4C, right-hand side). The height of this peak was, by definition, identical to the peak of the response PSD minus the noise level (signal level 2.17 mV$^2$/kHz = 2.18 − 0.01 mV$^2$/kHz). There was also a smaller peak at the frequency of the first harmonic ($1 \cdot 10^{-4}$ mV$^2$/kHz at 2 $f_{\text{stim}} = 10$ kHz). The level of the first harmonic was only −45 dB (or 0.003%) compared to the signal level at $f_{\text{stim}}$, indicating a highly sinusoidal signal. In the whole population of 331 recording sites, the cyclic-mean response at BF was almost always sinusoidal: the level of the second harmonic was less than −20 dB with respect to the fundamental in all but 10 cases. The median level of the second harmonic was −47 dB in comparison to the fundamental, with an interquartile range of 12.3 dB.

The spectrum of the noise (Fig. 4.4D, right hand side) showed all components of the response's PSD except the large peak at $f_{\text{stim}}$. The noise level was obtained from the average over 41 data points (corresponding to 1 kHz) of the PSD around the stimulus frequency and an average over all trials ($9.61 \cdot 10^{-3}$ mV$^2$/kHz, dashed line in Fig. 4.4D, right-hand side).

To further characterize the neurophonic at a recording site, tuning curves of signal and noise levels were assembled. To this end, we measured signal levels and noise levels at one recording site for various values of the stimulus frequency $f_{\text{stim}}$ (Fig. 4.4E). In general, the signal level was larger than the noise level for stimulus frequencies around the BF of the recording site; the signal level showed a maximum near the BF, and declined (usually monotonically) at both sides of the maximum. The shape of the tuning curve in Figure 4.4E was similar to the tuning curve derived from the SDs (Fig. 4.2C, note the logarithmic ordinate scale in Fig. 4.4E).

The separation of signal and noise enabled us to calculate the signal-to-noise ratio (SNR). The SNR provided the best measure to quantify the neurophonic. For the recording site described in Figure 4.4A–D with responses driven by a tonal stimulus at frequency $f_{\text{stim}} = 5.0$ kHz, the SNR was 412.7, corresponding to 26.2 dB (Fig. 4.4F). The frequency at which the highest SNR occurred was lower than the BF (maximum SNR of 28.1 dB achieved at $f_{\text{stim}} = 4.4$ kHz) in this example.

### Signal level, noise level, and signal-to-noise ratio in the whole sample

In our population of 331 recording sites, tonal stimuli at the BF led to PSDs with signal and noise levels that covered wide ranges of values. The signal levels varied over about seven orders of magnitude and ranged from $7.4 \cdot 10^{-4}$ to $2.7 \cdot 10^{2}$ mV$^2$/kHz. The noise levels varied over about four orders of magnitude and ranged from $3.0 \cdot 10^{-5}$ to $5.3 \cdot 10^{-1}$ mV$^2$/kHz (Fig. 4.5A). On the other hand, the SNR at the BF had a range of only three orders of magnitude: from 1 to 1071 with a median of 317. In a logarithmic scale, the range was from 0 to 31.2 dB with a median of 25.4 dB (Fig. 4.5B) and an interquartile range of 5.8 dB.

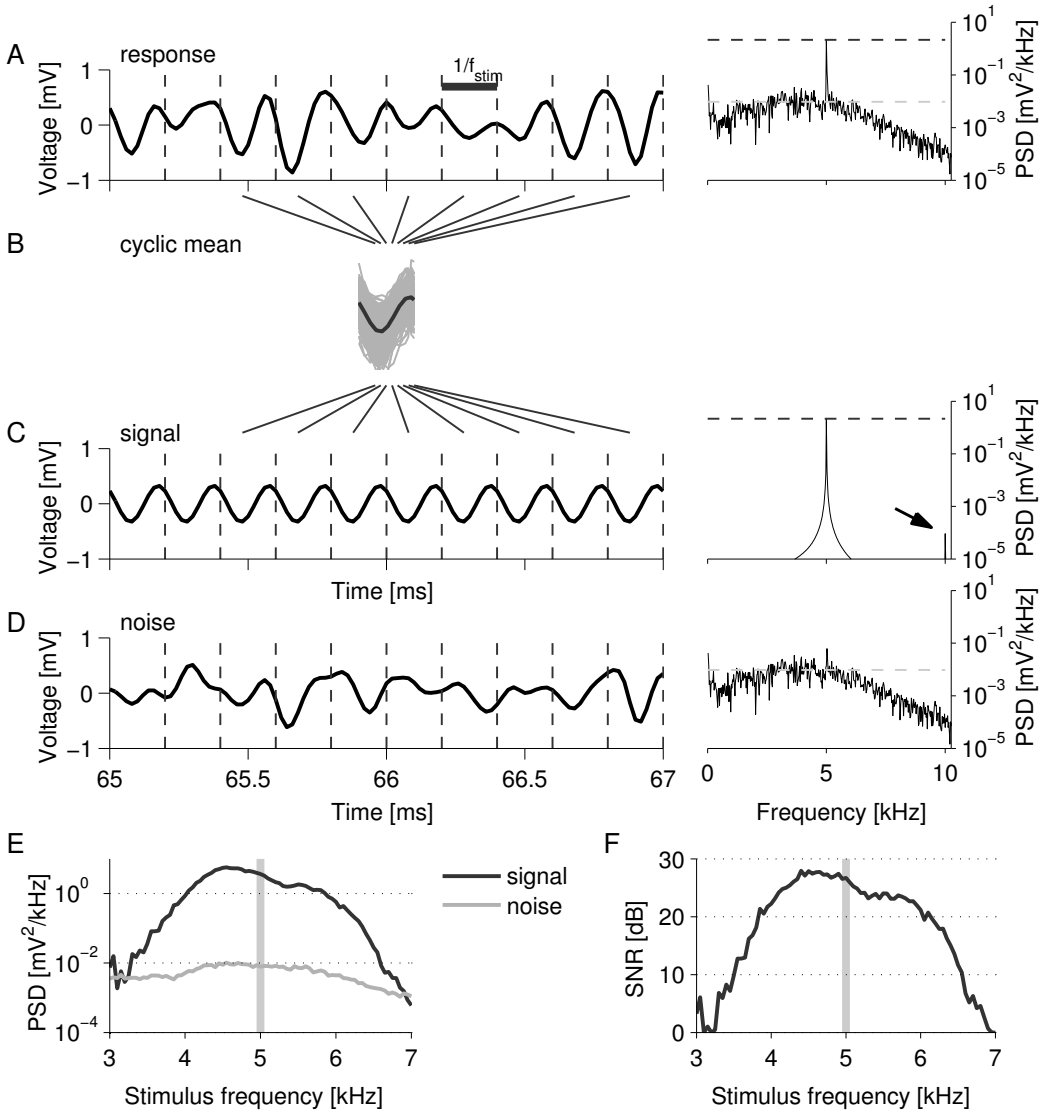


Figure 4.4.: Signal-to-noise ratio (SNR) of responses to tonal stimuli. *A:* Response: driven activity (left) and its PSD (right) for a tonal stimulus at frequency $f_{\mathrm{stim}} = 5.0$ kHz. The two horizontal dashed lines indicate the levels of the peak of the PSD at $f_{\mathrm{stim}}$ (signal) and the mean PSD around $f_{\mathrm{stim}}$ (noise). *B:* Cyclic-mean: a response is wrapped to one cycle (width $1/f_{\mathrm{stim}}$). The wrapped segments (gray lines) are averaged (cyclic-mean, black line). *C:* Signal: several cycles of the same cyclic-mean are shown in the time trace (left); the PSD (right) has a peak at $f_{\mathrm{stim}}$ and a smaller peak at the first harmonic frequency $2f_{\mathrm{stim}}$ (arrow). *D:* Noise (left) is derived by subtracting the signal in *C* from the response in *A*. Noise is calculated for each trial separately. The PSD of the noise (right) is an average over all trials. *E:* Signal and noise levels as a function of stimulus frequency. The vertical gray line indicates the stimulus frequency $f_{\mathrm{stim}} = 5.0$ kHz used in *A*. Stimulus frequencies range from $f_{\mathrm{stim}} = 3.0$ kHz to 7.0 kHz with 50 Hz steps. *F:* SNR (in units of dB) as a function of stimulus frequency. The example shown is from the recording site 17.10 in owl 502.

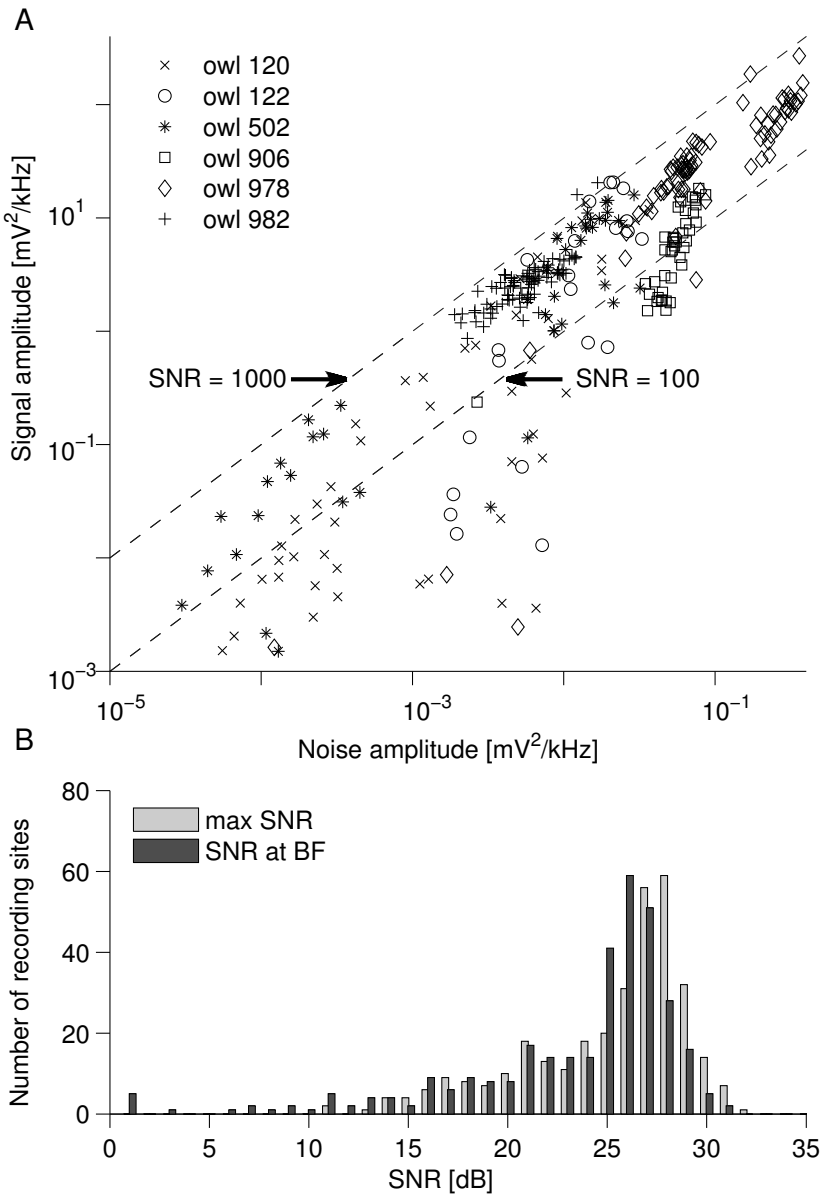


Figure 4.5.: Signal-to-noise ratio (SNR) of the neurophonic in six owls. *A:* Relation between PSD signal amplitudes and PSD noise amplitudes. At each recording site, the stimulus frequency was equal to the BF. The dashed lines shows SNRs of 100 and 1000. *B:* Histograms of maximum SNRs and SNRs at BF ($n = 331$).

Figure 4.5B also shows the distribution of the recording sites' maximal SNR. The highest value was 32.2 dB (range $10.9 - 32.2$ dB, median 26.6 dB, interquartile range 5.6 dB). The median of the maximum SNR was slightly larger (1.2 dB) than the median of the SNR at BF. Nevertheless, both distributions were similar. We conclude that the neurophonic potential in barn owl NL shows an exceptionally high SNR for tonal stimulation in the high-frequency ($> 2.5$ kHz) range.

### 4.4.2. Modeling the neurophonic

In this section, we address the question of how a neurophonic with a SNR of more than 30 dB and an amplitude in the range of 1 mV may be generated. To this end, we set up a computational model of the neurophonic, which was numerically simulated and then quantified in the same way as the experimental data. This comparison, together with a mathematical analysis of the model, then allowed us to constrain model parameters.

We will begin with a generic version of the model to illustrate its main features before we turn to a more detailed one. The detailed implementation of the models is described in the section 4.3. For the simplest possible model, we considered only one kind of source. We also assumed that all sources were mutually independent and that they contributed equally, i.e., with the same waveform and amplitude to the neurophonic. Furthermore, we modeled neuronal activity as an inhomogeneous Poisson processes; for the tone-driven neurophonic, we assumed a periodic firing rate (Fig. 4.6A). The probability that a homogeneous population of $N$ sources produces a spike in a small time interval was then proportional to this time-dependent firing rate. This rate was characterized by the stimulus frequency $f_{\mathrm{stim}}$, the vector strength $v$ of population phase locking, and the mean firing rate $\lambda$ for each of the $N$ sources. Spike trains generated in this way are shown in Figure 4.6C, D and E (top left) for three different numbers $N$ of sources. A convolution of the spikes with some kernel, for example the spike waveform in Figure 4.6B, yielded continuous voltage traces (Fig. 4.6C, D, E, bottom left).

Typical values of model parameters were motivated by physiological data from owl NL and NM. The population-mean vector strength was set to $v = 0.4$ for a stimulus frequency $f_{\mathrm{stim}} = 5$ kHz ((Köppl, 1997b), and the population-mean firing rate was set to $\lambda = 400$ Hz (Carr and Konishi, 1990; Peña et al., 1996). We did not consider spontaneous firing in the simplified model. Extracellular spike waveforms of sources within NL were not available. Therefore, the spike waveform, or kernel, was approximated by a Gabor function. The parameters of the Gabor were chosen so that its PSD roughly matched the shape of the measured noise spectrum in NL (Fig. 4.3D). Furthermore, the kernel was required to match generic extracellular spike waveforms (e.g. Gold et al. (2006)), and its amplitude was set to a typical value of 100 $\mu$V. The spike waveform in Figure 4.6B satisfied all criteria. Thus, all but one of the degrees of freedom were fixed in the simplest model, and the number $N$ of statistically independent sources was the only parameter that was varied in the simulations outlined in Figure 4.6.

#### Dependence of the simulated neurophonic on the number of sources

The temporal structure of the simulated neurophonic strongly depended on the number $N$ of sources. When only few sources were used, the singular spike waveforms could be identified ($N = 2$, Fig. 4.6C), and the neurophonic was not oscillatory at the stimulus frequency $f_{\mathrm{stim}} = 5$ kHz. Even $N = 20$ sources, as in Figure 4.6D, were insufficient to achieve the smooth oscillatory temporal course in the voltage trace seen in experiments (Fig. 4.3A). The simulated neurophonic was similar to owl data only for a large number of sources, for example $N = 200$ as in Figure 4.6E.

How does the number $N$ of independent sources affect the PSD? Clearly, the average level of the PSD increased with $N$ (Fig. 4.6C, D, and E, right column). The height of the spectrum's peak at the stimulus frequency and the SNR also increased with $N$. For two independent sources, the SNR was 10 dB; for 20 independent sources the SNR was 20 dB; and for 200 independent sources the SNR increased to 30 dB, suggesting a linear relationship.

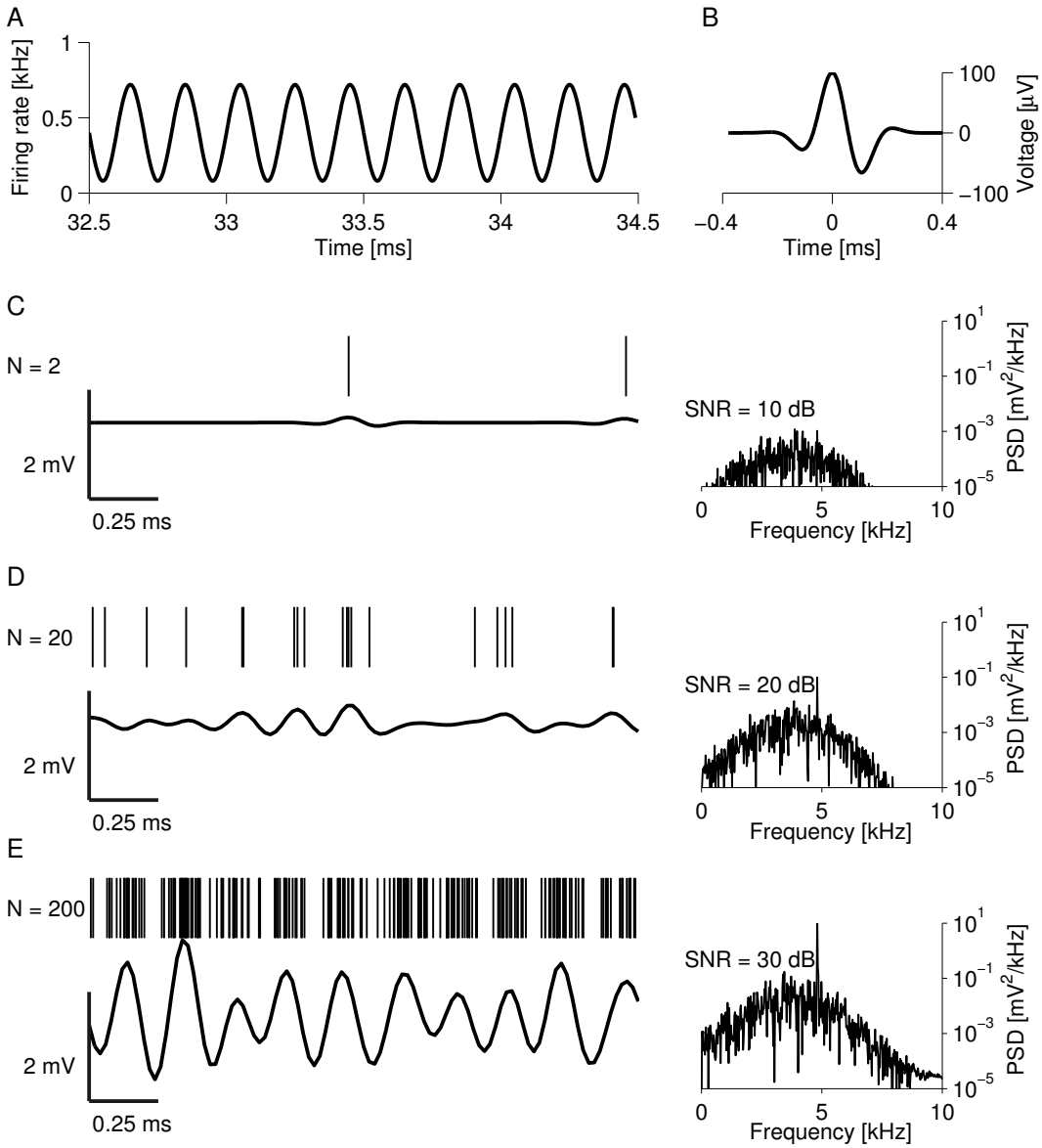


Figure 4.6.: Numerical simulations of neurophonic responses. *A:* Periodic firing rate. This rate was used in an inhomogeneous Poisson process to generate spike times as shown in *C, D* and *E*; see also section 4.3. *B:* Spike waveform (kernel). *C, D, E:* Neurophonic generated by different numbers $N$ of statistically independent sources. To produce a voltage trace (bottom left) from spike times (top left), each spike was convolved with the kernel in *B*, and contributions from different sources were summed. Right-hand side: PSDs based on 80-ms voltage traces. *C:* Simulation of 2 sources. *D:* Simulation of 20 sources. *E:* Simulation of 200 sources. Simulation parameters in *C–E*: vector strength $v = 0.4$, mean firing rate $\lambda = 400$ Hz, stimulus frequency $f_{\mathrm{stim}} = 5$ kHz.

Further numerical simulations in Figure 4.7A (grey symbols) as well as a mathematical analysis of the model (gray line; see also section 4.3) prove that SNR depends linearly on the number $N$ of independent sources. Equation (4.13) tells us that $N = 324$ independent sources were needed to reproduce the highest SNR observed in our recordings (32.2 dB). Further simulations (not shown) and analytical calculations verified that the SNR linearly depended on the firing rate $\lambda$, since the sum of $N$ Poisson sources with rate $\lambda$ was equivalent to one source with rate $N\lambda$. Finally, SNR depended quadratically on the vector strength $v$ and was independent of the shape and amplitude of the spike waveform (see also Eq. (4.12)), which supports the importance of the SNR as a useful measure.

Figure 4.7B demonstrates that the cyclic-mean amplitude depended linearly on $N$ (gray line and squares); see also Eq. (4.8). The cyclic-mean amplitude, however, also strongly depended on the spike waveform, in contrast to the SNR. With the waveform as shown in Figure 4.6B (amplitude 100 $\mu$V) and for 200 sources, the resulting cyclic-mean amplitude was in the range of one millivolt, as observed in experiments.

In this first simple model, we assumed that all sources contributed equally to the neurophonic, that is, all kernels were identical. Further simulations and mathematical analyses (not shown) indicated that any deviation from this special case of identical kernels only increased the necessary number of sources to reach a desired SNR. Thus, our simple model with identical kernels yielded a lower bound for the number of sources that are required to reach a certain SNR. To illustrate this behavior, we now turn to a different distribution of kernel amplitudes.

#### Distance-dependent attenuation of kernel amplitudes

The larger the distance $r$ between a source and the tip of an electrode, the smaller the source's contribution to the recorded potential. Therefore, an extended version of the model included the dependence of source amplitudes on distance. Specifically, we assumed that the shape of kernels remained unchanged, but that a kernel's amplitude was proportional to $1/r^2$, reasonable for electric dipoles (Logothetis et al., 2007).

In line with the homogeneous structure of NL, we considered a spatially uniform distribution of sources with some fixed density. Then we derived the SNR and the cyclic-mean amplitudes generated by $N$ sources within a spherical halo around the tip of an electrode (Eqs. (4.16) and (4.20), as well as black circles and lines in Fig. 4.7A and B).

Compared to above simple case of identical kernels, the $1/r^2$ dependence of kernel amplitudes considerably increased the number of sources that are necessary to achieve a given SNR (squares vs. circles in Fig. 4.7A). For example, we needed $N = 633$ sources in case of the $1/r^2$ dependence to reach an SNR of 30 dB, in contrast to only $N = 200$ sources for identical kernels. Moreover, the $1/r^2$ dependence dramatically decreased the cyclic-mean amplitude (Fig. 4.7B). For example, for $N = 200$ independent sources, the cyclic-mean amplitude decreased from 0.84 mV (for identical amplitudes in Eq. (4.8)) to 0.061 mV (for the $1/r^2$ dependence in Eq. (4.16)); in general, the ratio of the cyclic-mean amplitude of $N$ equal sources to the cyclic-mean amplitude of $N$ homogeneously distributed sources with an $1/r^2$ decay is $N/[3(N^{1/3} - 1)]$, which increases with increasing $N$.

### 4.4.3. Values of the numbers of sources in biologically motivated scenarios

So far we have outlined some generic features of the model. We now explore two specific scenarios of distributions of sources in greater depth. These scenarios are motivated by the anatomy and neurophysiology of the NL, and consider only one type of source at a time.

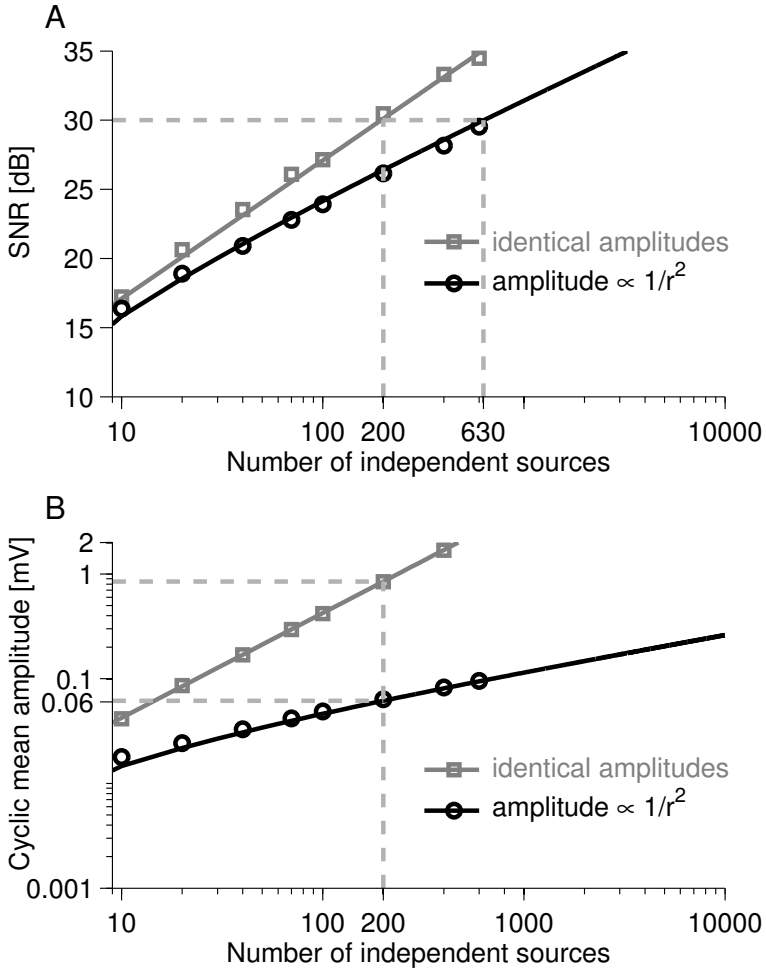


Figure 4.7.: Signal-to-noise ratio (SNR) and cyclic-mean amplitude in the Poisson model of the neurophonic. Gray lines and squares depict results for identical sources; black lines and circles indicate results for spatially evenly distributed sources with distance-dependent kernel amplitudes proportional to $1/r^2$). The solid lines show analytical results as described in section 4.3 'Materials and Methods'. The symbols indicate results obtained through numerical simulations. *A:* The SNR increased as a function of the number $N$ of sources; see also Eqs. (4.13) and (4.20). To reach an SNR of 30 dB, 200 identical sources are required. For the distance-dependent kernel amplitudes, 633 sources are required. *B:* The cyclic-mean amplitude increased as a function of $N$; see also Eqs. (4.8) and (4.16). The increase was linear in $N$ for identical sources, but proportional to $(N^{1/3} - 1)$ for distance-dependent kernel amplitudes. Simulation parameters: vector strength $v = 0.4$, mean firing rate $\lambda = 400$ Hz, duration of the analyzed response $T = 80$ ms. Kernels were as in Fig. 4.6B, either identical for all sources with amplitude 100 $\mu$V or distance-dependent with amplitude proportional to $1/r^2$; in the latter case, the amplitude was 100 $\mu$V at a distance of 50 $\mu$m, and the mean distance of neighboring sources was 100 $\mu$m.

### Anatomy and physiology of NL

In the NL, three possible types of sources may contribute to the extracellular potential: the nodes of Ranvier of the afferent NM axons, which conduct the phase-locked spikes from NM to NL, the chemical synapses between NM axons and NL neurons, and the NL neuronal spikes. GABAergic inputs were neglected because they do not appear to phase lock to high-frequency tones (Yang et al., 1999).

NL is a large, dorsoventrally flattened oval nucleus in the dorsal brainstem, below the fourth ventricle (Fig. 4.8). NL is about 700 $\mu$m deep (dorso-ventral), about 2 mm wide (medio-lateral) and about 3.5 mm long (rostro-caudal; Fig. 4.8H, I). All values are corrected for shrinkage, if not stated otherwise. NL has a total volume of about 6.4 mm$^3$ (4.8 mm$^3$ if not corrected for 10% shrinkage) and is surrounded by a glial envelope (Cheng and Carr, 2007), penetrated dorsally by axons from the ipsilateral NM, and ventrally by axons from the contralateral NM (Fig. 4.8A, J). NM axons interdigitate, and traverse the dorso-ventral dimension of NL (Fig. 4.8A and B). These axons are densely packed, with a mean axon diameter of $3.3 \pm 1.5$ $\mu$m ($n = 406$; $3.0 \pm 1.3$ $\mu$m, not corrected for shrinkage; compare with Carr and Boudreau (1993a): $3.18 \pm 0.74$ $\mu$m, not corrected for shrinkage), and the density of the axons is about 72,000 mm$^{-2}$ (Fig. 4.8D). The mean distance between two neighboring nodes of Ranvier is about 60 $\mu$m ((Carr and Konishi, 1990; Carr and Boudreau, 1993a): $58 \pm 5.3$ $\mu$m, not corrected for shrinkage). Further details of the physiology of NL have been introduced in the subsection 2.2.3 Auditory brainstem.

NL neurons are medium sized ovals with maximum diameters of $15 - 20$ $\mu$m (not corrected for shrinkage; (Carr and Konishi, 1990)) and large numbers of short ($5.0 \pm 1.9$ $\mu$m) stubby dendrites (Fig. 4.8D−F; not corrected for shrinkage, (Carr and Boudreau, 1993a)). NL neurons are sparsely distributed; the mean distance between neighboring NL cells is about 100 $\mu$m (Fig. 4.8D, (Carr and Boudreau, 1993a): $75 \pm 8\mu$m not corrected for 10% shrinkage and for the projection of the slice volume to a plane). In total, there are about 13,000 neurons in NL (Winter and Schwartzkopff, 1961; Kubke et al., 2004). If the volume of NL is divided by the total number of neurons, the density of the neurons in the 5 kHz region is about 2,000 mm$^{-3}$. This density also corresponds approximately to the mean distance of 100 $\mu$m. This simple density measure slightly overestimated the cell density in the rostral two thirds of NL because cell density in NL was not even. The highest cell density was found in the caudal, low BF region. Each NL neuron was contacted by about 100 (range 45 to 150) afferent NM axons from each side, and each NL neuron has only one axon (Carr and Boudreau, 1993a). The NL spike is probably generated in the first node of Ranvier of the NL axon (Ashida et al., 2007; Carr and Boudreau, 1993b; Kuba et al., 2006).

Taking into account these characteristics, in what follows we use the computational model to estimate how many sources of each type are needed to reproduce properties of the measured neurophonic. Such estimates will allow us to identify the putative generator(s). Here we divide the generators into two classes: (i) the output of NL, i.e. action potentials of NL neurons, and (ii) the input to NL, i.e. action potentials in NM axons as well as the activity of synapses between NM axons and NL neurons. In both cases, we will investigate how we could reach a cyclic-mean amplitude in the range of 1 mV and a SNR up to 30 dB for acoustic stimulation with tones.

### (i) Contribution of the output of NL to the neurophonic

We first considered how the output of NL, that is the action potentials of NL neurons, contributed to the neurophonic. For monaural acoustic stimulation with tones near BF, as in our recordings, the firing rate of NL neurons was typically about $\lambda_{\text{driven}} = 210 - 240$ Hz, and the vector strength was $v = 0.2 - 0.5$ for $f_{\text{stim}} = 5$ kHz (Carr and Konishi, 1990; their table 2), (Peña et al., 1996). The spontaneous firing rate was set to $\lambda_{\text{spont}} = 50$ Hz (Carr and Konishi, 1990; Viete et al., 1997).

Using these constraints in our model, Eq. (4.13) with SNR = 30 dB, $\lambda = 240$ Hz, $v = 0.5$, and $T = 80$ ms predicts $N = 208$ independent sources, which is a lower bound for the true number of sources. We note that Eq. (4.13) was based on the assumption of identical kernel amplitudes for all neurons.

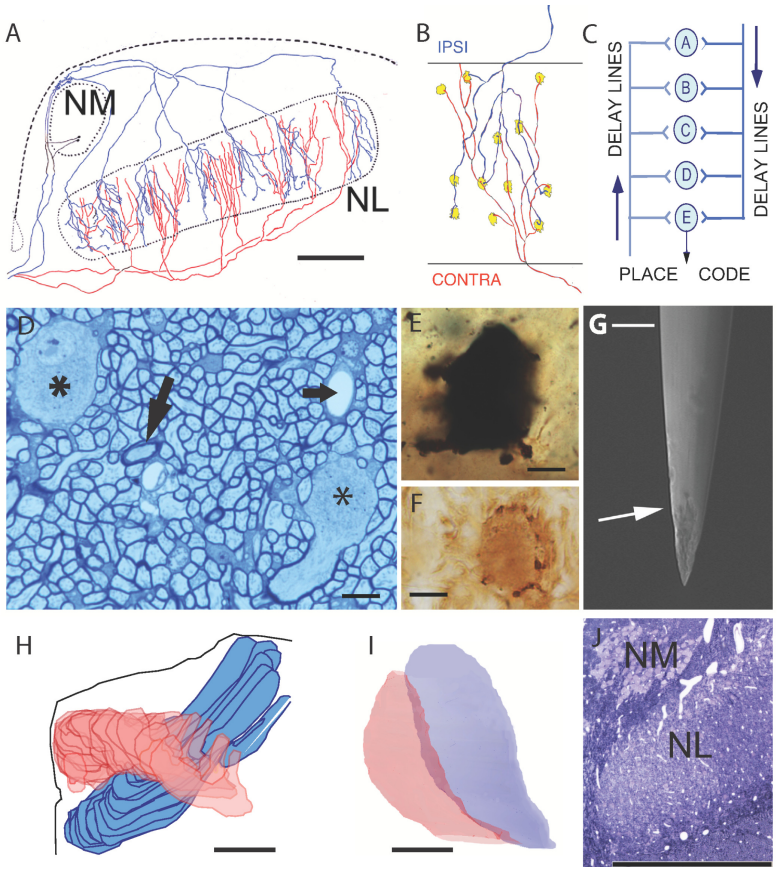


Figure 4.8.: ITD coding circuits and NL elements in the barn owl. *A:* Drawing of a transverse hemisection through dorsal brain stem, adapted from Figure 2 of Carr and Konishi (1990), with the projection from the nucleus magnocellularis (NM) to the nucleus laminaris (NL). Two NM neurons and their axonal arbors in NL were reconstructed. Ipsilateral NM axons in blue, and contralateral axons in red. Because each arbor is 3-dimensional, the actual mediolateral extent of the nucleus laminaris has been exaggerated to accommodate the full superimposed arbors (see reconstructed NL in H for an accurate 3D view). Scale bar, 500 $\mu$m. *B:* Diagram of interdigitating ipsilateral (blue) and contralateral (red) axons traverse the dorsoventral dimension of NL to create a map of ITD. *C:* Jeffress model, with binaural coincidence detectors *D:* Horizontal 2 $\mu$m section through NL, orthogonal to delay line axons, stained with Toluidine Blue. There are two NL neurons (*), surrounded by the myelinated afferent NM axons. Blood vessels (small arrow), sparse NL neuron axons (arrow, thicker myelin than the NM axons) and glial cells are also visible. *E:* Rapid Golgi stained NL neuron with many short dendrites. *F:* Immunohistochemical labeling with an antibody against GABA reveals perisomatic GABAergic terminals in NL. *G:* Scanning electron micrograph of one of the batch of 4 M$\Omega$ tungsten electrodes used in this study. Arrow marks border between insulation and the electrode tip. *D-G* Scale bars are 10 $\mu$m. *H:* 3D reconstruction of NM and NL, looking from caudal to rostral, with medial to the left and lateral to the right. *I:* View of the same reconstruction from above. *J:* Transverse section through Toluidine blue stained 2 $\mu$m section through the medial central region of NL, with NM above. Note the lighter myelin within NL, as compared to the NM cross tract. *H-J:* Scale bar are 1 mm.

Refining the model through a distance-dependent decay of amplitudes according to $1/r^2$, Eq. (4.20) indicates that we need $N = 690$ NL neurons to reach an SNR of 30 dB (above we obtained $N = 633$ for a slightly different set of parameters). Thus, if NL neuronal spikes are the only source of the neurophonic, a significant fraction of the total number of about 13000 neurons in the NL must contribute. The low density 2000 mm$^{-3}$ of NL neurons then implies that the electrode picks up signals from a sphere with a radius of about 440 $\mu$m.

A numerical simulation that illustrates this "NL-output" scenario is presented in Figure 4.9. This simulation resembles the sustained response of the data shown in Figures 4.1, 4.3, and 4.4 as closely as possible. To match the data, we fixed basic parameters ($\lambda_{\text{driven}} = 240$ Hz, $\lambda_{\text{spont}} = 50$ Hz $f_{\text{stim}} = 5$ kHz, $v = 0.5$) and chose $N = 206$ to reach the observed SNR = 26.2 dB (Eq. (4.21)). This number of NL neurons can be found within a radius of 295 $\mu$m around the tip of the electrode. Furthermore, a rather large kernel amplitude of 620 $\mu$V (at a distance 50 $\mu$m) had to be chosen to match the observed cyclic-mean amplitude of 0.32 mV (Eq. (4.16)). Moreover, the large kernel amplitude resulted in a less smooth voltage trace in comparison to the physiological data (Figs. 4.9A and 4.1A).

### (ii) Contribution of the input to NL to the neurophonic

To estimate how the neuronal structures providing the input to the NL may contribute to the neurophonic, we evaluated the activity of the contribution from NM. The phase-locked input to NL originates exclusively from the NM, that is, via NM axons within the NL and via synapses between terminals of NM axons and somata of NL neurons.

Tones presented monaurally at a frequency of 5 kHz activate NM neurons with BFs near 5 kHz, tonic firing rates of about $\lambda_{\text{driven}} = 450$ Hz (Carr and Konishi, 1990; Peña et al., 1996) and a vector strength of about $v = 0.4$ (Köppl, 1997b). To estimate the number $N$ of independent inputs contributing to the neurophonic for the case of monaural stimulation, we considered that half of the $N$ inputs are spontaneously active because they originate from the non-stimulated side. For the non-stimulated fibers we took a spontaneous firing rate of $\lambda_{\text{spont}} = 200$ Hz (Köppl, 1997a) and set the vector strength to zero.

To estimate the expected SNR for the case of identical kernels for all sources, the noise level was due to $N/2$ driven sources and $N/2$ spontaneously active sources. Extending Eq. (4.11), we found that the noise level was proportional to $[(N/2)\lambda_{\text{driven}} + (N/2)\lambda_{\text{spont}}]$. The $N/2$ driven sources gave rise to the signal level, which was proportional to $[(N/2)\lambda_{\text{driven}}\, v]^2 T$; see also Eq. (4.10). The SNR then was

$$\text{SNR} = \frac{N\, \lambda_{\text{driven}}^2\, v^2\, T}{2\, (\lambda_{\text{driven}} + \lambda_{\text{spont}})} \quad . \tag{4.22}$$

To reach an SNR of 30 dB for $\lambda_{\text{driven}} = 450$ Hz, $\lambda_{\text{spont}} = 200$ Hz, $v = 0.4$, and $T = 0.08$ s, we need at least about $N = 500$ independent sources, each of which contributes with the same kernel to the neurophonic.

The number $N = 500$ axons can be found in the vicinity of the tip of an electrode within NL. For a density 72000 mm$^{-2}$ of axons, the required 500 axons fit in a halo with a radius of about 47 $\mu$m. However, different axons might not be statistically independent because an axonal tree originating from a single NM neuron has many branches (Figs. 4.8A and B), and each axonal tree represents only one independent source in our model. The minimum halo for $N = 500$ independent sources was therefore larger. However, even for a tenfold lower local density of independent axons, the electrode halo will increase only by a factor of $\sqrt{10}$ to about 150 $\mu$m.

A numerical simulation that illustrates this "NL-input" scenario is presented in Figure 4.10. This simulation closely resembles the sustained response of the data shown in Figures 4.1, 4.3, and 4.4. To

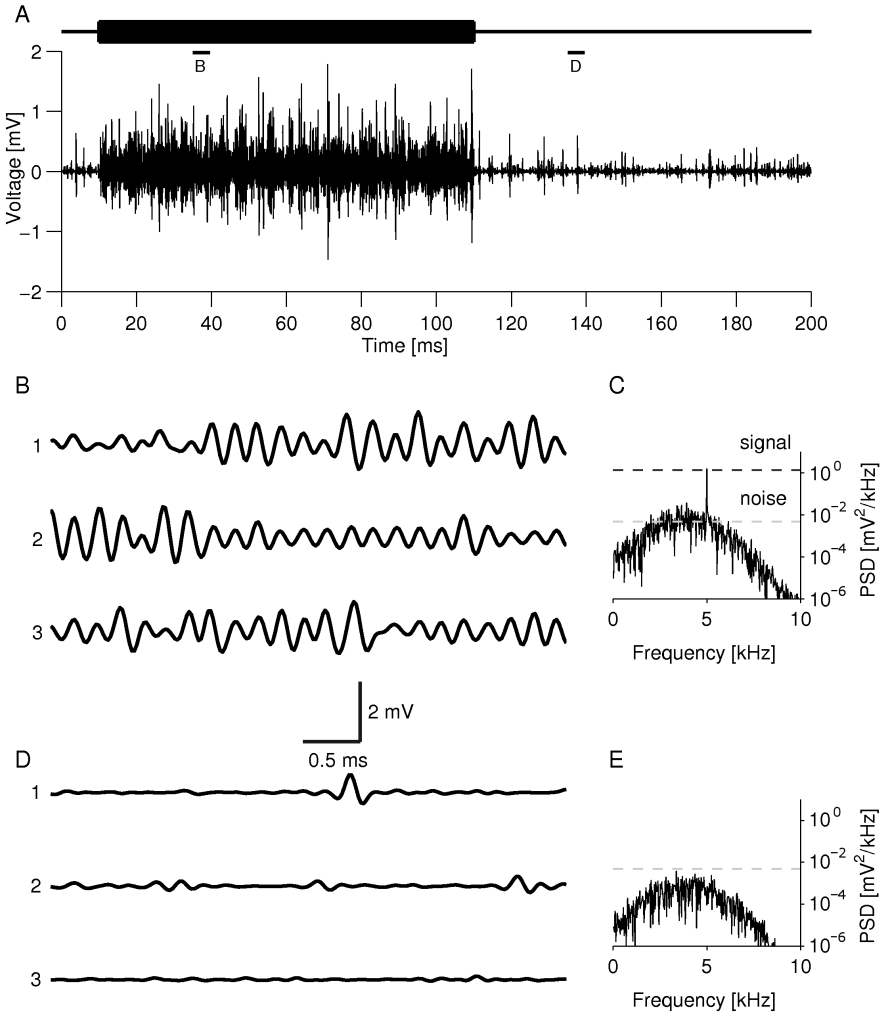


Figure 4.9.: Numerical simulation of the neurophonic – output scenario. All kernels were identical in shape, but their amplitude depended on the distance with $1/r^2$. *A:* Stimulus (top) and response (bottom). The driven response (10–110 ms) and the spontaneous activity (0–10 ms and 110–200 ms) were sums of the activity of $N = 206$ sources. The mean distance between sources was 100 $\mu$m, and they were distributed uniformly. *B:* Five-millisecond intervals of the neurophonic, 25–30 ms after stimulus onset, as labeled in *A*, at an expanded time scale. The three traces were from statistically independent trials. *C:* Mean PSD of the driven response in *B*, based on activity 10–90 ms after the onset of the tone. *D:* Spontaneous activity, 25–30 ms after stimulus offset, as labeled in *A*. *E:* Mean PSD of the spontaneous activity. The dashed line shows the same level as in *C* (noise), for reference. Simulation parameters: $N = 206$ sources, kernel amplitude: 620 $\mu$V. Driven activity: vector strength $v = 0.5$, mean firing rate $\lambda_{\text{driven}} = 240$ Hz, stimulus frequency $f_{\text{stim}} = 5$ kHz. Spontaneous activity: $v = 0$, $\lambda_{\text{spont}} = 50$ Hz. Resulting properties of the driven neurophonic: cyclic-mean amplitude: 0.38 mV, SD: 0.36 mV, signal level (peak): 4.753 mV$^2$/kHz, noise level: $9 \cdot 10^{-3}$ mV$^2$/kHz, SNR: 27.5 dB. Resulting properties of the spontaneous neurophonic: SD: 0.07 mV, noise level around 5 kHz: $1 \cdot 10^{-3}$ mV$^2$/kHz.

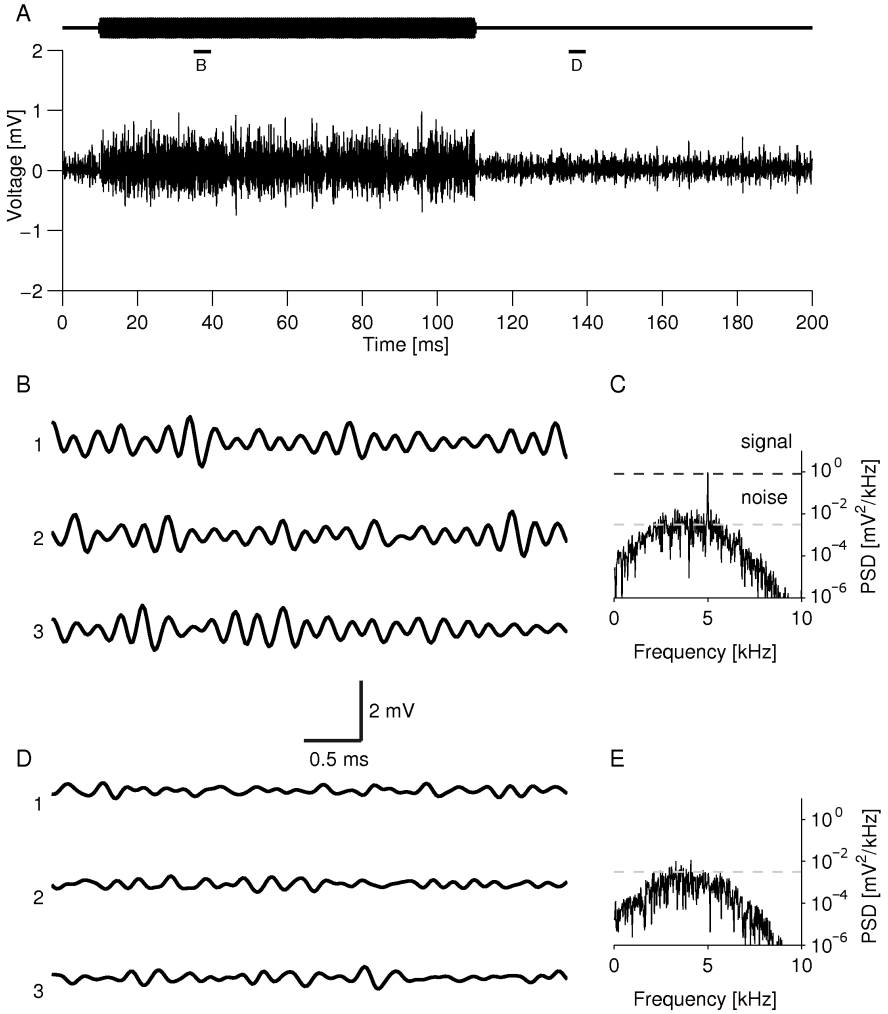


Figure 4.10.: Numerical simulation of the neurophonic – input scenario. All kernels were identical, i.e., each source had the same shape and amplitude. *A:* Stimulus (top) and response (bottom). The driven response (10–110 ms) is a sum of spontaneous activity and monaurally driven activity, each having an equal number of $N/2 = 105$ sources. The spontaneous activity (0–10 ms and 110–200 ms) is from $N = 210$ spontaneously active sources. *B-E:* See the caption of the Figure 4.9. Simulation parameters: $N = 210$, kernel amplitude: 58 $\mu$V. Driven activity: vector strength $v = 0.4$, mean firing rate $\lambda_{\text{driven}} = 450$ Hz, stimulus frequency $f_{\text{stim}} = 5$ kHz. Spontaneous activity: $v = 0$, $\lambda_{\text{spont}} = 200$ Hz. Resulting properties of the driven neurophonic: cyclic-mean amplitude: 0.30 mV, SD: 0.26 mV, signal level (peak): 2.92 mV$^2$/kHz, noise level: $4 \cdot 10^{-3}$ mV$^2$/kHz, SNR: 28.5 dB. Resulting properties of the spontaneous neurophonic: SD: 0.10 mV, noise level around 5 kHz: $2 \cdot 10^{-3}$ mV$^2$/kHz.

match the data, we fixed basic parameters ($\lambda_{\text{driven}} = 450$ Hz, $\lambda_{\text{spont}} = 200$ Hz, $f_{\text{stim}} = 5$ kHz, $v = 0.4$) and chose the total number $N = 210$ of axons to reach the observed SNR =26.2 dB (Eq. (4.22)). Furthermore, the kernel amplitude 58 $\mu$V was used to match the observed cyclic-mean amplitude of 0.32 mV (Eq. (4.8) for $N/2 = 105$ *coherent* sources).

The example simulation in Figure 4.10 is generic in the sense that all model parameters were fixed by experimental constraints — there was no free parameter that needed to be tuned to reproduce the recorded neurophonic. In particular, the SNR and cyclic mean amplitude were reproduced in the numerical simulations by selecting corresponding numbers of sources and kernel amplitudes. Thus, further simulations (not shown) of the input scenario also matched the data very well. The more important results of the model were the values of the parameters such as number of independent sources and the peak amplitude of the kernel. They could be obtained directly from the mathematical analysis of the computational model in the section 4.3, in particular Equations. (4.8) and (4.22) for the input scenario (Fig. 4.11, gray) and Equations. (4.16) and (4.20) for the output scenario (Fig. 4.11, black). Only for this input scenario, were the obtained values of the parameters consistent with the anatomy and physiology of the NL. In summary, our analysis indicates that the contributions of the input to NL can explain the measured properties of the neurophonic.

## 4.5. Discussion

A combined computational and electrophysiological investigation of the neurophonic potential observed in the high-frequency region of the barn owl NL was used to connect the EFPs to their neuronal generators. We shall first compare our results with earlier observations of the neurophonic, then discuss the relative measure of SNR as an indicator for the number of contributing sources, and finally draw conclusions about the nature of sources.

### 4.5.1. Neurophonic in the barn owl and in other animals

Our data are consistent with those of Sullivan and Konishi (1986) in that the time courses of the frequency-following neurophonic potentials in response to monaural tone bursts were typically oscillatory up to 7 kHz, with amplitudes in the millivolt range. Such a response behavior is indicative of the volley principle (Wever and Bray, 1930) because each single neuron cannot produce an action potential at such a high rate.

A strong neurophonic is also present in chicken NL (Schwarz, 1992a; Köppl and Carr, 2008). The observed increases of the PSD in the vicinity of the cell body layer led to the conclusion that the neurophonic potential is created by synaptic currents (Schwarz, 1992a). In contrast, in the barn owl, when the electrode is in NL, there are no local peaks (within a range of 100 $\mu$m) in the amplitude, PSD, or SNR of the neurophonic (Kuokkanen et al., 2009). Instead, the neurophonic increases steadily from the edges of NL to the center. Since the structure of NL and the shape of neurons in NL in chick and owl are different, it is not clear whether chick and owl neurophonic in NL share the same sources. In the chick, NL neurons are asymmetric (bipolar), and they are arranged in a densely packed layer of $1-3$ neurons (Smith and Rubel, 1979). The extracellular neurophonic has an amplitude of about 100 $\mu$V, or about $10-20$ times smaller than in owl, and best frequencies are lower (Schwarz, 1992a; Köppl and Carr, 2008; Carr and Konishi, 1990). According to the model presented here, the extracellular neurophonic in chick may be explained by signals from NM synapses, with additional contributions from NL action potentials.

In cat auditory nerve, the neurophonic may represent a spatial summation of the coherent, phase-locked activity (Snyder and Schreiner, 1984). In cat medial superior olive, with a structure similar to the chick NL in that both have a monolayer-like array coincidence detector neurons, the neurophonic is strongest close to this cell layer (Guinan et al., 1972; Bojanowski et al., 1989; Wernick and Starr,

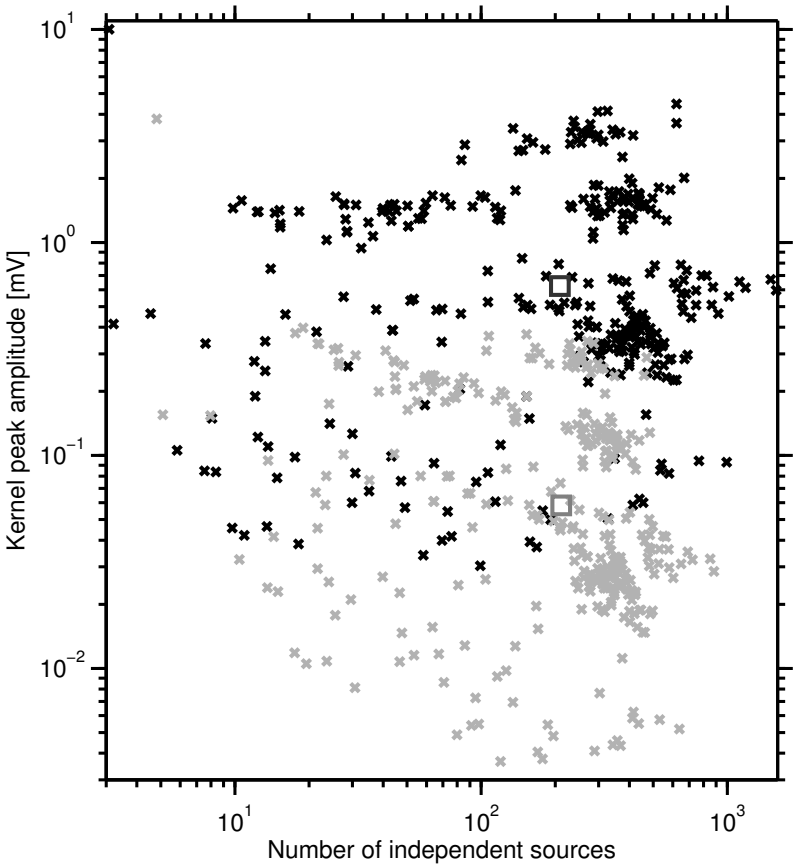


Figure 4.11.: Estimated numbers of independent sources and kernel peak amplitudes for all 331 recording sites. Both the input scenario (gray) and output scenario (black) were considered, and values were calculated with Eqs. (4.8) and (4.22) (input) and Eqs. (4.16) and (4.20) (output). In the equations, the parameters' dependency on the stimulus frequency was taken into account for the kernel as well as for the vector strength of the driven activity; for the input scenario the vector strength was fitted linearly by $v = 0.61 - 5.2 \cdot 10^{-5} \cdot f_{\mathrm{stim}}$ (Köppl, 1997b) and for the output scenario by $v = 0.77 - 6.7 \cdot 10^{-5} \cdot f_{\mathrm{stim}}$ (Carr and Konishi, 1990), in both $1500 \leq f_{\mathrm{stim}} \leq 6000$ Hz. Otherwise, the parameters were the same as in Figs. 4.9 and 4.10 (in which vector strengths were slightly higher than in the linear fit). For the input scenario, the number of independent sources was the sum of spontaneous and driven sources. The examples from Figs. 4.9 and 4.10 are marked with squares.

1968). There, the neurophonic has been proposed to be generated by a dipole field originating from the bipolar neurons with oriented dendrites which generate a phase shift of about 0.5 cycles between the sink and the source of the dipole (Mc Laughlin et al., 2010a). To our understanding, the high-frequency neurophonic in the barn owl is not produced by such a dipole field because the phase shift observed when moving the electrode through NL is generally much greater than 0.5 cycles (Sullivan and Konishi, 1986).

### 4.5.2. Derivation of SNR and SNR in other neuronal systems

The SNR, in general, can be used to quantify how much information the response carries about the stimulus (Borst and Theunissen, 1999). Here we used the SNR to quantify the measured neurophonic and to compare it to the computational model. For tones, the SNR is a relative measure in a narrow frequency band. To derive the SNR, the phase locking allowed us to average the responses to tone bursts not only across trials (for review, see Borst and Theunissen (1999)) but also across the many cycles, typically hundreds. The resulting SNRs in the owl's NL reached extraordinary high values of up to 32.2 dB (range from 10.9 to 32.2 dB, median 26.6 dB); the lowest values were probably from locations near the border of NL. Maximum values around 32 dB for extracellular signals were much larger than the estimates for intracellular signals (Ashida et al., 2007): We calculated 27.6 dB (Eq. (4.12) for monaural input: $N = 100$, $\lambda = 450$ Hz, $v = 0.4$, $T = 0.08$ s), which is near our median SNR.

For comparison, SNRs have also been measured in other neural systems. For example, in the saccular nerve of a teleost fish, the SNR reached 30 dB for an 85 ms time window (Tomchik and Lu, 2006). For crayfish photoreceptors, SNRs of up to 22 dB for 120 s recording time were reported (Bahar et al., 2002). The SNRs obtained for periodically driven responses are much higher than SNRs obtained from intrinsically oscillating systems (Hurtado et al., 2004), although the two cases are difficult to compare because for the latter case energy is distributed across a wider frequency band.

### 4.5.3. Modeling results and implications for the origin of the neurophonic potential

We set up a novel model of the neurophonic potential in the auditory brainstem to reveal its sources. Other, similar approaches have modeled intracellular voltages (e.g. Gerstner et al. (1996); Kempter et al. (1996; 1998b;a); Kuhlmann et al. (2002); Ashida et al. (2007)). The assumptions underlying our model were straightforward: an inhomogeneous Poisson process with a periodically modulated rate, and the kernel that matched typical waveforms as recorded in other neuronal systems. In general, the amplitude of a spike depends on the distance $r$ of the source to the tip of the electrode. We considered two special cases. First, a distance-dependent decay where the amplitude was proportional to $1/r^2$ (Rall, 1962; Logothetis et al., 2007), which is reasonable for neuronal dipoles whose spatial extent is smaller than $r$. This "far field" case was used to simulate the contribution to the neurophonic due to spikes of NL neurons, which have a maximal diameter of $15 - 20$ $\mu$m. For distances $r$ smaller than the size of the neuronal source, the decay may be weaker (Nunez and Srinivasan, 2006). In a second case, we assumed that kernel amplitudes were constant. This "near field" case was used to simulate the neurophonic due to NM axonal arbors, which are elongated structures with a length in the range of 1 mm within NL.

An important parameter was the peak amplitude of a spike, which was not available for NL of owls because single units could not be isolated from the EFP with conventional metal electrodes. Spontaneous activity in slices of very young owl NL (Lautemann et al., 2008) indicated peak amplitudes of about 100 $\mu$V. A kernel amplitude 100 $\mu$V may also be an upper bound for amplitudes of extracellular spikes of NL neurons when measured at a reference distance of 50 $\mu$m, which is half the distance between nearest neighbors (Carr and Boudreau, 1993a). The value 100 $\mu$V is typical for the much larger hippocampal pyramidal neurons, which exhibit action potentials with intracellular spike amplitude in the range of 100 mV (Gold et al., 2006). In contrast, the intracellular spike amplitude of adult NL neurons has been suggested to be only about 10 mV (Funabiki and Konishi, 2005; Ashida et al., 2007), see also (Kuba et al., 2005; Golding et al., 1995; Oertel et al., 2000; Scott et al., 2005). Spike amplitudes may also be estimated as follows: at the peak of a spike, membrane currents are in the range of 2 nA (Ashida et al., 2007), see also (Scott et al., 2010), which corresponds to an input resistance of 5 M$\Omega$ for spike amplitudes of 10 mV (K Funabiki, personal communication). For a spike generated in the first node of Ranvier of the NL afferent axon, about 60 $\mu$m away from the soma (Carr and Boudreau, 1993b), and for a specific resistance of about 2 $\Omega$m of NL tissue, we can estimate the spike amplitude resulting from

such a dipole (Logothetis et al., 2007; p. 815) to be at most 2 nA $\cdot$ 60 $\mu$m $\cdot$ 2 $\Omega$ m/($2\pi \cdot r^2$) = 19 $\mu$V at a distance $r = 50$ $\mu$m from the center of the dipole. In summary, the estimated extracellular kernel amplitude of 19 $\mu$V for NL spikes is well below 620 $\mu$V, which is the amplitude required to explain the measured cyclic-mean amplitude of the neurophonic with NL spikes only.

### Identical kernel amplitudes

In the above approaches, with identical kernel amplitudes and with distance-dependent, dipole-like decay of kernel amplitudes, the mathematical analysis (results in Eqs. (4.13), (4.20) and (4.22)) proved that the SNR of the modeled neurophonic was independent of the form and the amplitude of the extracellular action potentials (i.e. the kernels). The only unknown parameter that remained was N, the number of independent sources that contribute to a given SNR.

The model with identical kernels for all sources sets a lower bound for the number $N$ of sources to reach a certain SNR. Any kind of variability, for example in the amplitudes or shapes of the kernels, only increases the $N$ needed to create a certain SNR. Moreover, weakening the assumption of independent sources increases the necessary number of sources. Including in the model further noise sources (for example an invariant background noise, GABAergic synapses, etc.) also increases $N$. We found at least hundreds of independent neuronal sources are needed to reach an SNR of 30 dB. Equations (4.13) and (4.22) tell us how $N$ depends on the experimentally accessible quantities.

**Spatial extent of one source** A natural upper bound for the number of independent sources in NL may be the number of NM neurons because each axonal tree of an NM neuron represents one independent source in NL. The required number of independent axonal branches (to generate the measured properties of the neurophonic) can already be found within a small radius of about 150$\mu$m around the electrode. The attenuation of kernels may be neglected for $r$ that are smaller than the spatial extent of an action potential propagating along an NM axon. Its spatial width in NL is about one millimeter for a conduction velocity of 5 m/s and for an assumed temporal width as low as 0.2 ms (Carr and Konishi, 1990; their Fig. 5). Therefore, within the estimated electrode halo, the distance dependence of the kernel amplitude is weak, and may be weaker than $1/r$ (Nunez and Srinivasan, 2006). However, amplitudes of axonal action potentials are quadrupolar at large distances, i.e. they show a $1/r^3$ dependence of the amplitude for large $r$ (Nunez and Srinivasan, 2006).

It is clear that such a strong decay at large $r$ is necessary to avoid arbitrary large SNRs and cyclic mean amplitudes in models of the neurophonic. We indeed included a strong decay in our model of the input scenario (with identical kernel amplitudes) simply by restricting contributions of sources to a finite halo around the electrode: inside the halo the amplitudes were constant, outside they were zero. A halo in the range 150$\mu$m also guarantees that for each axon there are at least two nodes of Ranvier, which are the source of axonal currents. Finally, cyclic-mean amplitudes in the millivolt range, kernel amplitudes in the range of 100 $\mu$V were sufficient (Fig. 4.11). Numerical simulations based on such identical kernels matched the data well (Fig. 4.10).

**Numbers of possible sources contributing to the neurophonic** Each of the approximately 13,000 NL neurons is contacted by about 100 afferent NM axons from each side (Carr and Boudreau, 1993a). The contributions of the 2,600,000 synapses within NL can simply be included in the kernel that describes the waveform due to a spike of an NM neuron because the synapses' activity is highly correlated to the activity of the axons feeding them. Thus, including synapses does not change the above arguments.

Although currents originating from synapses between NM axons and NL neurons might be larger than currents from nodes of Ranvier of NM axons, it is unclear how strong synaptic currents affect the extracellular field. Synaptic currents actually may contribute little to the extracellular field because neurons in the high-frequency region of NL are nearly spherical and synapses are distributed uniformly

on the neuron's surface (Carr and Boudreau, 1993a). This "closed field" configuration (Lorente de Nó, 1947) predicts that synaptic currents in NL neurons have a relatively small impact on the extracellular field, in contrast to the elongated NM axons. The "closed field" configuration is broken only by the outgoing NL axon, which is notably large and oriented orthogonal to the NM axons Carr and Boudreau (1993b).

We propose that contributions from the input to NL, i.e. axons from NM and synapses between NM axons and NL somata, yield the necessary number of inputs to explain both the high SNR and large amplitude of the neurophonic. In this case, contributions to the neurophonic originate within about 150 $\mu$m of the recording electrode, which is in line with results by Katzner et al. (2009) who showed that 95% of the local field potential in visual cortex originate within 250 $\mu$m of the recording electrode. Furthermore, Nelson and Pouget (2010) argue that the electrode impedance and geometry do not appreciably affect recordings of the field potential. That the neurophonic reflects the input was already suggested from models for the development of temporal-feature maps in NL (Kempter et al., 2001; Leibold et al., 2001a; 2002).

### Distance-dependent decay of kernel amplitudes

In addition to the above case of identical kernels for all sources, we considered a dipole-like decay of amplitudes, where sources were spatially uniformly distributed within a spherical halo of radius $R$ around the electrode tip. Although the kernel amplitudes decreased with distance, the PSD of the signal increased with the radius $R$ of the halo because the number of sources in a thin spherical shell of radius $r$ is proportional to $r^2$, which compensates the $1/r^2$ dependence of the kernel amplitude. The PSD "signal" level is thus determined by the size of a region in which neurons are synchronously active. On the other hand, the PSD of the noise saturates with increasing $R$. The noise is therefore "local", in contrast to the "global" signal. In effect, the SNR in Eqs. (4.19) and (4.20) also increases with increasing $R$ and $N$, respectively.

The $1/r^2$ dependence of kernel amplitudes gave rise to two predictions. First, for a measured SNR of 30 dB, at least $N = 690$ NL neurons are required, which can be found within a sphere of radius $N^{1/3} \cdot r_S = 400$ $\mu$m (the minimum halo of an electrode). Second, extracellular spike amplitudes should be in the same range as the cyclic-mean amplitude, i.e. in the millivolt range. Such large extracellular spike amplitudes are difficult to reconcile with the properties of NL neurons and difficulties in isolation of single units in NL.

The hypothesis that NL neurons within a sphere of radius 400 $\mu$m contribute to a tone-driven neurophonic is not in line with the tuning and the synchrony of the activity of NL neurons. The width of the short axis of NL parallel to the axonal delay lines is approximately 700 $\mu$m (Carr and Konishi, 1988). Spikes of neurons along this dorso-ventral axis are coherent but not necessarily synchronous, because the preferred phase of firing depends on the neuron's position, which reflects their tuning to the interaural time difference (Carr and Konishi, 1990). For example, for an axonal conduction velocity of 5 m/s and a stimulus frequency of 5 kHz, neurons that are 500 $\mu$m apart from each other (along this axis) fire 180 degrees out of phase (Sullivan and Konishi, 1986). Their summed contribution to the neurophonic would decrease the cyclic-mean amplitude and the SNR because of negative interference. Positive interference is possible only within a distance of about 250 $\mu$m from the tip of an electrode. Inside a sphere with radius 250 $\mu$m there are, however, only about $(250/50)^3 = 125$ NL neurons. Such a small number of NL neurons cannot explain an SNR of 30 dB.

What is the range of synchrony in the two remaining dimensions of NL? The tonotopic axis in NL runs from mediocaudal to rostrolateral (owl, (Carr and Konishi, 1990); chicken, (Rubel and Parks, 1975; Köppl and Carr, 2008)). We assume that a frequency lamina in the 5 kHz region would extend only about 600 $\mu$m in the caudomedial to rostrolateral dimension, given the width at half height of tuning curves of about 1.2 kHz (Peña et al., 2001), and the frequency gradient in this region of about 0.5 mm/kHz (Carr and Konishi, 1990; their Fig. 3A). Tuning curves and SNR tuning curves (for example

in Figs. 4.2C and 4.4E) had a similar width, which confirms the estimated spatial range of synchrony. In our estimate of the range of synchrony, we neglected any change or variability in phase of firing along the tonotopic axis, which can only further decrease the range of synchrony. In summary, the 600 $\mu$m upper bound for the range of synchrony is smaller than the diameter 880 $\mu$m diameter of the sphere in which NL neurons should contribute to a tone-driven neurophonic. The third dimension of NL should not constrain the neurophonic in a similar way because neurons within an isofrequency band might fire synchronously (Sullivan and Konishi, 1986).

## Conclusions

We conclude that it is difficult to explain both the high SNR and the large cyclic-mean amplitude of the tone-driven neurophonic with the contributions from NL action potentials only. NL axons also should not contribute significantly because their number is approximately a factor 100 less than the NM axons. The initial segment of the NL axon is, however, very large (up to 10 $\mu$m in diameter when it leaves the cell body), and may make a significant contribution, although it should be noted that it is strongly myelinated with its first node at 60 $\mu$m distance from the soma, and that it is orthogonal to the NM axons (Carr and Boudreau, 1993b).

In summary, the high cyclic-mean amplitude and the large SNR of the neurophonic in response to high-frequency tones provide strong constraints for the origin of the neurophonic potential in barn owl NL. We can exclude large contributions of spikes of NL neurons. Our analyses and simulations show that a large number of sources, i.e. hundreds, are needed to form the neurophonic potential as observed in barn owl NL. Many arguments support the input from NM as the origin, although the contributions from NM axons and their synapses can not be separated. Further experimental and theoretical work is required to resolve this issue.

# 5. Waveform Summation in the Barn Owl's Brainstem

## 5.1. Summary

The neurophonic potential is a frequency-following extracellular potential that can be recorded, for example, in the nucleus laminaris (NL) in the brainstem of the barn owl. Putative generators of the neurophonic are the activity of afferent axons from nucleus magnocellularis, synaptic activation onto NL neurons, and spikes of NL neurons. We hypothesize that the input to NL, i.e., affarent axons and synapses, are the origin of the neurophonic. This model implies that the sum of the responses to ipsi- and contralateral stimulation matches the response to binaural stimulation. It fully explains the tuning of the neurophonic to the interaural time difference. In particular, it was not necessary to include nonlinear responses of NL coincidence detector neurons, whose firing rate and synchrony strongly depend on the interaural time difference. Our results suggest that the input to NL is the main origin of the neurophonic[1].

## 5.2. Introduction

Barn owls localize auditory sources with excellent precision (1.5° error in the direction of the head) (Knudsen et al., 1979; Bala et al., 2003). The localization of the azimuth is based on the encoding of the interaural time differences (ITDs) in the nucleus laminaris (NL) by coincidence detection neurons (Moiseff and Konishi, 1981; Poganiatz et al., 2001; Bala et al., 2003). The encoding is based on the phase-locked monaural inputs from the ipsi- and contralateral nucleus magnocellularis (NM) via axons acting as delay lines (Jeffress, 1948; Carr and Konishi, 1990).

ITD sensitive neurons have been recorded, apart from NL of the owl, also in chicken (Overholt et al., 1992), as well as in the medial superior olivary nucleus (MSO) of several mammals (cats: Galambos et al. (1959); Moushegian et al. (1964); Guinan et al. (1972); Yin and Chan (1990), dogs: Goldberg and Brown (1969), kangaroo rats: Moushegian et al. (1975), brown bats: Grothe and Park (1998), gerbils: Spitzer and Semple (1995); Brand et al. (2002) and rabbits: Batra et al. (1997)) and in the inferior colliculus of both avians and mammals (Knudsen and Konishi, 1978a; Carney and Yin, 1989; Yin et al., 1990; Wagner, 1992; Euston and Takahashi, 2002; Joris et al., 2005; Agapiou and McAlpine, 2008; Vonderschen and Wagner, 2009; Horvath and Lesica, 2011). The extracellular field potential or 'neurophonic' (Weinberger et al., 1970) in the NL of both chicks and owls also shows ITD tuning (Sullivan and Konishi, 1986; Schwarz, 1992a; Wagner et al., 2005; Köppl and Carr, 2008).

NL neurons in the owl are difficult to record from intracellularly (Funabiki et al., 2011; Peña et al., 1996; Carr and Konishi, 1990), and their spikes are small (about 10 mV). Thus isolation of single units' activity from the extracellularly recorded neurophonic is impossible. To characterize the response properties of NL, either the bundle of NL output axons (Moiseff and Konishi, 1983; Carr and Konishi, 1990) or the neurophonic in NL has been used (Sullivan and Konishi, 1986; Wagner et al., 1987; 2005;

[1] The research presented in this chapter is the result of a collaboration with several researchers. I conceived the project, developed the analysis tools and performed the analyses of the experimental data. The experimental data was recorded by Catherine Carr and Hermann Wagner in their laboratories in University of Maryland, US and in RWTH Aachen, Germany.

2009). The neurophonic has a temporal precision of $\leq 10$ $\mu$s (Wagner et al., 2005; 2009) in the NL region responsive to high-frequencies ($> 2.5$ kHz) and shows a prominent oscillation at the stimulus frequency (signal-to-noise ratio $> 30$ dB) in response to pure-tone stimulation (Sullivan and Konishi, 1986; Kuokkanen et al., 2010).

The morphology of the owl NL is simple, and thus it is a good model system to test how (and whether it is possible at all) to separate and identify putative neuronal contributors of an extracellular field potential. There are three putative sources of the neurophonic, exhibiting the coherent signals phase-locked to the stimulus frequency. Those are: 1) densely packed axons projecting from the ipsi- and contralateral NMs, 2) the synapses from these axons to the dendrites of NL neurons and 3) oval NL neurons sparsely distributed in NL (only one type of neuron present). NL neurons have a small (non-bipolar) dendritic tree and a thick axon that does not branch within the nucleus (Carr and Konishi, 1990). The neurophonic in NL of the owl has been hypothesized to reflect the activity of a large number (hundreds) of sources related to the input to NL (activity in axons and synapses) (Kuokkanen et al., 2010), whereas the neurophonic in the chicks' NL and in the mammals' MSO has been estimated to originate from fewer, post-synaptic sources (synaptic currents or bipolar neurons' spikes) (Guinan et al., 1972; Schwarz, 1992a; Köppl and Carr, 2008; Mc Laughlin et al., 2010a;b).

We propose that the neurophonic in the owl's NL is a population effect resulting from the activity of many sources that are related to the input to NL, and these inputs originate from the ipsilateral and contralateral sides. This hypothesis has an interesting implication: a linear combination of monaurally stimulated responses can predict binaurally stimulated responses. Several different features characterizing the response can be predicted. Such features are, for example, the amplitude of the phase-locked oscillatory *signal* part of the response and the variance of the non-phase-locked *noise* part (Kuokkanen et al., 2010). The latter, even though not phase-locked, still reflects the overall level of activity. Deviations from the prediction might then relate to some non-linearities in the system, such as contributions from the output of NL, i.e., the activity of the NL neurons.

To test this hypothesis, we analyzed neurophonic responses to monaural and binaural tonal stimulation, and evaluated the quality of the linear prediction from the 'input' model.

## 5.3. Materials and Methods

### 5.3.1. Experimental paradigm

Owl data were recorded as explained in the Appendix B (Neurophonic Recordings). Data set 2 was analyzed for the results following.

### 5.3.2. Extracellular recordings: Data analysis

For each tone burst, the voltage trace from 10-90 ms after the stimulus onset was analyzed. All the data analysis was done with Matlab 7.6 (MathWorks, Natick, MA). To calculate the circular-linear correlation coefficient, the vector strength and the direction of the circular data, we used the Circular Statistics Toolbox by Dr. P. Berens available at matlabcentral (Berens, 2009).

#### Preprocessing and selection of the data

**Amplitudes of spontaneous activity.** Monaural and binaural responses were corrected for instabilities of the response amplitudes during the recording at one location. The minimum duration of a recording at one location was 2 minutes. Locations for which more than 40 minutes passed between the first and the last stimulus condition were excluded from the data set. After that, the average duration of a recording at one location was $7 \pm 5$ minutes (mean $\pm$ SD), only one location exceeding 15 minutes.

To correct for instabilities during recordings at one location, and to correct for manual changes in the amplification gain (powers of 10), for each stimulus condition (ipsilateral, contralateral and binaural stimulation) the spontaneous noise level ('baseline') was calculated as the variance of the first and last 5 ms of each 200-ms recording ([0, 5] ms and [195, 200] ms). The average over all repetitions and stimuli for a given stimulus condition then served as a baseline noise level. The responses to binaural stimulation were then scaled with the factor $\langle$ mean of monaural baselines$\rangle$ /$\langle$ binaural baseline$\rangle$. The scaling factors were in order of $0.09 - 0.11$, $0.9 - 1.1$ and $9 - 11$. Recording locations with a scaling factors larger than 20 were excluded from the data set. Recordings for which the ratio of the ipsi- and contralateral baselines exceeded 1.1 or was below 0.91 were excluded from the data set.

**Phase variability.** In some recordings we observed a variability in the mean phase of the neurophonic, which could also be interpreted as a change of the instantaneous frequency. This variability might be due to synchronization errors in the microsecond scale between the set-up and the recording PC, but also due to natural variability in the responses. The phase changes between trials would result in a decreased cyclic mean signal amplitude and, subsequently, an increased noise variance (see Results) - in the worst case scenario the phases of trials are uniformly distributed and the cyclic mean signal would be zero. However, the phase difference of the mean phase in different repetitions was typically in the range of 5 $\mu$s. Data at one recording location for a given stimulation were therefore corrected for phase changes between trials. The mean phases of the responses (80-ms segments) were therefore aligned by shifting time courses typically by few microseconds.

**Stimulus frequencies.** The set of stimulus frequencies for the monaural responses was always the same for both ears. If a frequency used for the binaural stimulation was not in the set used for stimulating monaurally, the response characteristics (variances of the response, signal and noise) of the monaural responses were interpolated linearly from the closest stimulus frequencies.

The stimulus frequency used for binaural stimulus was about at the best frequency for both monaural responses. The recordings were from the high best frequency (BF) -region of NL; BFs ranged from 2.7 kHz to 7.5 kHz and from 2.9 kHz to 7.4 kHz for ipsi- and contralateral stimulation, respectively. The binaural stimulus frequencies ranged from 3.0 kHz to 7.4 kHz. Both the BF of the contralateral side and frequency of the binaural stimulation were highly correlated with the BF of the ipsilateral side (correlation coefficients $> 0.97, p < 10^{-35}$ for both). The difference between ipsi- and contralateral BFs was small (mean $\pm$ SD: $0 \pm 200$ Hz, range: $-320$ Hz to 480 Hz) and in the same range as previous measurents (Peña et al., 2001).

**ITD tuning.** The tuning to interaural time difference (ITD) is defined as a significant variantion in a response with the stimulus ITD. Only recordings showing an ITD tuning were included in the analysis. The vector strength of the ITD tuning of the response variance was required to be $> 0.02$ and significant. The significance of the vector strength was tested by bootstrapping the variance of each data set 10000 times to calculate the distribution of possible vector strengths for that data set. Other recordings were excluded from the data set (see below).

The best ITD of a recording location was determined by the mean direction of the variance of the mean cyclic signal. The periodicity of the ITD tuning was unequivocally determined by the stimulus frequency. To quantify how well the change of the response with the ITD tuning reflected a sine wave, we used the circular-linear correlation coefficient (Zar, 1999; Berens, 2009):

$$\rho_{cl}(\alpha, x) = \sqrt{\frac{r_{cx}^2 + r_{sx}^2 - 2 r_{cx} r_{sx} r_{cs}}{1 - r_{cx}^2}} \,,$$

where $r_{cx} = c(\cos\alpha, x)$, $r_{sx} = c(\sin\alpha, x)$, $r_{cs} = c(\sin\alpha, \cos\alpha)$ and $c(x, y)$ is the Pearson correlation coefficient.

**Response variance.** The temporal variance of a response is defined as

$$\mathrm{V}ar(V) = \langle (V(t) - \langle V \rangle)^2 \rangle$$

where the mean is marked by the brackets:

$$\langle V \rangle = \frac{1}{T} \int_0^T V(t) \mathrm{d}t \ .$$

The responses we analyzed were mean-free.

**Recording locations.** Above criteria for selecting data sets left us with 58 (out of 91) recording locations that were analyzed in more detail. For the prediction of the binaural phase we only included recording locations at which the same stimulus frequency was used for both monaural recordings as well as for the binaural recordings (38 out of 58); we furthermore excluded those recording locations (4 out of 38) at which either one of the monaural recordings or the binaural recording had a randomized onset phase of the stimulus, leaving 34 recording locations for this prediction.

## 5.4. Results

To clarify the origin of the neurophonic potential in the barn owl's nucleus laminaris (NL), we compared extracellular field potentials in response to monaural and binaural tone bursts, the latter at varying ITDs (Fig. 5.1A–D). Altogether, we analyzed responses at 58 recording locations in the high-frequency region of the NL that showed ITD tuning in their response variance. The stimulus frequency used for each recording location was near its best frequency (see Materials and Methods for details).

### 5.4.1. Quantification of ITD tuning of the neurophonic

The neurophonic in NL typically shows a strong ITD tuning (Sullivan and Konishi, 1986; Wagner et al., 2005; 2009). We quantified ITD tuning using the variance of the ongoing neurophonic response; onset effects were excluded, and we averaged the variance over several trials. Figure 5.1E depicts an example of the response variances to binaural stimulation at different ITDs. The variance of the binaural response showed a modulation with the ITD (vector strength $r = 0.28$, $p = 8 \cdot 10^{-3}$), this modulation was highly sinusoidal (circular-linear correlation $\rho_{cl} > 0.999$, $p = 4 \cdot 10^{-3}$), and the binaural response variances were always larger than the variances of responses resulting from monaural stimulation (see also Fig. 5.4E). This behavior was typical for all 58 recording locations (Fig. 5.1F; $r = 0.15 \pm 0.12$ mean $\pm$ SD, $c = 0.96 \pm 0.07$, all values were significant at $p < 0.05$).

### 5.4.2. Linear-summation hypothesis

What could be the underlying mechanism of the strong ITD tuning of the neurophonic? One the one hand, this ITD tuning could reflect the activity of the primary neurons with the NL. These neurons are generally regarded as nonlinear coincidence detectors that fire at high rates at a particular ITD of the ipsi- and contralateral input. One the other hand, the ITD tuning of the neurophonic could be a result of a linear waveform summation of the ipsi- and the contralateral inputs. Here we test this latter hypothesis and propose that the measured field potential $r_B(t)$ (in response to binaural input) is simply the sum of a contribution $r_I(t)$ from the ipsilateral side and a contribution $r_C(t)$ from the contralateral side, that is,

$$r_B(t) = r_I(t) + r_C(t) \ . \tag{5.1}$$

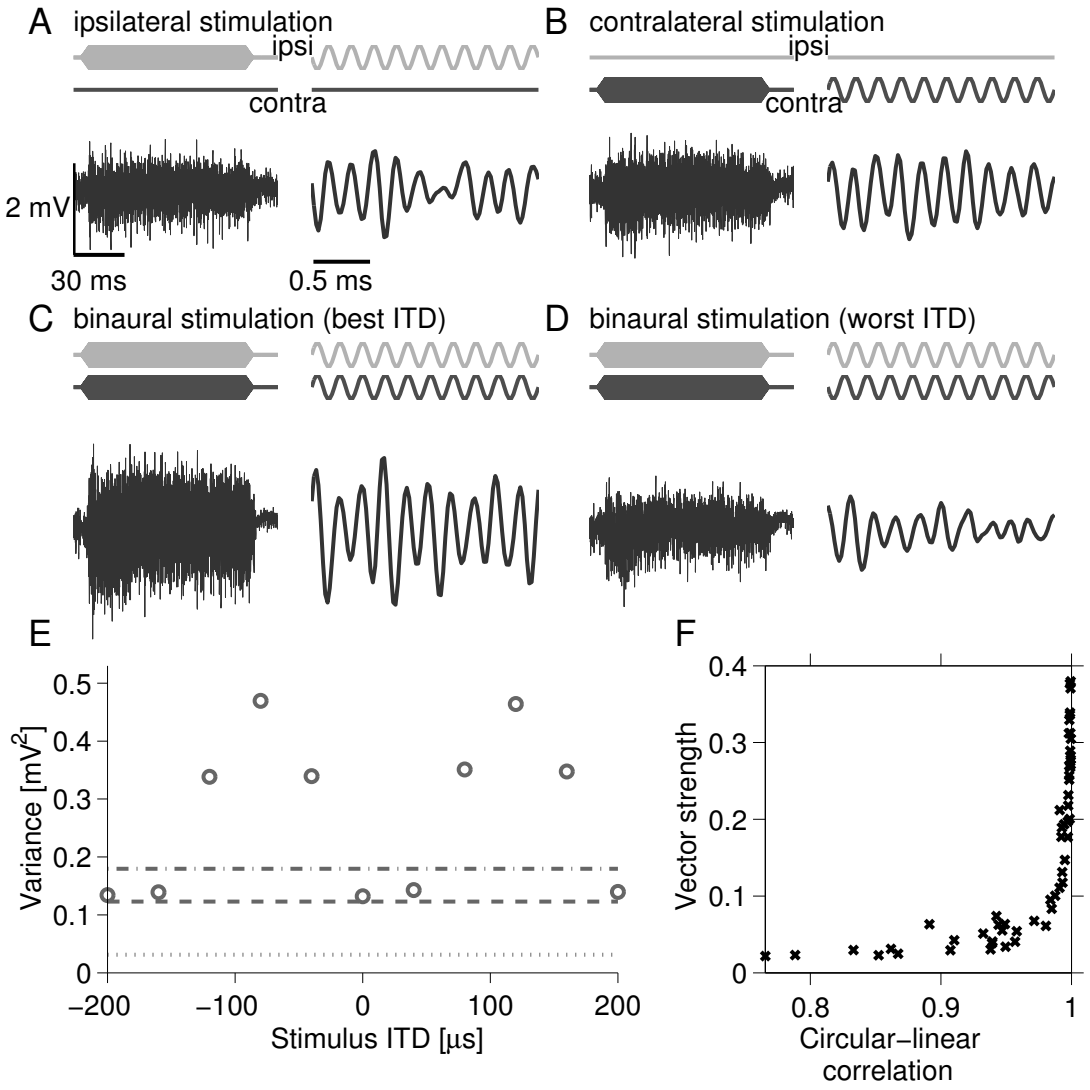


Figure 5.1.: ITD tuning of the neurophonic potential. *A:* ipsilateral stimulation, *B:* contralateral stimulation, *C:* binaural stimulation at best ITD *D:* binaural stimulation at worst ITD. The top panels of *A*–*D* indicate the stimulation paradigm (ipsilateral stimulation: light gray, contralateral stimulation: dark gray). The bottom panels show the neurophonic responses. The left panels show the total length of the response, whereas the right panels show a close-up of the response $30 - 32$ ms after the beginning of the recording. *E:* Response variance (circles) as a function of interaural time difference (ITD) of binaural tones. The horizontal dashed and dash-dotted lines indicate the variances in response to monaural stimulation at the ipsi- and contralateral sides, respectively. The dotted line indicates the variance of the spontaneous activity. Recording location: 502.18.3-4-8, stimulation at 40 dB, stimulus frequency: 5000 Hz. *F:* The strength of the ITD tuning at 58 recording locations: the vector strength is related to the circular-linear correlation.

A direct test of this hypothesis is, however, impossible because monaural and binaural responses cannot be measured simultaneously and a test using responses in subsequent trials is difficult because of considerable trial-to-trial variability. We therefore evaluated the predictions of the linear-summation hypothesis for averaged quantities of the response. In particular, we studied the time course of the phase-locked component (cyclic mean signal) of the response to monaural and binaural tone bursts. Furthermore, we studied the variance of the residual noise of the responses, i.e., the part of the responses that is not phase locked to the periodic stimulus (Kuokkanen et al., 2010).

The cyclic mean signal, in general, is defined as follows (Kuokkanen et al., 2010): If acoustic stimuli are periodic, we may average a neurophonic response $r(t)$ across stimulus cycles. The resulting cyclic mean is then repeated periodically for the duration of the response to produce the "signal" $\langle r(t)\rangle$. The angular brackets $\langle \ldots \rangle$ denote this average. Subtracting the signal from the response we obtain the "noise" (see also chapter 4)

$$n(t) = r(t) - \langle r(t)\rangle \ . \tag{5.2}$$

Signal and noise can be extracted from monaural responses $r_I$ and $r_C$ as well as from binaural responses $r_B$.

An example for a binaural response and the resulting signal and noise are shown in Figure 5.2A–C. The corresponding power spectral densities (PSDs) in Figure 5.2D further illustrate this separation. In summary, the cyclic mean signal captures the phase-locked part of the response, whereas the noise includes all (other) broadband components.

To test our linear-summation hypothesis, let us first focus on basic properties of the cyclic mean signal.

### 5.4.3. Properties of the cyclic-mean signal

Important properties of the binaural signal $\langle r_B(t)\rangle$ (note the subscript 'B' for binaural) are its shape and its ITD-tuning. To describe the ITD tuning, we considered the variance $\mathrm{V}ar\langle r_B(t)\rangle$ of the signal. The example in Fig. 5.2E (circles) shows strong ITD tuning. The magnitude of tuning was, again, quantified by the vector strength, which was $r = 0.42$ ($p = 0.026$) here. The minimum variance, e.g. at ITD $\approx 20\mu$s, was below the variances of both monaural responses. This behavior was different compared to the variances of the full responses shown in Fig. 1E (same recording location) where the binaural variance was always larger than the monaural ones.

The example shown in Fig. 5.2E was typical for all recording locations: the ITD tuning of $\mathrm{V}ar\langle r_B(t)\rangle$ was strong (vector strength $r = 0.41 \pm 0.09$, range from 0.16 to 0.50, all $p \leq 0.03$). The signal variances for monaural and binaural stimulations ranged over five orders of magnitude across recording locations (Fig. 5.2F). Even at those recording locations at which the cyclic mean was relatively small in amplitude, the quality of the ITD tuning was not affected: in the population, the variance of the cyclic mean was uncorrelated to the strength of the ITD tuning ($CC = 0.17$, $p = 0.19$ (t-test), $N = 58$).

The second important property of the binaural signal $\langle r_B(t)\rangle$ is its time course. We utilize the PSD to infer the time course (example in Fig. 5.2D). Because the second harmonic was much smaller than the peak at the stimulus frequency, the binaural signal was highly sinusoidal. At the 58 recording locations, the median level of the second harmonic was $-44$ dB (interquartile range: 12 dB) below that of the first harmonic at the best ITD. For the worst ITD, the median of the second harmonic was $-20$ dB (interquartile range: 14 dB) lower. As a consequence, we could describe the time course of the binaural signal by the simple model

$$\langle r_B(t)\rangle = a_B \sin(2\pi\, f_{stim}\, t + \phi_B) \ , \tag{5.3}$$

where $a_B$ is the amplitude and $\phi_B$ is the phase of a sine function, and $f_{stim}$ is the stimulus frequency. Please note that both $a_B$ and $\phi_B$ may depend on ITD, and that the signal is mean-free. The variance

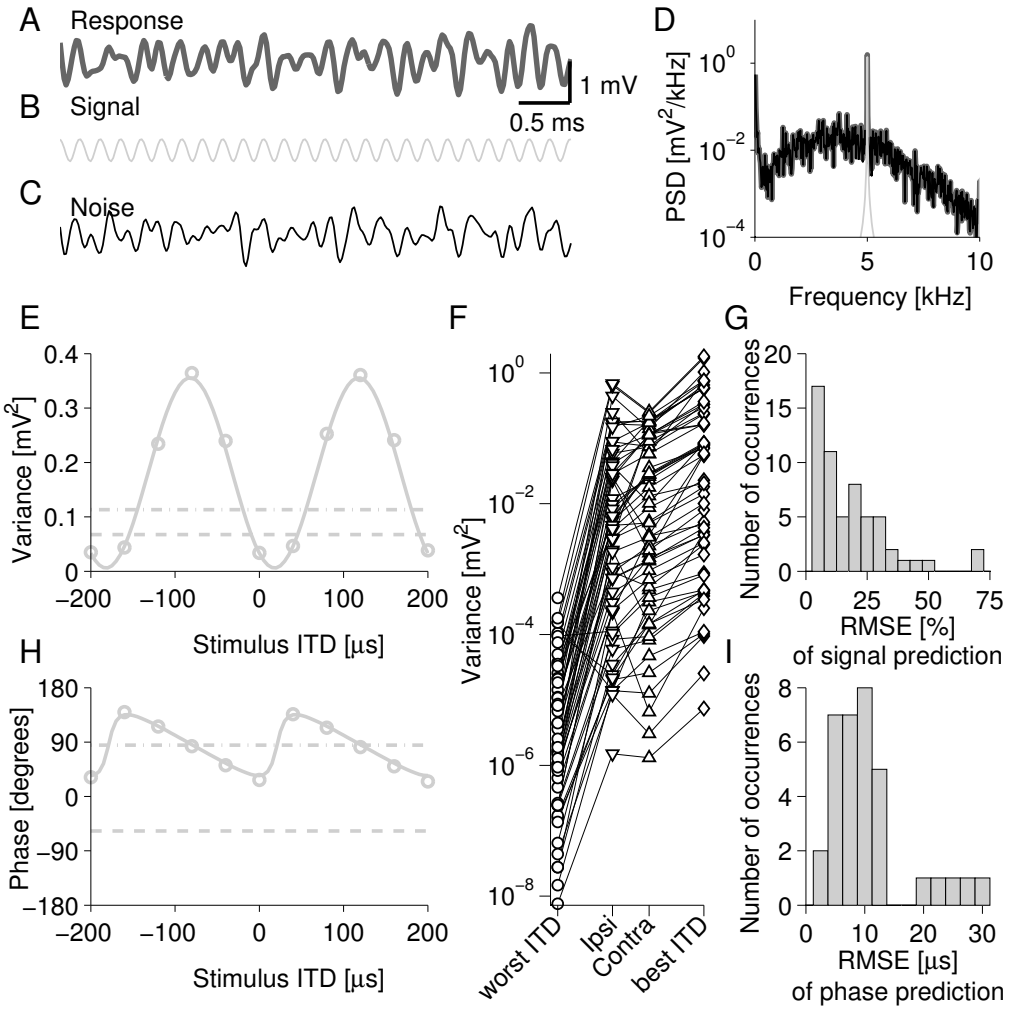


Figure 5.2.: The cyclic mean signal can be predicted from the monaural activity. *A–C:* A response (*A*) can be separated to the cyclic mean signal (*B*) and noise (*C*). *D:* The power spectral densities (PSD) of the signal (light gray) and the noise (black) sum up to the PSD of the response. *E:* Variance of the cyclic mean signal as a function of interaural time difference (ITD) of binaural tones (circles). The horizontal dashed and dash-dotted lines represent the variances in response to monaural stimulation at the ipsi- and contralateral sides, respectively. The solid line is the prediction of the linear model. *F:* Variance of the cyclic mean signal of all recording locations for binaural stimulation at worst ITD (squares), monaural stimulation (downwards triangles: ipsilateral, upwards triangles: contralateral) and binaural stimulation at best ITD (diamonds). At 15 locations out of 58 the ipsilateral variance exceeded the contralateral one. *G:* Histogram of root mean squared errors (RMSE) of cyclic mean predictions at 58 recording locations. *H:* The phase of the response as a function of the ITD. *I:* Histogram of the RMSEs of phase predictions in the population. The RMSE was measured in $\mu$s: Pred. error [$\mu$s] = Pred. error [cycles]/$f_{\mathrm{stim}}$. *A – E* and *H:* recording location: 502.18.3-4-8.

and the amplitude of the signal are then related through

$$\mathrm{V}ar\langle r_B(t)\rangle = \frac{a_B^2}{2} \ . \tag{5.4}$$

Signals in response to monaural stimulation are also highly sinusoidal (Kuokkanen et al., 2010). We therefore can describe signals $\langle r_I\rangle$ and $\langle r_C\rangle$ in response to ipsi- and contralateral stimulation, respectively, by

$$\langle r_I(t)\rangle = a_I \ \sin(2\pi \, f_{stim} \, t + \phi_I) \tag{5.5}$$

and

$$\langle r_C(t)\rangle = a_C \ \sin(2\pi \, f_{stim} \, t + \phi_C) \tag{5.6}$$

with amplitudes $a_I$ and $a_C$ and phases $\phi_I$ and $\phi_C$ of sinusoids oscillating at the stimulus frequency $f_{stim}$. These descriptions of averaged responses are instrumental for a first test of the linear-summation hypothesis.

### 5.4.4. Prediction of the binaural cyclic-mean signal from monaural signals

The linear-summation hypothesis in equation (5.1), which states that the binaural response is the sum of ipsi- and contralateral inputs, can be tested for cyclic-mean signals. Because the average $\langle \ldots \rangle$ is linear, equation (5.1) leads to

$$\langle r_B(t)\rangle = \langle r_I(t)\rangle + \langle r_C(t)\rangle \ . \tag{5.7}$$

We showed that cyclic means are highly sinusoidal and that they can be approximated by sine functions; see equations (5.3), (5.5), and (5.6). Using these models in equation (5.7), we find relations for the amplitudes and for the phases. The linear-summation hypothesis therefore predicts that the binaural signal has amplitude

$$a_B = |a_I + a_C \cdot \exp[i \, (\phi_I - \phi_C)]| \tag{5.8}$$

and phase

$$\phi_B = \arctan\left(\frac{a_I \sin\phi_I + a_C \sin\phi_C}{a_I \cos\phi_I + a_C \cos\phi_C}\right) \ , \tag{5.9}$$

where $\phi_C = \phi_C(\mathrm{ITD})$. We note that the branch of the arctan needs to be chosen appropriately.

The predicted amplitudes (or variance) and phases (solid lines in Figs. 5.2E and H, respectively) matched the measured ones (circles). The root mean squared error (RMSE) of the amplitude prediction was $8.2 \cdot 10^{-3}$ mV$^2$, which could be separated into a bias term $-4.0 \cdot 10^{-3}$ mV$^2$ and a deviation term $7.2 \cdot 10^{-3}$ mV$^2$. To compare errors across recording locations, we normalized values by the mean variance across stimulus ITDs for each recording location. In the example in Figure 5.2E, where we had a mean binaural variance of $160 \cdot 10^{-3}$ mV$^2$ for the cyclic mean, the normalized RMSE was 5.2 %, the normalized bias was $-2.5$ %, and the normalized deviation was 4.6 %. In the population, normalized values were $18 \pm 16$ % (RMSE, Fig. 5.2G), $-1 \pm 20$ % (bias) and $11 \pm 8$ % (deviation).

Similarly to response amplitudes (Eq. 5.8), the binaural phases were also well described by the linear prediction (Eq. 5.9). The predicted phase in Figure 5.2H had an RMSE of 4.7 degrees with a bias $-2.9$ degrees and a deviation 3.7 degrees. To compare predictions across locations, we divided these values, in cycles, by the stimulus frequency (in the example 5.0 kHz), which leads us to a temporal precision. The normalized values in the example were 2.6 $\mu$s (RMSE), $-1.6$ $\mu$s (bias) and 2.0 $\mu$s (deviation). In the population, the normalized values were $10 \pm 8$ $\mu$s (RMSE, Fig. 5.2I), $-8 \pm 14$ $\mu$s (bias) and $7 \pm 6$ $\mu$s (deviation). In the population, there were several typical shapes of the phase-ITD tuning curves, including the sawtooth-like (Fig. 5.2H) with a 90° jump, a monotonically decreasing one and one resembling a sinusoid. However, the physiological interpretation of these shapes is beyond the

scope of this study.

To summarize, for all applied stimulus frequencies and all applied ITDs, there was a good agreement between the measured binaural amplitude and phase of the signal and the predicted values, when we used the linear waveform-summation model of monaural responses to explain the binaural responses.

### 5.4.5. Prediction of the binaural noise variance from monaural and spontaneous noise variances

To further test the linear-summation hypothesis, we also analyzed the properties of the noise. The noise $n$ was defined in equation (5.2) and in Figure 5.2A–C. Here, for example, binaural noise $n_B$ is the binaural response $r_B$ minus the cyclic mean binaural response $\langle r_B(t)\rangle$:

$$n_B(t) = r_B(t) - \langle r_B(t)\rangle \ . \tag{5.10}$$

To get rid of trial-to-trial fluctuations in the time course of the noise, we quantified the noise by means of its variance

$$\sigma_B^2 = \mathrm{V}ar\left[n_B(t)\right] \ . \tag{5.11}$$

Our linear prediction was that if the noise was related to the activity of the NL neurons, it should vary with ITD, whereas if it was mainly related to the input to NL, it should not show this ITD tuning. Interestingly, the binaural noise variance $\sigma_B^2$ was only weakly tuned to ITD (Fig. 5.3A, circles). In this example, the vector strength ($r = 0.017$, $p = 0.03$) was small but significant. The binaural noise variance was larger than the variances of the two monaural stimulations (dashed and dot-dashed lines), and those were even larger than the variance of the spontaneous activity (dotted line). This ordering of the magnitude of variances was observed at all recording locations (Fig. 5.3B) and implies that the noise, similarly to the signal, shows some tuning to the stimulus even though the binaural noise variance was independent of the ITD.

The vector strength in the population was small ($r = 0.012 \pm 0.008$, range from 0.002 to 0.043, Fig. 5.3C, length of arrows). At 15 recording locations (out of 58) the vector strength was significant at $p < 0.05$.

Although the noise variance was weakly tuned to ITD, there was nevertheless a preferred phase of tuning (e.g. ITD = 134 $\mu$s in Fig. 5.3A). To test whether this preferred ITD of the noise response was related to the ITD tuning of the signal (e.g. 118 $\mu$s in Fig. 5.2E), we took the difference $\Delta = 134-118$ $\mu$s of the two values and converted it to a phase $D = 360^\circ \cdot \Delta \cdot f_{\mathrm{stim}}$, which was $D = 29.6^\circ$ for $f_{\mathrm{stim}} = 5000$ Hz in this example. The direction of the noise variance in the population was $D = 18 \pm 46^\circ$ (circular mean $\pm$ circular SD, Fig. 5.3C, direction of arrows) and the mean direction of the noise variances weighted with the respective vector strengths was 16.9° (Fig. 5.3C, gray arrow).

Can we predict the binaural noise variance $\sigma_B^2$ from the monaural noise variances $\sigma_I^2$ and $\sigma_C^2$ with the linear model? To do so, we need to consider that the noise $n_B$ measured with binaural stimulation may be composed of at least three types of sources: noise due to ipsilaterally driven input, $n_{driven,I}$, noise due to contralaterally driven input, $n_{driven,C}$, and also background noise $n_{background}$ that is unrelated to acoustic stimulation. We tentatively neglect here further noise sources, for example due to the activity of NL neurons. To summarize,

$$n_B(t) = n_{driven,I}(t) + n_{driven,C}(t) + n_{background}(t) \ . \tag{5.12}$$

If these three noise sources are uncorrelated, the corresponding noise variances add up:

$$\sigma_B^2 = \sigma_{driven,I}^2 + \sigma_{driven,C}^2 + \sigma_{background}^2 \ . \tag{5.13}$$

Unfortunately, the three noise variances on the right-hand side of the equation (5.13) cannot be

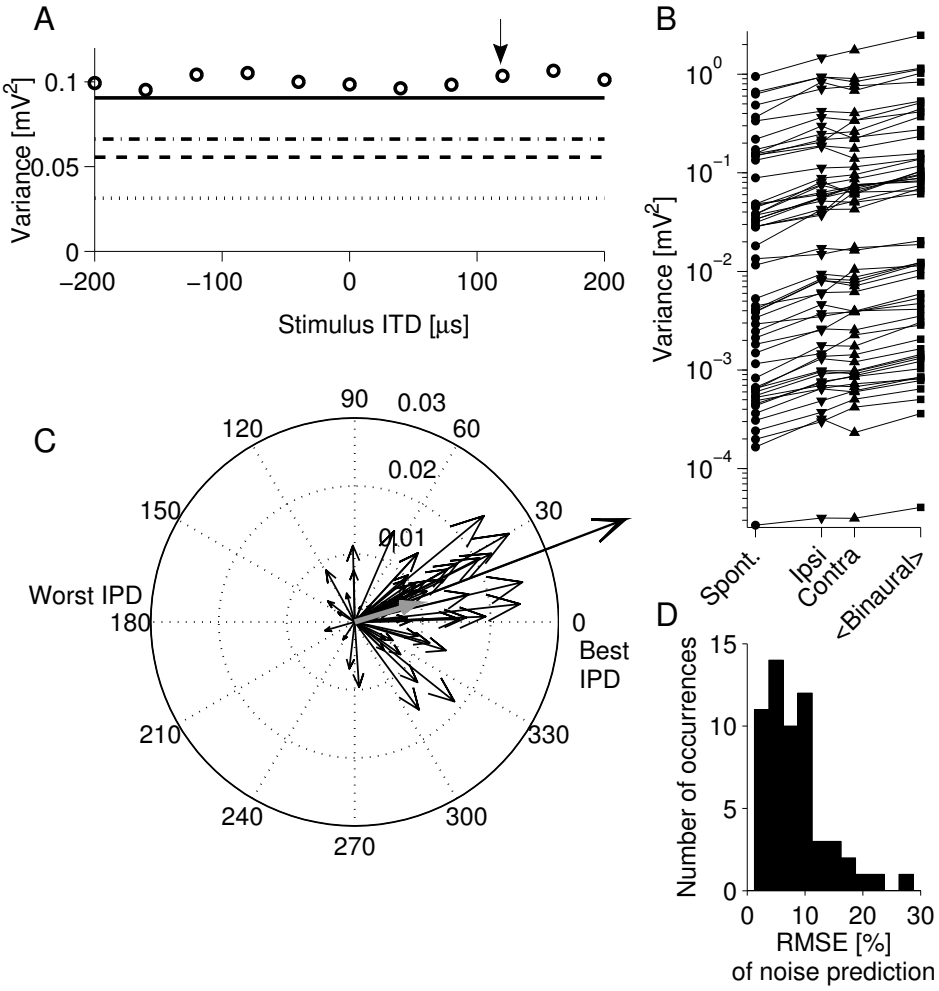


Figure 5.3.: Noise variance is weakly ITD tuned. *A:* The variance (circles) of the noise showed small ITD modulation (vector strength: $r = 0.017$, $p = 0.03$). The mean direction (134 $\mu$s) of the modulation is shown by the arrow. The horizontal dashed and dash-dotted lines represent the variances in response to monaural stimulation at the ipsi- and contralateral sides, respectively. The dotted line indicates the variance of the spontaneous activity. The solid line is the prediction of the linear model. Recording location: 502.18.3-4-8. *B:* The variance of the noise at 58 recording locations for spontaneous activity (circles), monaural stimulation (downwards triangles: ipsilateral, upwards triangles: contralateral) and binaural stimulation (mean over all ITDs, squares). *C:* The mean directions of the noise variances for 58 recording location are represented by the angles of the arrows. The length of each arrow indicates the vector strength of the ITD tuning of the noise component. The thick gray arrow shows the mean vector strength and mean direction of the population. *D:* Histogram of RMSE of the noise predictions at 58 recording locations.

determined separately. One can measure, instead, the noise $n_I(t)$ for ipsilateral stimulation, the noise $n_C(t)$ for contralateral stimulation, and the noise $n_{spont}(t)$ for spontaneous activity. As argued above (Eq. 5.12), $n_I(t)$ may be composed of three components:

$$n_I(t) = n_{\mathrm{d}riven,I}(t) + n_{spont,C}(t) + n_{\mathrm{b}ackground}(t) \ , \tag{5.14}$$

where $n_{spont,C}$ is the noise due to spontaneous activity of the contralateral input to NL. This term corresponds to (but is different from) the term $n_{\mathrm{d}riven,C}$ in equation (5.12). For uncorrelated noise sources, equation (5.14) leads to

$$\sigma_I^2 = \sigma_{\mathrm{d}riven,I}^2 + \sigma_{spont,C}^2 + \sigma_{\mathrm{b}ackground}^2 \ . \tag{5.15}$$

Similarly, the noise variance $\sigma_C^2$ for contralateral acoustic stimulation can be described by

$$\sigma_C^2 = \sigma_{spont,I}^2 + \sigma_{\mathrm{d}riven,C}^2 + \sigma_{\mathrm{b}ackground}^2 \ . \tag{5.16}$$

Furthermore, the "spontaneous" noise for no acoustic stimulation at all can be described by

$$\sigma_{spont}^2 = \sigma_{spont,I}^2 + \sigma_{spont,C}^2 + \sigma_{\mathrm{b}ackground}^2 \ . \tag{5.17}$$

Using equations (5.15), (5.16), and (5.17) in equation (5.13), we finally arrive at the prediction

$$\sigma_B^2 = \sigma_I^2 + \sigma_C^2 - \sigma_{spont}^2 \ . \tag{5.18}$$

All quantities in equation (5.18) can be directly measured. We note that there is a minus sign before $\sigma_{spont}^2$. The linear-summation hypothesis therefore predicts how the variance $\sigma_B^2$ of the noise for binaural stimulation depends on the measured noise variances $\sigma_I^2$ and $\sigma_C^2$ in case of monaural stimulation and on noise $\sigma_{spont}^2$ for spontaneous activity.

The prediction error of the noise was normalized similarly to the prediction error of the cyclic mean signal. In the example in Fig. 5.3A (solid line) the prediction had 10.8 % RMSE, −10.2 % bias and 3.7 % deviation. At the population level, the prediction of the noise variance matched the data well (RMSE: $8 \pm 6$ %, Fig. 5.3D, bias: $-2 \pm 9$ %, deviation: $3 \pm 1$ %).

The good match between prediction and data further support our hypothesis that the NL neurons' contribution to the neurophonic is small and that the noise reflects the activity of the inputs to the NL. The small difference between the prediction and the data may be explained by the activity of the NL neurons.

### 5.4.6. Prediction of the binaural response variance

After having considered the binaural signal and noise separately, we revisit the binaural response $r_B(t)$. From Eq. (5.10) we find

$$\mathrm{V}ar[r_B(t)] = \mathrm{V}ar\left[\langle r_B(t)\rangle + n_B(t)\right] \ , \tag{5.19}$$

and, assuming that binaural signal and noise are uncorrelated, equations (5.4) and (5.11) lead us to

$$\mathrm{V}ar[r_B(t)] = \frac{a_B^2}{2} + \sigma_B^2 \ . \tag{5.20}$$

The assumption that signal and noise are uncorrelated is supported by the strong ITD tuning of the signal and the absense of the ITD tuning in the noise. Figure 5.4A–C outlines for three examples the predicted (solid lines) and measured (circles) response variances. Although the recorded response variances spanned over five orders of magnitude (Fig. 5.4D), the binaural response variance were predicted well by the spontaneous and monaural responses (Fig. 5.4E). The RMS error of the prediction was

$9 \pm 6$ % with a bias $-3 \pm 10$ % and a deviation $4 \pm 3$ %. The prediction errors of response, signal and noise were not correlated with the magnitude of the respective binaural variances (|correlation coefficient| $< 0.11, p > 0.4$ for each).

In summary, the linear model based on the 'input-hypothesis' and monaural responses predicted the variance of the binaural neurophonic well. Only weak non-linearities were found, supporting the hypothesis that the input to NL is the overwhelming source of the neurophonic potential in NL of the barn owl.

## 5.5. Discussion

We showed that in the barn owl NL the sum of the neurophonic potentials in response to ipsi- and contralateral stimulation accurately predict the responses to binaural stimulation at arbitrary ITDs. The fundamental assumption underlying this linear model is that the inputs to NL, i.e., afferent axons within NL and synaptic input onto NL neurons, are the main sources of the neurophonic potential. Because the binaural response can be predicted by a linear model, nonlinearities as generated by NL coincidence detector neurons were not necessary to explain the strong ITD tuning of the neurophonic.

### 5.5.1. ITD tuning of neurophonic can be explained by ITD tuning of the phase-locked signal

The ITD tuning of the neurophonic potential in response to binaural tones can be fully accounted for by the ITD tuning of the phase locked part of the response. This phase locked part of the response was called "signal", and the residual, non-phase locked part was defined as "noise". The amplitude of the signal always exhibited a strong ITD tuning, and this tuning was strong even in recordings in which the ITD tuning of the full response (= signal + noise) was weak (vector strength close to 0.02); in these responses, the strong ITD tuning of a small signal was masked by a weak ITD tuning of large noise. Although the vector strengths of the ITD tuning in the response and in the signal could be very different, they were correlated (correlation coefficient 0.37, $p = 0.004$).

Monaural and binaural signals, which are the result of averaging extracellular field potentials over many stimulus cycles, turned out to be highly sinusoidal; both the amplitude and the phase of the binaural signal were predicted well by the sum of monaural signals. We note that for the binaural phase the median prediction error was only 9 $\mu$s (phase was normalized by the variable stimulus frequency), which is smaller than the sampling interval 22.7 $\mu$s in the measurements. The prediction error was in the same range as the previously reported temporal precision $< 20$ $\mu$s of the neurophonic (Wagner et al., 2005). The normalized root mean squared error (RMSE) of the predicted binaural signal amplitude was $18 \pm 16$ %. In general, errors might at least partly be due to nonstationarities of recordings because monaural and binaural responses were measured with a temporal delay of typically several minutes.

There were two recording locations with high RMSE ($> 70$ %). For both, the bias was more than 60 %. One of them could clearly be identified to be situated at the border of NL, and the contralateral cyclic mean signal was two orders of magnitude smaller than the one in response to ipsilateral stimulation. For the other one, the ipsilateral cyclic mean signal was one order of magnitude smaller than the contralateral one, but no further obvious reason could be identified.

### 5.5.2. Weak ITD tuning of noise implies small contributions from NL neurons to the neurophonic

Mechanistically, the amplitude of the signal is proportional to the population firing rate times the population vector strength of the neural elements within NL, most of which fire phase-locked to the stimulus (Kempter et al., 2001; Kuokkanen et al., 2010). On the other hand, the residual noise represents

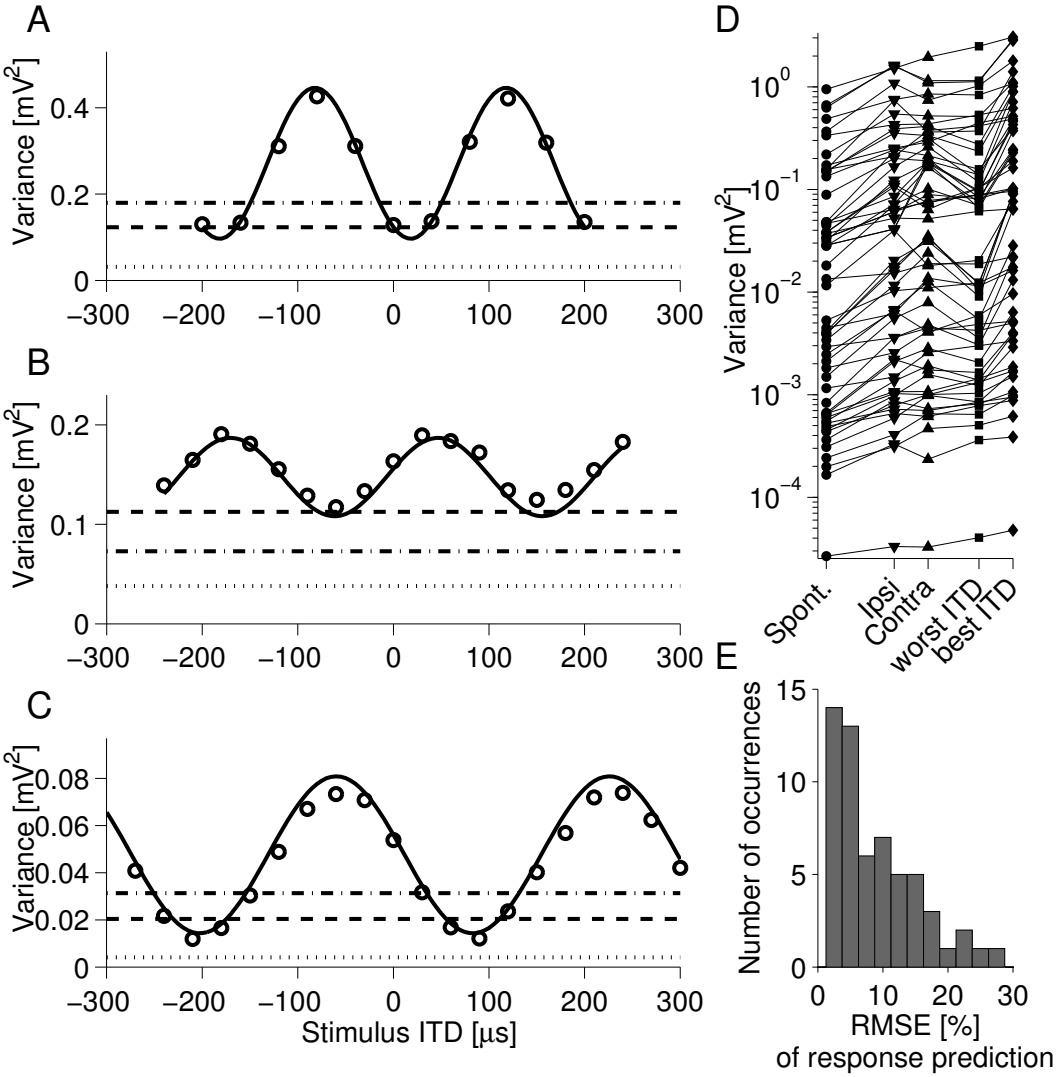


Figure 5.4.: Waveform summation accurately predicts the ITD tuning of the response variance. *A–C:* Variances (circles) of the noise as a function of interaural time difference (ITD) of binaural tones. The horizontal dashed and dash-dotted lines indicate the variances in response to monaural stimulation at the ipsi- and contralateral sides, respectively. The dotted line indicates the variance of the spontaneous activity, and the solid line indicates the prediction of the linear model. RMSE, bias and deviation of each prediction and recording location, respectively: *A:* RMSE: 6.4 %, bias: −5.4 %, deviation: 3.6 %; 502.18.3-4-8. *B:* RMSE: 6.6 %, bias: −6.0 %, deviation: 2.6 %; 502.10.1-6-7. *C:* RMSE: 12.7 %, bias: 8.8 %, deviation: 9.1 %; 122.05.1-3-4. *D:* The variance of the response of all recording locations for spontaneous activity (circles), monaural stimulation (downwards triangles: ipsilateral, upwards triangles: contralateral) and binaural stimulation (worst ITD: squares, best ITD: diamonds). *E:* RMSE of response prediction in the population.

the activity of neural elements that contribute to the extracellular field potential independently of their phase locking. The noise variance is therefore a signature for the mean neuronal activity in the immediate vicinity ($< 150$ $\mu$m) around the recording electrode (Kuokkanen et al., 2010; Lindén et al., 2011).

To test whether ITD tuning of the mean neuronal activity in NL can be observed in the extracellular field potential, we studied the ITD tuning of the noise variance. Interestingly, the noise variance of the binaurally stimulated data did not show ITD tuning at most recording locations, and the vector strength was always small and below 0.043. However, at 17 (out of 58) recording locations, ITD tuning was significant at $p < 0.05$. Overall, the ITDs that gave rise to the largest noise variances were different from the best ITDs of the binaural signals ($D = 18 \pm 46°$, normalized by the stimulus frequency). Funabiki et al. (2011) have recently reported a difference in a similar range ($41.3 \pm 40.3°$) between the the spike rate ITD tuning of the NL neurons and neurophonic ITD tuning. As Funabiki et al. (2011) suggest, this difference might be due to the NL axons contributing to the neurophonic potential, instead of the NL cell bodies. Because the NL axons run along the ITD gradient, orthogonal to the delay line axons within the NL (Sullivan and Konishi, 1986; Carr and Boudreau, 1993a), the ITD tuning of the axon should be phase shifted with respect to the neurophonic. Furthermore, in the NL neurons the action potential is thought to be generated in the first node of Ranvier (Ashida et al., 2007), giving rise to strong conductances beyond the cell body.

The very weak ITD tuning of the noise variance suggests that the neural elements that significantly contribute to the extracellular field potential in NL do not change their mean activity as a function of ITD. We note that the mean activity of the bilateral inputs to NL is independent of ITD whereas the mean activity of NL neurons strongly varies as a function of ITD (Peña et al., 1996; Köppl, 1997b). As a result, the contribution of NL action potentials to the neurophonic can be assumed to be small.

### 5.5.3. Linear prediction of noise variance and the summation ratio

The conjecture that contributions of NL action potentials to the noise are negligible allowed us to predict the binaural noise variance $\sigma_B^2$ from the ipsilateral ($\sigma_I^2$) and contralateral ($\sigma_C^2$) response variances and the variance $\sigma_{spont}^2$ of spontaneous activity. The linear model led to the prediction $\sigma_B^2 = \sigma_I^2 + \sigma_C^2 - \sigma_{spont}^2$, which matched the binaural data well: the RMSE was only $8 \pm 6$ %.

The linear model for noise variances is related to the "summation ratio" (SR) as defined by (Goldberg and Brown, 1969)

$$SR = \frac{R_B - R_{spont}}{R_I - R_{spont} + R_C - R_{spont}}$$

where $R_B$, $R_I$, $R_C$, and $R_{spont}$ are the firing rates in response to binaural, ipsilateral and contralateral stimulation, and the spontaneous activity, respectively. The SR quantifies the relationship of the activities: $SR = 1$ represents linear summation of monaural rates whereas $SR < 1$ indicates 'disfacilitation' and $SR > 1$ indicates 'facilitation' (Goldberg and Brown, 1969; Peña et al., 1996).

The SR has been applied to NL neurons' firing rates. At the worst ITD, sustained firing rates were smaller than or similar to their monaurally driven rates (Carr and Konishi, 1990; Peña et al., 1996), and Peña et al. (1996) reported disfacilitation at $SR = 0.50 \pm 0.05$. On the other hand, at the most favorable ITD, sustained firing rates can exceed the sum of monaural discharge rates (Carr and Konishi, 1990; Peña et al., 1996), and Peña et al. (1996) found facilitation at $SR = 1.51 \pm 0.27$. Thus, NL neurons operate in the regime of nonlinear coincidence detectors extracting the signal amplitude of oscillatory input (Peña et al., 1996; Kempter et al., 1998b).

The noise variance can be associated with the local mean neuronal activity (Kuokkanen et al., 2010), as argued above. Assuming that the noise variance is proportional to the firing rate, i.e., $R_B \propto \sigma_B^2$, $R_I \propto \sigma_I^2$, $R_C \propto \sigma_C^2$ and $R_{spont} \propto \sigma_{spont}^2$, we find from the measured noise variances the summation ratio $SR = 1.00 \pm 0.03$. This value indicates linear summation (Goldberg and Brown, 1969), as predicted by the linear model. Indeed, the original expression for the summation ratio at $SR = 1$ and the linear

model for noise variances are equivalent if firing rates are proportional to noise variances.

### 5.5.4. Predictions of extracellular potentials

The generative mechanisms of the extracellular field potential (EFP) have been subject to intensive research recently, and only recently predictions of EFPs have been compared to physiological data. Various models generating an EFPs to compare with the data have been used.

A field potential created by the currents from one cell can be modeled in a forward fashion, like e.g. Gold et al. (2006); Pettersen et al. (2008) and Lindén et al. (2010) have done. Assuming population activity (with or without tuning), in which each spike is presented by a certain spike waveform, can also produce a good estimate of the EFP (Katzner et al., 2009; Kuokkanen et al., 2010). Toward population models, it is possible to assume one filter for the activity of each of similar sources (instead of one spike waveform for each source) (Nagel and Wilson, 2011), or even estimate different frequency components of the EFP (such as the multi-unit activity and the local field potential) from extracellular measurements by current source density analysis (Pettersen et al., 2006; Einevoll et al., 2007). Also predictions about the intracellular features can be done from the extracellular measurements, for better separation of single spike waveforms (Henze et al., 2000; Harris et al., 2000). Aforementioned methods have been used to show that the LFP can be predicted. However, all of them need to know, or try to estimate, the contribution of a single cell or source (in the sense of CSD analysis) in the LFP.

In contrast to the aforementioned studies, the method presented here estimates tuned activity of two populations. However, no spike waveform is needed for the prediction done here. Instead, our analysis predicts that usually the spike waveform (or the filter representing the population activity of the input from NM) in NL does not change much between stimuli, whichever its shape might be.

### 5.5.5. Conclusion

We conclude that the nonlinear behavior of the NL coincidence detector neurons (summation ratio $\approx 1.5$), which is the output of this brain structure, is only weakly, if at all, represented in the extracellular field potential within NL. Conversely, the neurophonic mainly represents the input to NL. Our results therefore strongly support the hypothesis by (Sullivan and Konishi, 1986) that the neurophonic response to binaural stimulation is essentially waveform summation of the monaurally stimulated neurophonic responses. Also theoretical and computational work on the development of temporal feature maps in NL had suggested that the neurophonic reflects the input to NL (Kempter et al., 2001; Leibold et al., 2001a; 2002). Understanding the origin of the neurophonic is therefore essential for understanding how maps of ITD with a sub-millisecond precision can be set up during development. Future work to test the input hypothesis may include a spectral analysis of the neurophonic. The contribution of NL action potentials, which here was not detectable in broadband noise, might be significant in particular frequency bands around 1 kHz. However, recordings much longer than those available for this study are necessary to further elucidate the origin of extracellular field potentials.

# 6. Spectral Components of the Neurophonic

## 6.1. Summary

Putative generators of the neurophonic potential are the activity of afferent axons from NM, synaptic activation onto NL neurons, and spikes of NL neurons. The source of the neurophonic is mainly the input to NL, i.e. the afferent axons and their synaptic activation onto NL neurons. The question remaining is how much does the activity of the NL neurons contribute to the neurophonic potential. It is possible to differentiate between these putative generators while analyzing the neurophonic, since between the worst and the best ITD, the NL neurons' activity changes dramatically, but the activity of putative generators related to the input to NL does not change essentially. To clarify the roles which the different generators play in the spectrum of the neurophonic, we analyzed spectra of extracellular in-vivo responses to acoustic stimulation with tones, and changed the ITDs of the binaural stimulations[1].

We found that from the worst to the best ITD, the spectral components $< 500$ Hz had a small but systematic peak, corresponding to the increasing spiking activity of the NL neurons. We also compared the spontaneous activity to the activity at the worst ITD, which mainly changes the activity of the input sources (i.e. NM axons and their synapses to NL neurons). We found that then the amplitude of the spectrum had a peak either around $1-2$ kHz and/or around $3-4$ kHz. Comparing the spontaneous activity and the activity at the worst ITD we also found a notch at low frequencies around 200 Hz. The origin of this notch is not clear. However, the main source contributing at these low frequencies might be independent of the stimulus and thus independent of the correlated increase in the neural activity.

## 6.2. Introduction

In the extracellular field potential (EFP) there is often a large difference between the power spectral densities of the spontaneous activity and the driven activity (Tokioka et al., 2000; Burns et al., 2010a;b). The spectra are also modulated by the stimuli, corresponding to the proportions of the activity of many neuronal components changing simultaneously (Nikonov et al., 2002; Henrie and Shapley, 2005). Furthermore, the origin the EFP is not well known in most systems. The low-frequency components (LFP) are usually accounted for the synaptic currents (Mitzdorf, 1985; Nunez and Srinivasan, 2006; Gold et al., 2006; 2007), whereas the high-frequency component reflects typically the spiking activity of several neurons (Logothetis et al., 2001; Pettersen et al., 2008; Galindo-Leon and Liu, 2010; Kajikawa and Schroeder, 2011). However, both of these components usually originate from a complex pattern of neural activity. Only for most simple structures and stimuli, where the changes in the activity of all components with respect to stimuli are known approximately, can we identify the neural origin of the spectral components of the EFP. Such a simplicity is given for example for the neurophonic potential in the nucleus laminaris (NL), located in the auditory brainstem of the barn owl, in response to sustained tonal stimuli.

In the owl NL, the axonal spikes and synaptic inputs originating from the neurons in nucleus magnocellularis (NM) are the main source of the neurophonic (Kuokkanen et al., 2010; 2012). These

[1] The research presented in this chapter is the result of a collaboration with several researchers. I conceived the project, developed the analysis tools and performed the analyses of the experimental data. The experimental data was recorded by Catherine Carr and Hermann Wagner in their laboratories in University of Maryland, US and in RWTH Aachen, Germany.

sources represent the input to the nucleus, rather than the result of the coincidence detection performed in NL. The neurophonic is, furthermore, mainly of local origin ($\leq 300$ $\mu$m) (Kuokkanen et al., 2010). We ask whether it is possible to identify the minor contribution originating from NL neurons in the neurophonic. For tonal stimulation, the neurons' firing rate changes with ITD, whereas the activity of the other neural components (input to NL) stays constant (Peña et al., 1996; Köppl, 1997a;b). The changes in the variance of the neurophonic due to the changing firing rate of the NL neurons are minor and can only be observed at some recording locations (see chapter 5).

Our hypothesis is that the contribution from this 'output' activity change is detectable in the power spectral density (PSD) of the neurophonic, if present in it. The main question then is, to which frequencies of the response spectrum does this activity contribute, and with which intensity. We evaluate the spectral changes between spontaneous and driven activity as well as between driven activities in response to stimulation at the worst ITD and at the best ITD. We use for the evaluation the so called R-spectrum (Henrie and Shapley, 2005; Burns et al., 2010b;a), which shows the relative changes between the spectra. Analysis of the relative modulation of spectra (i.e., R-spectrum) has been used for EEG (Juergens et al., 1999) as well as for LFP (Siegel and König, 2003; Henrie and Shapley, 2005; Burns et al., 2010b; a.o.), mainly in the visual cortex. Usually, however, only the low-frequency components (LFP) have been analyzed for their modulation. Here we analyzed spectral components up to 10 kHz, and found changes in the spectra in the frequencies up to 6 kHz.

## 6.3. Materials and Methods

### 6.3.1. Experimental paradigm

Owl data were recorded as explained in the Appendix B. Data set 2 was analyzed for the results shown in this chapter (the same data set was used in the chapter 5). The data were pre-processed and pre-selected as described in the subsection 5.3.2.

### 6.3.2. Data analysis

There were two prominent features in the responses, namely the cyclic mean activity (or *signal*) and the *noise* (Kuokkanen et al., 2010; 2012) (see also Chapter 4 for definition). The signal comprises the phase-locked part of the response, or the peak of the spectrum at the stimulus frequency, and reflects both the level of the mean population activity and its phase locking. The noise is defined (Kuokkanen et al., 2010) by calculating the cyclic mean signal of the response and substracting that from the response. The noise does not capture the phase locking, but the mean population activity over all frequencies in the spectrum. Subsequently, the spontaneous activity only has a 'noise' component. The signal and noise components of the response served very different purposes in our analysis: the cyclic mean amplitude was used to judge the phase-locked activity level of the response, whereas only the noise was used to evaluate the subsequent changes in the spectrum. Figure 6.3A–C shows both the whole response (includling the peak at the stimulus frequency) as well as the noise component of the spectrum.

#### R-spectrum

R-spectrum measures the change in a spectrum at different frequencies, and is defined as (Henrie and Shapley, 2005)

$$R(f) = \frac{P_{\text{n, driven}}(f)}{P_{\text{spont}}(f)} \quad , \tag{6.1}$$

where $P_{\text{n, driven}}(f)$ is the spectrum of the noise in response to a stimulus eliciting high activity, and $P_{\text{spont}}(f)$ is the spectrum of the reference activity (e.g. spontaneous activity or response to a stimulus

eliciting low activity) .

In the R-spectra, a value of one represents 'no change in spectrum at this frequency' and values above one stand for 'increase in the spectrum at this frequency', i.e., a peak. Values between zero and one represent 'decrease in the spectrum at this frequency', i.e., a notch.

In each spectrum in response to stimulation, we excluded the contribution at the stimulus frequency, as well as a margin of 150 Hz around it, to enable the comparison of the spectra recorded at different stimulus frequencies. For spontaneous activity the exclusion of the spectral frequencies was neither needed nor done.

### Grouping and averaging of data

The spectra recorded in response to a given stimulus were noisy (Fig. 6.3). Furthermore, there were not many repetitions available per recording site ($11-51$ stimuli and $3-5$ repetitions per stimulus), and thus averaging over the repetitions did not decrease the noise level enough to enable identification of systematic changes in the spectra.

The spectra analyzed had the frequency resolution of 12.5 Hz, resulting from the duration of the data analyzed (80 ms were used). To reduce the noise level, we firstly took a running average (comprizing 10 points, i.e., 125 Hz) of each spectrum. Secondly, we developed a novel method for evaluating the spectra. We grouped recordings in response to binaural stimulation at each recording location into two subsets, namely 'high activity' and 'low activity'. The activity level was judged by the cyclic mean signal $A_c$ of the response, because it is the only response feature for the binaurally stimulated data that clearly changes with the ITD (Kuokkanen et al., 2012). If the cyclic mean amplitude of a response was lower than (or as low as) the average of all cyclic mean signal for the same stimulus type at the same location, the response was categorized into the 'low activity', i.e., 'worst ITD' group. If the cyclic mean signal was higher than the average, the response was in the 'high activity', i.e., 'best ITD' group. To average the spectra within each group, they were weighted with the distance $w_j$ of the $j^{th}$ cyclic mean signal $A_{c,j}$ of the response to the average cyclic mean signal $\langle A_c \rangle$, that is, $w_j = |A_{c,j} - \langle A_c \rangle|$. Thus, those responses representative for low or high activity were given more weight than those near the average. In each group, the average spectrum was normalized by the sum of all weigths $\sum_{n=1}^{N} w_n$ in the respective group having $N$ spectra. The changes in the spectra between worst and best ITD groups were studied with the so called R-spectrum (Henrie and Shapley, 2005) (see above).

## 6.4. Results

The aim of this chapter is to clarify the origin of different spectral components in the neurophonic responses to tonal stimuli. We may be able to distinguish components that are related firstly to the input to NL and secondly to the output of the NL neurons. Spontaneous activity in NL includes moderate activity originating from the NM of both sides (including NM axonal spikes and synaptic currents to the NL neurons) but low spiking activity of the NL neurons. Binaural stimulation at the worst interaural time difference (ITD) increases the activity in NMs to its maximum, but barely increases the firing rate of the NL neurons. In contrast, binaural stimulation at the best ITD increases the firing rate of the NL neurons to its maximum, but does not influence the spiking activity in either NM with respect to stimulation at the worst ITD. Thus, by comparing the spectra of the three aforementioned activity states, we wish to disentangle the changes in the spectra related to the input to the NL and the output of the NL. The recordings were done in six animals, and comprized 58 recording locations. Because of the small sample size, we did not test for the significance of some of the changes we observed. In the future, aqcuiring more data will hopefully enable us to solve this problem.

We separated the responses into *cyclic mean response (signal)* and *noise* (see e.g. Figs. 4.4 and 5.2 and Methods). The cyclic mean signal captures the phase-locked mean activity level of the neural

ensemble, whereas the noise depends on the mean activity level but is independent of the phase-locking (Kuokkanen et al., 2010).

In the example shown in the Figure 6.1A, the cyclic mean amplitude showed strong modulation with the ITD ($r = 0.42$, $p = 0.026$, calculated as shown in chapter 5), whereas the variance of the noise only showed a weak tuning to the ITD ($r = 0.017$, $p = 0.03$).

To reduce the noisiness of the spectra, the responses were grouped into two subsets based on the cyclic mean signal at each ITD. Namely, those showing a strong response to the stimulus (*'best ITD'*-group, e.g. ITD $\approx -100$ $\mu$s in Fig. 6.1A) and those showing a weak response (*'worst ITD'*-group, e.g. ITD $\approx 0$ $\mu$s in Fig. 6.1A). We took a weighted average across the spectra in each group (see Materials and Methods for details).

The shape of the averaged driven noise spectra was very similar independent of whether the stimulus was at the best or at the worst ITD (Fig. 6.1B) and the shape of the spectrum was relatively flat. Independent of the stimulus frequency, the noise spectrum typically increased nearly monotonically from about 0.5 kHz to $3 - 4$ kHz and decreased monotonically at frequencies above. At lowest frequencies ($< 400$ Hz) there was a strong peak in this example (Fig. 6.1B). At the population level the spectrum at one location had typically either a large peak or strong notch at the lowest frequencies.

The shape of the spectrum varied between different recording locations. We concentrated on the changes in the spectrum at each location for different stimulus conditions instead of its actual shape. Furthermore, we wanted to enable the comparison between recording locations. Thus, we used the so called R-spectrum (see Eq. (6.1)), i.e., the noise spectrum divided by a reference spectrum at the same recording location, to identify the changes in the spectral shape. The average of the R-spectrum corresponds closely to the variance of the noise normalized by the variance of the reference spontaneous activity (appendix A.2). The noise has also been shown to be related to the mean activity of the neural population from which the noise originated from, independent of the synchronization of these sources (Kuokkanen et al., 2010).

### 6.4.1. Input to and output of the nucleus laminaris

**Input to NL.** At the stimulation with the worst ITD, the input to NL is at its maximum, since both the ipsi- and the contralateral side are stimulated. However, the output, i.e., the activity of the NL neurons, is low, even smaller than in response to monaural stimulation (Peña et al., 1996). Thus, to identify how the input to NL influences the response spectrum, we analyzed the shape of the spectra in response to the worst ITD in comparison to the spontaneous activity in NL.

The spontaneous activity after the stimulation was typically suppressed (Fig. 6.1B). Thus, we set the reference activity to spontaneous activity recorded after monaural stimulation at a frequency far from the best frequency (BF) of the recording location (see also section 6.4.2). The reference spontaneous activity showed also a broad peak at and slightly above the BF of the recording location (B$F = 5.31$ kHz, defined as the mean of the BFs for the ipsi- and contralateral stimulations: B$F_i = 5.28$ kHz, B$F_c = 5.34$ kHz, see also Fig. 4.2 for the definition of the BF). This peak might be due to spontaneous activity of the auditory nerve fibers driving subsequent activity in the brainstem. The driven noise spectra did not show this broad peak, probably because the activity was locked strictly to the stimulus frequency.

There was a large peak in the R-spectrum around 1.3 kHz (Fig. 6.1C). There was also a second, lower but broader peak at about $3 - 4$ kHz. Furthermore, there was a clear notch at about the best frequency, corresponding to the lack of the broad peak in the driven activity in comparison to the spontaneous activity.

**Output of NL.** At the stimulation with the best ITD, the output of the NL neurons is at its maximum. However, the only change in the input, with respect to worst ITD stimulation, is the phase of monaural inputs with respect to each other. Because the noise spectrum is not affected by this change in the phase,

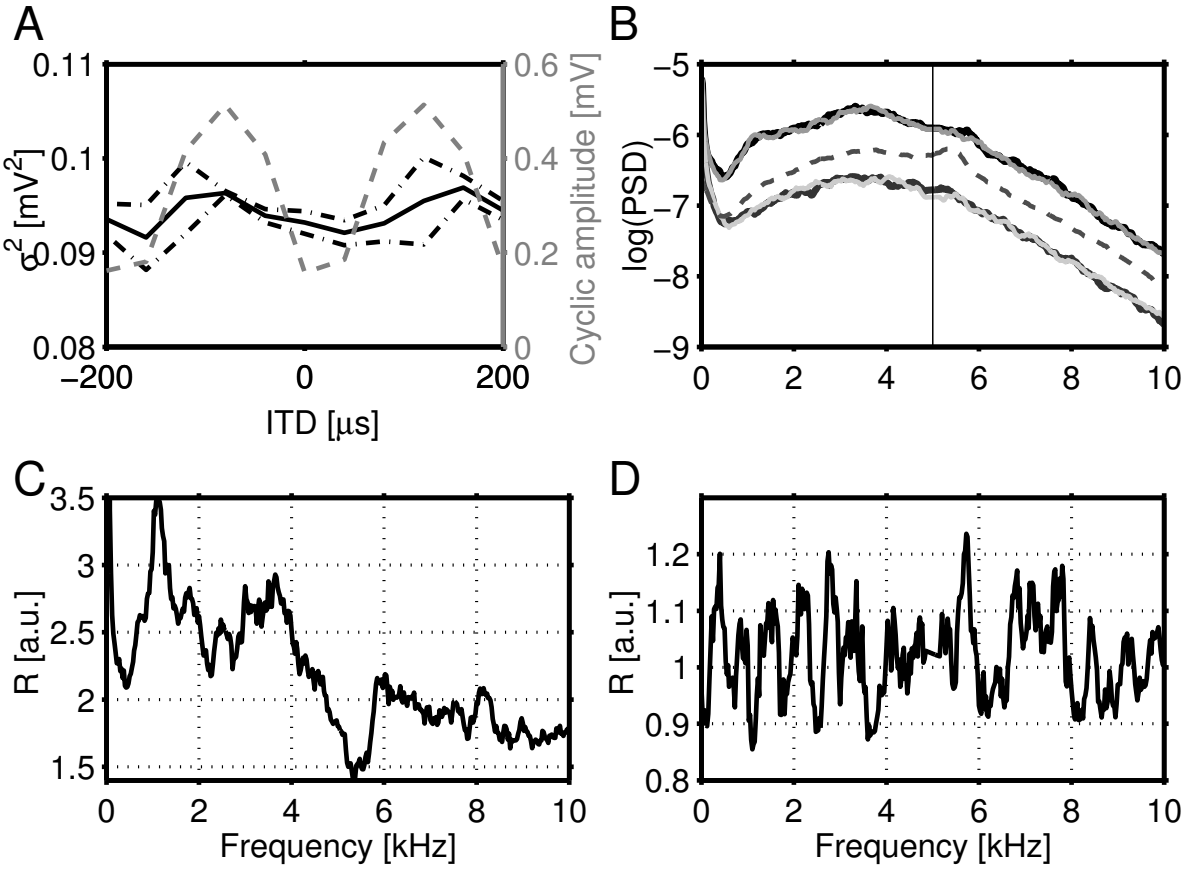


Figure 6.1.: Power spectral densities in response to binaural stimulation with varying ITDs and the corresponding spontaneous responses. *A:* Mean R-spectrum of the driven activity vs. reference spontaneous activity (black, dash-dotted lines mark mean ± S.D.) and cyclic mean amplitude (gray dashed line) as a function of the ITD. *B:* Averaged PSDs in response to high-driving ITD (upper black line) and to low-driving ITD (upper gray line), as well as corresponding spontaneous spectra immediately following (lower black and gray lines). Also the spectrum of the spontaneous activity is shown for reference (dashed line). The vertical line marks the stimulus frequency (5.0 kHz). *C:* R-spectrum of the worst ITD vs. reference spontaneous activity. *D:* R-spectrum of the best ITD vs. worst ITD. Recording site: 502.18.7.

the input spectrum remains constant from the worst ITD to the best ITD. Thus, the R-spectrum of the noise at the best ITD in comparison to the noise at the worst ITD can reveal the contribution of the NL neurons to the spectrum. However, individual R-spectra had a high variability around the value of one (Fig. 6.1D), and the difference between systematic changes and noisiness of the data was not clear.

### Input-related changes at population level

The spectral changes related to the input, as seen in Figure 6.1C for one recording location, were similar in population (Fig. 6.2A–B). All recording locations are shown ordered by the frequency at which the

maximum peak of the R-spectra occurred, within the frequency range $0.1 - 4$ kHz (Fig. 6.2A). The lower limit was selected because the data were band-pass filtered at $0.1 - 10$ kHz, and the higher limit was chosen so that all recording locations exhibited their first large peak withing this range.

There was a high variability in the mean level of the R-spectra (mean ± SD: $1.9 \pm 0.4$; range: 1.2 to 2.9, Fig. 6.2A). Thus, to visualize the changes more effectively, we normalized each R-spectrum to have an average of one and the range of $0 - 2$ (Fig. 6.2B, denoted by $\hat{R}$). The frequency range of the most pronounced peak was $0.75 - 2$ kHz (39 out of 58) or $3 - 4$ kHz (18 out of 58). One recording location showed a prominent broad peak throughout the low frequencies ($0 - 1$ kHz). The median frequency in the population at which the single highest value of the R-spectra was reached was 1.4 kHz. The height of the pronounced peak in non-scaled R-spectra was $2.8 \pm 0.8$ (mean ± SD), corresponding to $180 \pm 80$ % increase in the spectrum at the peak. We conclude that the input to NL has frequency components mostly around 1.4 kHz.

At low frequencies (restricted to range of $0.1 - 1.2$ kHz) the R-spectrum had a notch at all but two of the locations. The height at the low-frequency notch was $1.3 \pm 0.6$ at $200 \pm 160$ Hz (not scaled). At the high frequencies of the R-spectra ($3 - 10$ kHz), there was notch at about the BF (±500 Hz) at all but four of the 58 recording locations. The difference of the notch frequency and the BF was $-30 \pm 300$ Hz. The R-spectra had a tendency to decrease towards high frequencies. The origin of the low-frequency notch is not clear, but it might be an indication that the activity having most contributions at these frequencies is independent of the stimulation. The notch at about BF indicates that while some of the spontaneous activity was locked to frequencies at about BF, there was no such spontaneous locking in the binaurally driven activity.

### Output-related changes at population level

The noisiness of the R-spectra, was clearly visible at the population level (Fig. 6.2C). Furthermore, the R-spectra had a mean value of about one. Also these data were ordered by the frequency of their peak withing the range of $0.1 - 4$ kHz. After the R-spectra were normalized (Fig. 6.2D), some systematic changes in the spectra between the responses to best and to worst ITDs could be identified. About one third of the recording locations (21 out of 58) showed an increase of the spectrum at low frequencies ($100 - 500$ Hz) when the stimulus changed from the worst to the best ITD. For the rest, the peak of the change was distributed to higher frequencies ($0.5 - 2$ kHz: 18 out of 58, $2 - 4$ kHz: 19 out of 58). The median of the peak frequency was 1.4 kHz. The mean (non-normalized) peak height was very low, $1.26 \pm 0.14$, corresponding to a 26 % increase of the best ITD spectrum at the peak frequency with respect to the worst ITD spectrum.

Our previous analysis (see chapter 5) of the same data have shown that 17 of 58 recording locations exhibit small but significant ITD tuning of the noise in the response to binaural stimulation (black circles in Fig. 6.2D). The tuning was measured by vector strength (i.e., synchronization index). This ITD tuning of the noise can also be interpreted as a significant contribution from the NL neurons. The median frequency of the peak of the change among these locations was 300 Hz (range: 100 Hz to 2.95 kHz, 11 out of 17 $<$ 500 Hz, 6 out of 17 $>$ 500 Hz). We conclude that the activity of Nl neurons' spikes may contribute to the spectrum mostly at around 300 Hz. Furthermore, peaks seen at higher frequencies ($>$ 1 kHz) might result from our method of forcing to find a peak at a given frequency range.

### Correlations between input- and output-related changes

We had used the spectrum of the response to stimulation at the worst ITD for the calculation of the R-spectrum related to the input as well as the R-spectrum related to the output. Thus, we expected to see some correlations between these R-spectra. The changes in the input- and output-related R-spectra were weakly correlated. The strengths of the changes (peak heights) of the R-spectra in the population

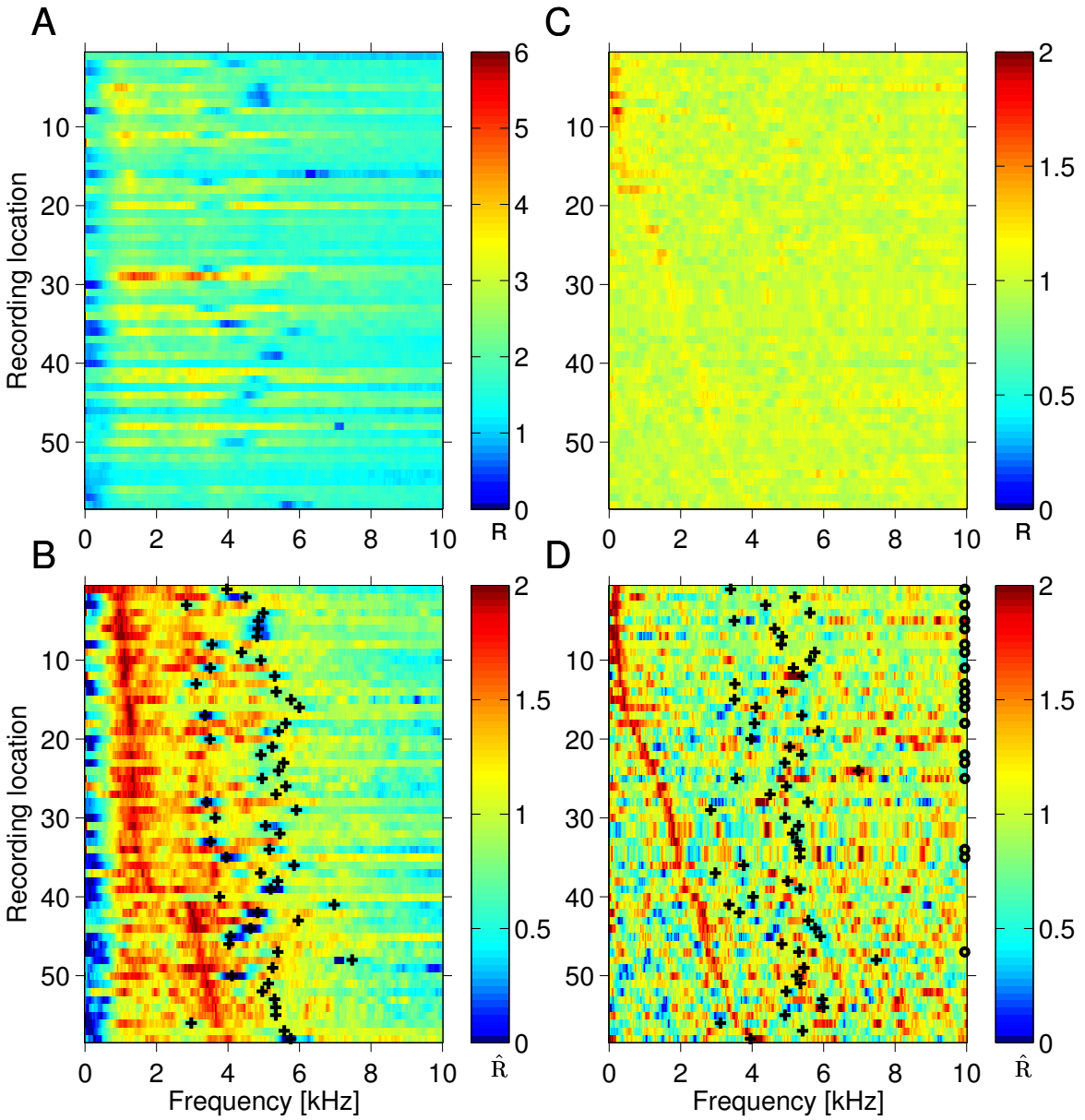


Figure 6.2.: R-spectra show the modulation frequencies. *A:* R-spectra (worst ITD vs spontaneous) of 58 recording sites, ordered by the frequency at which they have their peak (limited to $0.1 - 4$ kHz). *B:* R-spectra shown in A, normalized. The +signs show the BF of each recording location. *C:* R-spectra (best ITD vs worst ITD) of 58 recording sites, ordered by the frequency at which they have their peak (limited to $0.1 - 4$ kHz). *D:* R-spectra shown in C, normalized. The +signs show the BF of each recording location. The black circles show the locations at which the noise was significantly modulated with the ITD (chapter 5). Note that the ordering of the recording locations is different between A–B and C–D.

were correlated ($r = 0.30$, $p = 0.018$). We also tested for the correlations between the input- and output-related R-spectra at each location. The correlation of the R-spectra were significant at $p < 0.05$ for 49 out of 58 recording locations, correlation coefficients ranging from $-0.58$ to 0.16. Only one of the correlation coefficients was positive. The negative correlation coefficient means that the output-related R-spectrum tended to increase at frequencies at which the input-related R-spectrum decreased. However, at the population level the frequency at which the main peak occurred for the input- and output-related R-spectra was not correlated ($r = 0.03$, $p = 0.8$), further indicating that the spectral changes that we had categorized as input- and output-related resulted from different processes in NL.

### 6.4.2. Suppression of the spontaneous spectra

Previously in this chapter, we used the spontaneous spectrum recorded after low-driving monaural stimulation far from the best frequency of each location as the reference spectrum of that recording location. This was done because the spontaneous activity after high-driving stimulation was suppressed. Now let us describe this suppression more closely for monaural stimulation at varying stimulus frequencies.

For intuition, we show raw spectra obtained from one recording location in response to a monaural stimulation at three stimulus frequencies (Fig. 6.3A–C). Favorable stimuli, such as monaural stimuli at the best frequency, elicited a high peak in the spectrum at the stimulus frequency (Fig. 6.3B). Far from the BF, the peak was not present (Fig. 6.3A, C). The magnitude of the peak is related to the mean activity of the neural sources (i.e. firing rate) underlying the neurophonic, as well as to the degree of sychronization of their activity. The peak can reach levels of 30 dB above the noise level and the height of the peak can be quantified by the cyclic mean signal (cyclic amplitude) of the response (Kuokkanen et al., 2010) (Figs. 6.1A and 6.3G).

The spectra, excluding the peak, had similar shapes independent of the stimulus frequency, but there was a clear increase in the magnitude of the noise spectrum for favorable stimulus frequencies. Furthermore, the spectrum of the spontaneous activity recorded directly after a favorable stimulus (gray, Fig. 6.3A–C) was suppressed in comparison to the spectrum of the spontaneous activity recorded after a non-favorable stimulus (red).

The magnitude of the noise spectrum alone is a poor measure to identify changes since for different recording locations, the average noise magnitudes span over several orders of magnitude (Kuokkanen et al., 2010). Thus, we used the R-spectra to quantify changes in the spectra. The R-spectra were calculated comparing the spectrum of the driven activity at each stimulus frequency to the reference spectrum to overcome the effects of the aforementioned suppression. In contrast to the results shown previously in this chapter, we did not average over the low activity and high activity groups. Instead, the R-spectrum was calculated separately for each stimulus frequency. The reference, however, was still defined as the weighted mean of the spontaneous spectra after non-favorable stimulation (see Methods).

For monaural stimulation, a typical R-spectrum of the driven activity vs. reference was flat across the spectral frequencies (Fig. 6.3D–F), with some peaks due to noisiness of both the reference and the driven spectra. However, there was a clear tuning of the average level of the R-spectrum across spectral frequencies, i.e., the mean R-spectum $\langle R \rangle$, with the stimulus frequency (Fig. 6.3D–F, red line). It was apparent from the $\langle R \rangle$-tuning curve across all stimulus frequencies (Fig. 6.3G, red line) that for non-favorable frequencies there was on average no difference between the driven and the spontaneous spectrum. Thus, for non-preferred stimuli mainly spontaneous activity was present in the neurophonic potential.

The suppression of the mean R-spectra of the spontaneous activity recorded after stimulation at the given frequency also showed a clear frequency tuning (Fig. 6.3G, gray line). The frequency tuning of the spontaneous mean R-spectra had a similar shape as the frequency tuning of the mean R-spectra (driven vs. reference) – the higher the activation the lower the spontaneous activity afterwards. At all recording locations the correlation of the two mean R-spectra was significant at $p < 0.05$; the correlation

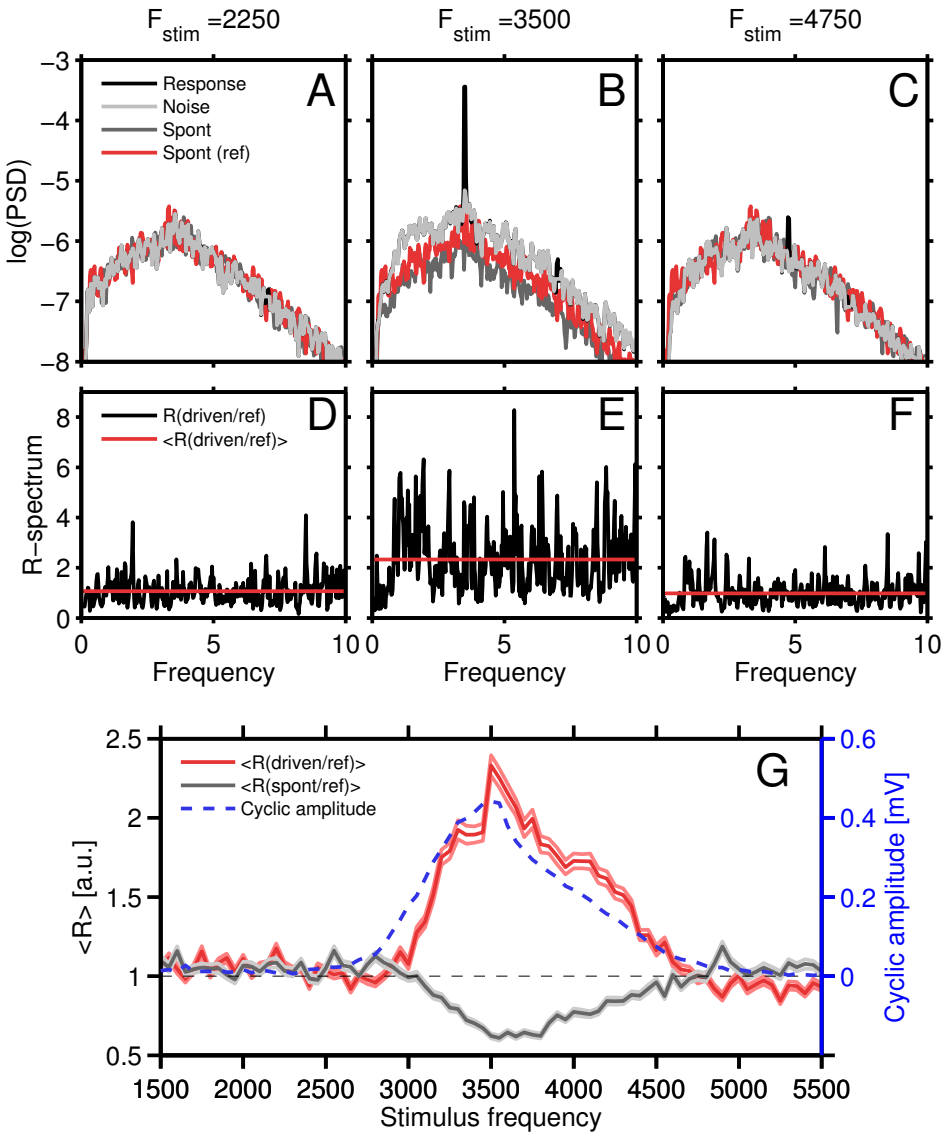


Figure 6.3.: The spontaneous activity is suppressed after high activation. *A–C:* PSDs of the driven *response* (black), the *noise* (light gray) separated from this response and the *spontaneous* activity (dark gray) after high-driving activity. The *spontaneous reference* spectrum recorded after low-driving stimulus is shown in red. *D–F:* R-spectra of the driven noise vs. the reference spontaneous spectra, as well as its mean R-spectrum (red line). *G:* Frequency tuning (red) of the mean R-spectrum of the driven noise vs. the reference spontaneous activity shown in *D–F*. The mean R-spectrum of the spontaneous activity vs. the reference spontaneous activity shows the suppression of the spontaneous activity after high-driving activity (gray). The light red and light gray lines show the standard error of mean for each stimulus frequency. The cyclic amplitude is shown in blue, dashed line. recording site: 122.05.4

coefficients ranged from $-0.53$ to $-0.98$ with a median of $-0.89$.

The R-spectrum was calculated from the noise, thus excluding the peak at the stimulus frequency. The frequency tuning of the peak, i.e., cyclic mean signal was similar, but not identical, to the frequency tuning of the mean R-spectrum (Fig. 6.3G, blue). The correlation of the frequency tunings of the mean R-spectum and cyclic mean signal was significant (at $p = 0.05$) for 49 out of 58 recording locations, and the significant correlation coefficients ranged from 0.33 to 0.97 (median 0.78). Furthermore, the suppression of the spontaneous R-spectra was not related to the cyclic mean amplitude – for binaural stimulation the suppression was independent of the ITD (Fig. 6.1B).

We conclude from our results for the suppression that when calculating the R-spectra, the choise of reference spectrum can change the R-spectra substantially.

## 6.5. Discussion

What are the main contributors to the observed noise PSDs? During the presentation of a monaural tone, NL neurons as well as NM neurons fire with high rate. During silence, NL neurons fire at a very low rate, but NM neurons have a high spontaneous firing rate. Because neuronal activities in NL can be well described by an inhomogeneous Poisson process, the shape of the noise PSD is determined by the spectra of the kernel functions associated with the sources, and the spectra of kernels of NL neuronal spikes and NM neuronal spikes might be different. Therefore, changing the ratio of the firing rates should change the shape of the resulting noise PSD of the neurophonic. The shape of the noise PSD during a tonal stimulus might therefore be different from the noise PSD during spontaneous activity.

We have shown that the average shape of the PSD does not change much from spontaneous to driven activity, or depending on ITD, apart from the peak at the stimulus frequency (see also chapter 5). More precisely, the spontaneous activity has a PSD that resembles in shape the driven activity, but the average level is lower. Given that the spectra of waveforms associated with NL and NM neuronal spikes are indeed different, our finding indicates that there is only one type of significant sources contributing to the neurophonic, related to the input to NL.

Here we found that the contributions from NL neurons influence the spectrum mainly at low frequencies $< 1$ kHz, considering those recording locations exhibiting a significant ITD tuning of the noise. The differences of the spectra between the spontaneous activity and the activity at the worst ITD, i.e. input-related differences, were at higher frequencies, mainly around $1 - 2$ kHz.

### 6.5.1. Contribution of the laminaris neurons

The variability in the extracellular contributions of the spiking of one or several NL neurons (6.2C–D) are in agreement with previous studies showing that depending on the relative positions of the recording electrode in respect to a neuron, there can be large variability in the extracellular spike waveform observed in the EFP, induced by the spike in that neuron (Gold et al., 2006; Lindén et al., 2010). The variability in these contributions might be further increased by a putative extracellular filtering (Bédard et al., 2004; 2006; 2010).

The changes of the spectrum around 500 Hz agree with the predictions made for currents from NL neurons in the high CF region (Slee et al., 2010). They are in disagreement with other studies stating that the synaptic currents affect the local field potential (low-pass filtered EFP) most (Mitzdorf, 1985; Logothetis and Wandell, 2004; Nunez and Srinivasan, 2006). Even though the intracellular shape of the spikes of the NL neurons might show fast time constants, i.e., a peak at higher frequencies than 500 Hz in their spectrum, a low-pass filtering might affect the extracellular shape of the spectrum. Such low-pass filtering could originate from the dendrites, from the capacitive cell membrane (Gold et al., 2006; Lindén et al., 2010) or from the putative back propagation of the spike from the axon initial segment to the soma (Ashida et al., 2007).

The origin of the notch at lowest frequencies (below 200 Hz), observed at many recording locations for the input-related R-spectra, is not clear. Nor is the origin of the peak at these frequencies observed in some in the output-related R-spectra. They might result in from processes, which are independent of the stimulus, contributing most to these frequencies. The band-pass filtering ($100 - 10000$ Hz) used in the recordings migth also affect these low frequencies. Furthermore, there might be an influence from the GABAergic inhibition to NL, since GABAergic currents observed in chick NM and NL (Funabiki et al., 1998; Monsivais et al., 2000) are much slower than the faster currents related to the NL spikes or NM spikes (Carr and Konishi, 1990; Köppl, 1997a; Funabiki and Konishi, 2005; Ashida et al., 2007; Funabiki et al., 2011).

### 6.5.2. Contribution of the magnocellular neurons

Our hypothesis is that the spontaneous neurophonic is mainly induced by the axonal activity of the NM axons, because the spontaneous (mean population) activity in NM is $\approx 200$ Hz (Köppl, 1997a) but in NL only around 50 Hz (Carr and Konishi, 1990; Viete et al., 1997). Moreover, we have previously shown that the form of the PSD can be approximated with the spectrum of the spike waveforms contributing to the neurophonic potential (Kuokkanen et al., 2010). Since the form of the PSD does not change much from spontaneous to driven activity, we take this as an indication that the both spotnaneous and driven activity have common underlying sources.

The above hypothesis implies that the frequency tuning of the mean R-spectrum (Fig. 6.3G) reflects the frequency tuning of the population firing rate of the NM neurons (see also appendix A.2). This tuning can be considerably different from the tuning of the cyclic mean signal or the variance of the response (chapters 4 and 5). The difference in the frequency tunings between the 'noise' and the 'signal', even though both would originate from the activity of the NM neurons, can for example result from the frequency tuning of the phase-locking of the NM neurons (Köppl, 1997b). The phase locking, apart from the firing rate, also highly influences the signal peak (see also the chapter 4).

### 6.5.3. Shape of the spectrum

The auditory nerve (AN) fibers have been shown to exhibit spontaneously preferred interspike intervals corresponding to about the best frequency up to 5 kHz CFs (Manley, 1979; Köppl, 1997a). The strong synapses from AN to NM (Köppl, 1994) probably subsequently bias the spontaneous activity in NM neurons towards the same frequency. It is unclear whether the NL neurons show the same bias towards preferred frequencies in their spontaneous activity. The peak we observed in the spontaneous, as well as some driven spectra around the CF up to 5 kHz but rarely above, fits together with the hypothesis that the input to NL (the NM neurons' activity) is the origin of the neurophonic.

A $1/f$ -scaling of the extracellular noise has been reported in many previous studies (Novikov et al., 1997; Freeman et al., 2000; Bédard et al., 2006; Bédard and Destexhe, 2009). The 'noise' spectra we present here are not comparable with those studies, because here its form has been proposed to reflect mainly or solely the spike waveform of the sources (Kuokkanen et al., 2010). In contrast, the $1/f$ -noise has been hypothesized to originate from the ionic diffusion for EFPs in which not most of the extracellular current is due to electric-field effects (Bédard and Destexhe, 2009). That these noises are not comparable is supported by our results showing a strong overall increase at all frequencies with increased activity level, such as resulting from stimulation at best frequency. Only a few frequency bands showed an exception of this general up-scaling.

It is possible that also in our data there is an underlying $1/f$ noise. However, to identify the spectrum of the underlying 'real' noise which is not related to the neuronal processing of ITD detection, much more data is needed, and novel analyzing methods to exclude contributions from both NM and NL neurons. Similar, or even flatter spectral shapes than reported here have been observed in auditory brainstem of other animals in response to sustained stimulus at one frequency (Mc Laughlin et al.,

2010a). The spectrum of the neurophonic in the owl NL also changes considerably with stimulus, as has been shown for click stimulation (Wagner et al., 2009). The spectral form in response to clicks and probably to onsets of the tones reflect the fact that the neurophonic at onsets might result from different mechanisms than those shown here. For example, the firing rate and synchrony of the NL neurons might be very different at onsets than during sustained responses. Thus, the conclusions made here might not apply to responses to transient stimuli.

### 6.5.4. Conclusions

We found that the contributions to the spectra of the neurophonic can be separated to ones originating from the input to NL and to others originating from the output of NL. The output, i.e., NL neurons' spiking influenced the spectra to a small extent, mainly at low frequencies ($< 1$ kHz). In contrast, the input to NL, i.e., the NM axonal spikes and the synaptic input to NL neurons, affected the spectra to a greater extent and at all frequencies. We were able to link the increase of the spectra at all frequencies to the mean population firing rate of the NM neurons. Furthermore, for the input to NL there were also two broad peaks around $1 - 2$ kHz and $3 - 4$ kHz. Moreover, we found that the more a spectrum, i.e., the mean population firing rate of the NM neurons, was increased by the stimulation, the more the spontaneous activity recorded immediately afterwards was suppressed. Finally, we found that the spontaneous spectra showed a peak at frequencies around BF, implying spontaneous locking to this frequency band. However, all these results are preliminary because of the small data set available for the analysis.

# 7. Discussion

## 7.1. Summary of the Results

The neurophonic potential in the nucleus laminaris (NL) of the barn owl results from the population activity of hundreds of neural sources (chapter 4). We have also shown that these sources are likely to represent the input to NL, i.e. the activity in the axons projecting to NL from nucleus magnocellularis (NM), because the number of the neurons in NL as well as the amplitude of their extracellular spikes are not alone sufficient to sum up to such a strong neurophonic as observed. Typically an EFP reflects the computations and output of a local cell assembly, whereas the neurophonic in NL reflects the inputs to the area. Consistently with observations in other EFPs, the spatial extent of the neurophonic seems to be rather small and most of the currents recorded with an electrode originate from a volume with a radius of about 300 $\mu$m around the electrode. However, we also introduced the possibility that coherent signals from dipole-like sources (such as those representing the output from NL) could sum up in the extracellular space and increase the potential in the electrode even though the sources would be far away and thus have a very small amplitude as arriving to the electrode. Similar summation of coherent activity over large distances have been lately suggested by Lindén et al. (2011).

The statistics of the neurophonic responses to monaural stimulation sum up linearly to predict the neurophonic in response to binaural stimulation with high accuracy (chapter 5). This is consistent with the hypothesis that the neurophonic is a summation of the currents from sources conveying the input to NL. Non-linearities that could reflect active processes of the NL neurons were only detected in few recordings of the neurophonic. Thus, if the NL neurons do contribute to the neurophonic, they have a minor role in its generation. Such a predictability of EFPs in response to one stimulation, from the responses to other stimuli has not been reported before to our knowledge.

Analysis of the spectra of the neurophonic responses (chapter 6) showed that the minor contributions from the NL neurons can be detected mainly at low frequencies ($< 1$ kHz). The majority of the changes in the spectrum from spontaneous to driven activity are broadband and probably correspond to the extracellular spike wave form of the NM axonal spikes or the synaptic input currents to NL dendrites. However, the morphology of the NL neurons' dendritic tree suggests that the synaptic currents might largely cancel out in the extracellular space.

Our results show that the neurophonic in the owl NL is different from EFPs in general, which arise mainly from synaptic currents (corresponding extracellularly to local field potentials) and from 'output' spikes (corresponding extracellularly to multi-unit activity). In agreement to previous studies we found that the morphology of a neural structure plays a crucial role in the relationship of the neuronal activity and the field potential.

Additionally, the neurophonic potential in the owl studied in this thesis is different from the neurophonic potentials as reported previously in chick and in mammals. There, the neurophonic is thought to originate mainly from from the output spikes of the bipolar layer of neurons and from the synaptic currents. The difference to other neurophonic potentials is not surprising, though. There are large physiological differences between the owl and the other species both at single cell level and at the level of network structure in the circuit performing the ITD detection. Thus, the source of the neurophonic can also differ between species, as shown in this thesis. Furthermore, some of the results presented in this thesis cannot be generalized to other species but rather highlight their difference to the owl.

## 7.2. Outlook

Refined computational studies may help to further understand the neurophonic. Useful may be mechanistic models of spike waveforms and their distance-dependence as outlined in Gold et al. (2006), models of the activity of NM and NL neurons (especially at onsets), and models of synapses including probabilistic release of vesicles and short-term plasticity. Extended numerical simulations could also evaluate combinations of different types of sources.

Further experimental work is also required. For example, high-resolution spectra obtained from longer recordings for various sound intensities and binaural input would further indicate the nature of sources if the associated spike waveforms have different shapes; the spectra obtained from our data were rather noisy. Furthermore, mapping studies (with a fine spatial resolution of recording sites when advancing the electrode through NL) would provide valuable insights on the recording radius of an electrode and answer the following questions. Does the neurophonic critically depend on the distance to an NL neuron, i.e., are there narrow spatially local extrema in the neurophonic response characteristics, such as its variance, cyclic-mean amplitude and/or the SNR, pointing to local contribution of synapses and NL neurons to the LFP? Or are these characteristics smoothly varying with depth, pointing to a spatially wider distribution of sources? What is the length constant of the decay of theses measures outside NL? What is the synchrony radius in medio-lateral and antero-posterior extensions of NL? Finally, an extended analysis of the neurophonic at the onset of tones and a comparison to the unit activity at onsets could deepen our understanding.

Another line of research to further clarify the origin of the neurophonic is drug application into NL. For example, pressure injection of GABA in NL in vivo reduced responses, which supports the role of NL spikes as the origin of the neurophonic (Takahashi and Konishi, 2002). However, analogue waveforms were not analyzed in this study. To avoid possible artifacts due to pressure injection, drugs might ideally be applied iontophoretically. In addition to GABA, also AMPA- and NMDA-receptor antagonists could be applied to separate contributions of axons from contributions of the NL cell bodies. In vitro approaches can also contribute to understanding the neurophonic in NL (Lautemann et al., 2008).

# A. Mathematical Appendix

## A.1. Calculation of the power spectral density of the noise

In this section, I approximate the power spectral density (PSD) of an inhomogeneous Poisson process. There are $N$ independent generators of the Poisson process, each with the same periodic firing rate $\lambda(t)$ with a period $1/f_{\text{stim}}$ and a mean rate $\langle\lambda\rangle$. The duration of the spike train is $T$, and the spike times are given by $\delta$-functions. The spike train including spike times from all sources is then convolved with a spike wave form $k(t)$ to achieve a continuous voltage trace. Such a process has been described also in section 4.3.4. In particular, I calculate the PSD not for the 'signal' at the stimulus freqyency $f_{\text{stim}}$ (see Eq. 4.10) but for the 'noise' at any other frequencies $f$ than the stimulus frequency $f_{\text{stim}}$.

The power spectral density $P$ of an inhomogeneous Poisson spike train is (Hohn and Burkitt, 2001):

$$P_T(\omega) = \frac{1}{T}\left|\int_0^T \langle R(t,\epsilon)\rangle e^{-j\omega\epsilon}\,\mathrm{d}\epsilon\right| \quad , \tag{A.1}$$

where $\langle R(t,\epsilon)\rangle = \langle\lambda(t)\lambda(t+\epsilon)+\lambda(t)\delta(\epsilon)\rangle$ is the autocorrelation function of the Poisson process (Papoulis and Pillai, 2002), and $T$ is the finite duration of the spike train. In the power spectral density $P_T(\omega)$ of the aforementioned inhomogeneous Poisson process, there are two prominent features, 1) at frequency $f_{\text{stim}}$ and at its higher harmonics there are peaks in the spectrum, and 2) at all other frequencies the spectrum is flat and has the intensity $\langle\lambda\rangle$ (Hohn and Burkitt, 2001). Now for $N$ sources with the mean firing rate $\langle\lambda\rangle$ the PSD at the frequency $f \neq n \cdot f_{\text{stim}}$ is then

$$P_T(f) = N\langle\lambda\rangle \quad . \tag{A.2}$$

Analyzing the Fourier transform of the convolution of two functions $x(t)$ and $y(t)$, it is very useful to notice that it is equivalent to the multiplication of their Fourier transforms $\tilde{x}(\omega)$ and $\tilde{y}(\omega)$:

$$\mathscr{F}\{x(t) * y(t)\} = \tilde{x}(\omega)\tilde{y}(\omega) \quad . \tag{A.3}$$

Thus, the PSD of a Poisson spike train convolved with the spike wave form $k(t)$ at $f \neq f_{\text{stim}}$:

$$P_{\text{n}}(f) = N\langle\lambda\rangle|\tilde{k}(f)|^2 \tag{A.4}$$

where $\tilde{k}(\omega)$ is the Fourier transform of $k(t)$ and $|\tilde{k}(f)|$ is its absolute value at the frequency $f$. The Fourier transform is then squared to get the PSD.

## A.2. Power spectral density, R-spectrum and variance of the noise

R-spectrum is defined as

$$R(f) = \frac{P_{\text{n, driven}}(f)}{P_{\text{spont}}(f)} \ . \tag{A.5}$$

For the PSDs of the noise and of the reference (spontaneous) noise, as defined in section A.1, the mean R-spectrum is

$$\begin{aligned} \langle R(f) \rangle &= \frac{1}{F} \int_0^F \frac{P_{\text{n, driven}}(f)}{P_{\text{spont}}(f)} \, \mathrm{d}f \\ &= \frac{1}{F} \int_0^F \frac{N\lambda_{\text{driven}} |\tilde{k}_{\text{driven}}(f)|^2}{N\lambda_{\text{spont}} |\tilde{k}_{\text{spont}}(f)|^2} \, \mathrm{d}f \\ &= \frac{1}{F} \frac{\lambda_{\text{driven}}}{\lambda_{\text{spont}}} \int_0^F \frac{|\tilde{k}_{\text{driven}}(f)|^2}{|\tilde{k}_{\text{spont}}(f)|^2} \, \mathrm{d}f \quad , \end{aligned} \tag{A.6}$$

where $N$ is the number of independent sources, $\lambda_{\text{driven}}$ is the driven firing rate, $|\mathscr{F}\{k_{\text{driven}}(t)\}| = |\tilde{k}_{\text{driven}}(f)|$ is the absolute value of the Fourier transfrom of the spike kernel, $|\tilde{k}_{\text{spont}}(f)|$ is the absolute value of the Fourier transfrom of the reference kernel and $\lambda_{\text{spont}}$ is the reference firing rate.

If $|\tilde{k}_{\text{driven}}(f)|^2 = |\tilde{k}_{\text{spont}}(f)|^2$, i.e., the shape of the spectrum does not change between spontaneous activity and diven activity, then the mean R-spectrum is the ratio of the driven and spontaneous population firing rates

$$\langle R(f) \rangle = \frac{\lambda_{\text{driven}}}{\lambda_{\text{spont}}} \quad . \tag{A.7}$$

On the other hand, the variance of the noise $n(t)$ in a response trace is defined as

$$\sigma_n^2 = \frac{1}{T} \int_0^T n^2(t) \, \mathrm{d}t \tag{A.8}$$

According to Parseval's identity

$$\int_{-\infty}^{\infty} |g(t)|^2 \, \mathrm{d}t = \int_{-\infty}^{\infty} |\mathscr{F}\{(g)\}|^2 \, \mathrm{d}f \quad . \tag{A.9}$$

Since the noise of a response $n(t) \subset \mathbb{R}$ is defined for $t \in [0, T]$, we get

$$\int_0^T n^2(t) \, \mathrm{d}t = \int_{-\infty}^{\infty} |\mathscr{F}\{n(f)\}|^2 \, \mathrm{d}f$$

and thus, because the power spectral density of the noise is $|\mathscr{F}\{n(f)\}|^2 = N\lambda|\tilde{k}(f)|^2$ (Eq. A.4), the variance of the noise $\sigma_{\text{n}}^2$ can be expressed in terms of the Fourier transfor of the noise

$$\begin{aligned} \sigma_{\text{n}}^2 = \frac{1}{T} \int_0^T n^2(t) \, \mathrm{d}t = \frac{1}{T} \int_{-\infty}^{\infty} |\mathscr{F}n(f)|^2 \, \mathrm{d}f = \frac{N \, \lambda}{T} \int_{-\infty}^{\infty} |\tilde{k}(f)|^2 \, \mathrm{d}f \\ = \frac{N \, \lambda}{T} \int_0^F |\tilde{k}(f)|^2 \, \mathrm{d}f \end{aligned} \tag{A.10}$$

where $|\tilde{k}(f)|^2$ is defined for $f \in [0, F]$ and zero for $f > F$.

Now the ratio of the variances of the driven noise and the reference (spontaneous) noise is

$$\frac{\sigma_{\mathrm{n}}^2}{\sigma_{\mathrm{spont}}^2} = \frac{\lambda_{\mathrm{driven}}}{\lambda_{\mathrm{spont}}} \frac{\int_0^F |\tilde{k}\mathrm{driven}(f)|^2 \, \mathrm{d}f}{\int_0^F |\tilde{k}_{\mathrm{spont}}(f)|^2 \, \mathrm{d}f} \quad . \tag{A.11}$$

Thus, assuming again that $|\tilde{k}_{\mathrm{driven}}(f)|^2 = |\tilde{k}_{\mathrm{spont}}(f)|^2$, the mean R-spectrum is closely related to the variance of the noise in the response:

$$\langle R(f) \rangle = \frac{\sigma_{\mathrm{n}}^2}{\sigma_{\mathrm{spont}}^2} \quad . \tag{A.12}$$

# B. Neurophonic Recordings in the NL of the Barn Owl

I introduce in this chapter the details of the recording setting of the physiological data[1] analyzed in the chapters 4–6.

## B.1. Experimental paradigm

Six barn owls (Tyto alba pratincola) were used to collect the physiological data presented in this study. The anatomical data in Figure 4.8 are re-analyses from data published earlier (Carr and Boudreau, 1993a;b) and from 6 additional owls used in parallel studies (Carr et al., 2010). The procedures described here conform to National Institute of Health guidelines for animal research and were approved by the Animal Care and Use Committee of the University of Maryland. Most animals were used in two or three separate physiology experiments, spaced approximately a week apart.

Anesthesia was induced by injections of ketamine hydrochloride (3 mg/kg i.m., Ketavet, Phoenix, St. Joseph, MO) and xylazine (2 mg/kg i.m., Xyla-ject, Phoenix). Supplementary doses of ketamine and xylazine were administered to maintain a suitable plane of anesthesia. Body temperature was measured with a cloacal probe inserted and maintained at 39°C by a feedback-controlled heating blanket (Harvard Instruments, Braintree, MA). Buprenorphine hydrochloride (0.3 mg/kg i.m., Buprenex, Reckitt and Colman Products, Richmond, VA) was administered at the end of each recovery experiment.

### B.1.1. Surgery and stereotaxis

Initially, the owl's head was placed in a custom-designed stereotaxic frame, and stabilized using ear bars and a beak holder. Then a metal headplate and a short metal pin marking a standardized zero point were permanently glued to the skull. After this, the ear bars and the beak holder were removed, and the head held by the headplate alone. An opening was made in the skull around the desired area relative to the zero point, and the dura was cut open. Each electrode was moved in defined amounts in the rostrocaudal and mediolateral axes before being driven down into the brain. In some cases, the electrode was angled to facilitate access to extremely medial or lateral regions of the brainstem.

### B.1.2. Electrodes and recording setup

Owls were placed on a vibration-isolated table within a sound-attenuating chamber (IAC, New York, NY). Commercial Epoxylite-coated tungsten electrodes (Frederick Haer) were used, with impedances between 2 and 20 MΩ. A silver chloride pellet, placed under the animal's skin around the incision, served as the reference electrode (WPI, Sarasota, FL). Electrode signals were amplified and band-pass filtered ($100 - 13000$ Hz) by a custom-built headstage and amplifier. The noise floor of the equipment was in the range of $1 - 10$ $\mu$V. The recording was then passed in parallel to an oscilloscope, a threshold discriminator [SD1, Tucker-Davis Technologies (TDT), Gainesville, FL] and an A/D converter (DD1, TDT) connected to a personal computer via an optical interface (OI, TDT). A continuously refreshed, software-generated

[1] The data was recorded $2001 - 2010$ by C. E. Carr, H. Wagner and G. Ashida in the laboralories of C. E. Carr in the University of Maryland, MD and H. Wagner in RWTH Aachen, Germany

display of the waveforms that triggered TTL pulses aided in trigger judgment. Analogue waveforms were saved for off-line analysis.

## B.2. Stimulation

### B.2.1. Stimulus generation and calibration

Acoustic stimuli were digitally generated using custom-made software (Xdphys, developed in Dr. M. Konishi's lab at California Institute of Technology, Pasadena, CA) driving a signal-processing board [DSP2, Tucker-Davis Technologies (TDT), Gainesville, FL]. After passing a D/A converter (DD1, TDT) and an anti-aliasing filter (FT6-2, corner frequency: 20 kHz, TDT), the signals were variably attenuated (PA4, TDT), impedance-matched (HB6, TDT), and attenuated by an additional fixed amount before being fed to commercial miniature earphones. Two separate signals could be generated, passing through separate channels of associated hardware and driving two separate earphones. Sounds were calibrated individually at the start of each experiment, using built-in miniature microphones (Knowles EM3068, Ithasca, IL). In all experiments, voltage responses were recorded with a sampling frequency of 48077 Hz, and saved for off-line analysis.

### B.2.2. Stimulation protocoll and recording

While lowering an electrode in the brain towards NL, noise bursts were presented as search stimuli. Once auditory responses were discernible, tonal stimuli were applied from both the ipsi- and the contralateral side in order to measure best frequency and best ITD, and to estimate the position of the electrode.

To record a the neurophonic, tone bursts of different frequencies (500 Hz−10 kHz) were presented monaurally. Tone bursts were repeated 3 to 5 times. The duration of a tone burst was 100 ms with 5-ms rise/fall times and a constant starting phase. In total, 200 ms of the response were saved per trial (single trial data shown in Fig. 4.1 A). The stimulus began 5 ms after the recording started and ended at 105 ms. The level of the tones was generally $20 - 30$ dB above threshold. The inter-stimulus interval was either 500 ms or 700 ms.

The frequency-tuning curves were recorded in response to both monaural and binaural stimulation. For each recording location, an appropriate stimulus frequency near the location's best frequency was selected to record the ITD tuning in the range of $-300$ to 300 $\mu$s with 30 $\mu$s step size.

### B.2.3. Recording locations

Data were recorded from 171 locations in the NL of 6 anesthetized barn owls. We acquired data in one to three recording sessions in each owl, and in each session from only one of the NLs. There were one to seven penetrations in each session, and each penetration contained one to 28 dorso-ventrally distributed recording locations. In a single penetration, the distance between the recording locations was generally equal to or more than 100 $\mu$m (approx. 2/3 of the locations). In four penetrations we used distances of 10 or 15 $\mu$m.

#### Dataset 1

Both ipsi- and contralateral ear were stimulated for almost all locations, sometimes repeatedly. In the chapter 4, one "recording site" means a recording of the response to monaural stimulation. We analyzed 378 recording sites altogether.

### Data set 2

At 91 locations (out of 171), responses to ipsi- and contralateral stimulation with different frequencies, as well as binaural stimulation approximately at best frequency with varying ITDs were recorded and analyzed. In the chapters 5 and 6, one "recording site" refers to one location.

## B.3. Anatomical analyses

Golgi data and the plastic sections through NL were published in Carr and Boudreau (1993a) and reanalyzed for this study, e.g. to correct for the shrinkage of the tissue.

For GABA immunohistochemistry, two owls were anesthetized by i.m. injection of pentobarbital sodium/phenytoin sodium (Euthasol Euthanasia Solution, Delmarva Laboratories, Inc., Virginia) at a dose of 7 mg/kg. Once deeply anesthetized, the owls were perfused transcardially with 0.9% saline, followed by 0.1 M phosphate buffer, 4% paraformaldehyde, and 0.25% glutaraldehyde. For one case, processed by D. LaRue and J. Winer (Winer and Larue, 1996), 50 $\mu$m vibratome sections were placed in 10% normal goat blocking serum (NGS) for 1 hr and incubated overnight in rabbit- anti-GABA (INCstar; Stillwater, MN) diluted 1:5000 or in rabbit-anti-GABA (R.J. Wenthold, National Institutes of Health, Bethesda, MD) diluted 1:2000 in 0.01 M phosphate- buffered saline with 2% NGS. The immunoperoxidase procedure was avidin-biotin (Vector Laboratories; Burlingame, CA) with diaminobenzidine as the chromagen. In the second owl, 40 $\mu$m frozen sections were incubated with antiserum against GABA (Sigma, St Louis, MO) diluted 1:2000 for two days at 4°C. The immunoperoxidase procedure was as above.

The dorsal brainstem was reconstructed to determine the size and volume of NL. For normal light microscopy, 3 barn owls were anesthetized and perfused as above, then the brainstems were sectioned on a freezing microtome at 40 $\mu$m thickness. Two brains were cut in the coronal plane, and one in the horizontal plane. Sections were collected in order in phosphate buffer, mounted, Nissl stained and coverslipped. Every third section was traced on a computer connected to a microscope. We used an Olympus BX-60 microscope equipped with a motorized stage drive (LEP Mac 5000), and coupled to a PC containing the Neurolucida software (Microbrightfield Inc., Colchester, VT) through the Lucivid system for morphometry, or through a digital camera (DVC, Austin, TX) for photomicrograph acquisition. Cytoarchitectonic boundaries were determined in Nissl stained sections and reconciled for 10% shrinkage, determined by comparing with Araldite embedded sections. The dorso-ventral depth of the central region of the nucleus laminaris was measured from both frozen sections ($635 \pm 36$ $\mu$m, 15 sections, 3 owls) and from Araldite embedded sections ($634 \pm 38$ $\mu$m, 15 sections, 2 owls). The nucleus laminaris is about 100 $\mu$m thicker rostrally, and about 100 $\mu$m thinner caudally, and sections throughout the rostrocaudal extent of NL had a mean depth of $639 \pm 184$ $\mu$m (26 sections, 1 owl). With 10% shrinkage, this produces an estimated depth of 705 $\mu$m, consistent with physiological measurements (Carr and Konishi, 1990).

Axon and neuron density were measured in NL, using osmium treated araldite embedded material stained with Toluidine blue and prepared for Carr and Boudreau (1993a). All brains were sectioned in the transverse plane, orthogonal to the major axis of the brainstem (Carr and Konishi, 1990; Carr and Boudreau, 1993a). Some of the prepared 200 $\mu$m plastic sections were re-sectioned orthogonal to the delay line axons i.e. orthogonal to the transverse section plane and also parallel to the dorsal and ventral borders of the NL, in order to generate the most accurate estimate of maximum axon density. In order to measure axon diameters in and around the NL, a detailed morphometric analysis was performed. Axon diameters were measured from myelinated profiles cut in cross section, while the mean Feret's diameter was used for fibers cut on a tangent. Feret's diameter takes the value of the distance measured across minimum and maximum tangents across a particle and avoids choosing between maximum and minimum diameters. Images of NL axons were captured at 2000x (Neurolucida), then analyzed using interactive profile recognition. All measurements were corrected for 10% tissue shrinkage for aldehyde fixation and plastic embedding (Kushida, 1962).

# Bibliography


R. Adolphs. Bilateral inhibition generates neuronal responses tuned to interaural level differences in the auditory brainstem of the barn owl. *J Neurosci*, 13(9):3647–68, 1993.

J. P. Agapiou and D. McAlpine. Low-frequency envelope sensitivity produces asymmetric binaural tuning curves. *J Neurophysiol*, 100(4):2381–2396, 2008.

J. Arezzo, H. G. Vaughan, and B. Koss. Relationship of neuronal activity to gross movement-related potentials in monkey pre- and postcentral cortex. *Brain Res*, 132(2):362–9, 1977.

B. J. Arthur. *Neural Computations Leading to Space-specific Auditory Responses in the Barn Owl*. PhD thesis, California Institute of Technology, 2002.

B. J. Arthur. Sensitivity to spectral interaural intensity difference cues in space-specific neurons of the barn owl. *J Comp Physiol A*, 190(2):91–104, 2004.

G. Ashida, K. Abe, K. Funabiki, and M. Konishi. Passive soma facilitates submillisecond coincidence detection in the owl's auditory system. *Journal of Neurophysiology*, 97(3):2267–82, 2007.

S. Bahar, A. Neiman, L. A. Wilkens, and F. Moss. Phase synchronization and stochastic resonance effects in the crayfish caudal photoreceptor. *Phys Rev E*, 65:050901, 2002.

A. D. S. Bala, M. W. Spitzer, and T. T. Takahashi. Prediction of auditory spatial acuity from neural images on the owl's auditory space map. *Nature*, 424(6950):771–4, Aug. 2003.

M. S. Bartlett. *An introduction to stochastic processes, with special reference to methods and applications*. Cambridge University Press, Cambridge, UK, 3rd edition, 1978.

R. Batra, S. Kuwada, and D. C. Fitzpatrick. Sensitivity to interaural temporal disparities of low- and high-frequency neurons in the superior olivary complex. ii. coincidence detection. *J Neurophysiol*, 78 (3):1237–47, 1997.

C. Bédard and A. Destexhe. Macroscopic models of local field potentials and the apparent 1/f noise in brain activity. *Biophys J*, 96(7):2589–2603, 2009.

C. Bédard, H. Kröger, and A. Destexhe. Modeling extracellular field potentials and the frequency-filtering properties of extracellular space. *Biophys J*, 86(3):1829–42, 2004.

C. Bédard, H. Kröger, and A. Destexhe. Does the 1/f frequency scaling of brain signals reflect self-organized critical states? *Phys Rev Lett*, 97(11):118102–118102, 2006.

C. Bédard, S. Rodrigues, N. Roy, D. Contreras, and A. Destexhe. Evidence for frequency-dependent extracellular impedance from the transfer function between extracellular and intracellular potentials. *J Comput Neurosci*, pages 1–15, 2010.

P. Berens. Circstat: A matlab toolbox for circular statistics. *Journal of Statistical Software*, 31(10): 1–21, 9 2009.

P. Berens, G. A. Keliris, A. S. Ecker, N. K. Logothetis, and A. S. Tolias. Feature selectivity of the gamma-band of the local field potential in primate primary visual cortex. *Front Neurosci*, 2(2): 199–207, 2008.

J. Blauert. *Spatial hearing: the psychophysics of human sound localization.* MIT Press, Cambridge, Massachusetts, 1997.

T. Bojanowski, K. Hu, and D. W. Schwarz. Analogue signal representation in the medial superior olive of the cat. *The Journal of otolaryngology*, 18(1):3–9, 1989.

A. Borst and F. E. Theunissen. Information theory and neural coding. *Nat. Neurosci.*, 2(11):947–957, 1999.

J. C. Boudreau. Neural volleying: upper frequency limits detectable in the auditory system. *Nature*, 208 (5016):1237–8, 1965.

A. Brand, O. Behrend, T. Marquardt, D. McAlpine, and B. Grothe. Precise inhibition is essential for microsecond interaural time difference coding. *Nature*, 417(6888):543–7, May 2002.

J. R. Brawer and D. K. Morest. Relations between auditory nerve endings and cell types in the cat's anteroventral cochlear nucleus seen with the golgi method and nomarski optics. *J Comp Neurol*, 160 (4):491–506, 1975.

P. Bremen, I. Poganiatz, M. von Campenhausen, and H. Wagner. Sensitivity to interaural time difference and representation of azimuth in central nucleus of inferior colliculus in the barn owl. *J Comp Physiol A Neuroethol Sens Neural Behav Physiol*, 193(1):99–112, 2007.

H. M. Brew and I. D. Forsythe. Two voltage-dependent k+ conductances with complementary functions in postsynaptic integration at a central auditory synapse. *J Neurosci*, 15(12):8011–8022, 1995.

S. Brückner and R. L. Hyson. Effect of gaba on the processing of interaural time differences in nucleus laminaris neurons in the chick. *Eur J Neurosci*, 10(11):3438–50, 1998.

J. S. Buchwald, E. S. Halas, and S. Schramm. Progressive changes in efferent unit responses to repeated cutaneous stimulation in spinal cats. *J Neurophysiol*, 28:200–15, 1965.

R. M. Burger, K. S. Cramer, J. D. Pfeiffer, and E. W. Rubel. Avian superior olivary nucleus provides divergent inhibitory input to parallel auditory pathways. *J Comp Neurol*, 481(1):6–18, 2005.

S. P. Burns, D. Xing, and R. M. Shapley. Comparisons of the dynamics of local field potential and multiunit activity signals in macaque visual cortex. *Journal of Neuroscience*, 30(41):13739–13749, 2010a.

S. P. Burns, D. Xing, M. J. Shelley, and R. M. Shapley. Searching for autocoherence in the cortical network with a time-frequency analysis of the local field potential. *Journal of Neuroscience*, 30(11): 4033–4047, 2010b.

G. Buzsáki. Theta oscillations in the hippocampus. *Neuron*, 33(3):325–40, 2002.

G. Buzsáki and A. Draguhn. Neuronal oscillations in cortical networks. *Science*, 304(5679):1926–9, June 2004.

L. H. Carney and T. C. Yin. Responses of low-frequency cells in the inferior colliculus to interaural time differences of clicks: excitatory and inhibitory components. *J Neurophysiol*, 62(1):144–61, 1989.

C. E. Carr. Time coding in electric fish and barn owls. *Brain Behav Evol*, 28(1–3):122–33, 1986.

C. E. Carr. Processing of temporal information in the brain. *Annu Rev Neurosci*, 16:223–43, 1993.

C. E. Carr and R. E. Boudreau. Central projections of auditory nerve fibers in the barn owl. *J Comp Neurol*, 314(2):306–18, Dec. 1991.

C. E. Carr and R. E. Boudreau. Organization of the nucleus magnocellularis and the nucleus laminaris in the barn owl: encoding and measuring interaural time differences. *J Comp Neurol*, 334(3):337–55, Aug 1993a.

C. E. Carr and R. E. Boudreau. An axon with a myelinated initial segment in the bird auditory system. *Brain Res*, 628(1–2):330–4, Nov. 1993b.

C. E. Carr and M. Konishi. Axonal delay lines for time measurement in the owl's brainstem. *Proc Natl Acad Sci USA*, 85(21):8311–5, 1988.

C. E. Carr and M. Konishi. A circuit for detection of interaural time differences in the brain stem of the barn owl. *J Neurosci*, 10(10):3227–46, Oct. 1990.

C. E. Carr and C. Köppl. Coding interaural time differences at low best frequencies in the barn owl. *J Physiol Paris*, 98(1–3):99–112, 2004.

C. E. Carr, I. Fujita, and M. Konishi. Distribution of GABAergic neurons and terminals in the auditory system of the barn owl. *J Comp Neurol*, 286(2):190–207, Aug. 1989.

C. E. Carr, G. Ashida, S. Shah, S. Brill, P. T. Kuokkanen, R. Kempter, and H. Wagner. Neurophonic maps of ITD in nucleus laminaris of the barn owl. In *Proceedings*, volume 40, page 480.18. Soc Neurosci Abstr, 2010.

S.-M. Cheng and C. E. Carr. Functional delay of myelination of auditory delay lines in the nucleus laminaris of the barn owl. *Dev Neurobiol*, 67(14):1957–74, Dec. 2007.

G. B. Christianson and J. L. Peña. Noise reduction of coincidence detector output by the inferior colliculus of the barn owl. *J Neurosci*, 26(22):5948–54, May 2006.

G. B. Christianson and J. L. Peña. Preservation of spectrotemporal tuning between the nucleus laminaris and the inferior colliculus of the barn owl. *J Neurophysiol*, 97(5):3544–53, May 2007.

Y. E. Cohen and E. I. Knudsen. Maps versus clusters: different representations of auditory space in the midbrain and forebrain. *Trends in Neurosciences*, 22(3):128–35, 1999.

W. L. Coleman, M. J. Fischl, S. R. Weimann, and R. M. Burger. Gabaergic and glycinergic inhibition modulate monaural auditory response properties in the avian superior olivary nucleus. *J Neurophysiol*, 105(5):2405–20, 2011.

R. B. Coles and A. Guppy. Directional hearing in the barn owl (Tyto alba). *J Comp Physiol A*, 163(1): 117–33, 1988.

J. W. Conlee and T. N. Parks. Origin of ascending auditory projections to the nucleus mesencephalicus lateralis pars dorsalis in the chicken. *Brain Research*, 367(1–2):96–113, 1986.

V. K. Dasika, J. A. White, L. H. Carney, and H. S. Colburn. Effects of inhibitory feedback in a network model of avian brain stem. *J Neurophysiol*, 94(1):400–14, 2005.

P. Dayan and L. F. Abbott. *Theoretical Neuroscience*. MIT Press, Cambridge, Massachusetts, 2001.

M. Deger, M. Helias, S. Cardanobile, F. M. Atay, and S. Rotter. Nonequilibrium dynamics of stochastic point processes with refractoriness. *Phys Rev E*, 82(2 Pt 1):021129–021129, 2010.

M. Deger, M. Helias, C. Boucsein, and S. Rotter. Statistical properties of superimposed stationary spike trains. *J Comput Neurosci*, 2011. doi: 10.1007/s10827-011-0362-8.

M. Dyson, G. Klump, and B. Gauger. Absolute hearing thresholds and critical masking ratios in the european barn owl: a comparison with other owls. *Journal of Comparative Physiology A*, 182(5): 695–702, 1998.

G. T. Einevoll, K. H. Pettersen, A. Devor, I. Ulbert, E. Halgren, and A. M. Dale. Laminar population analysis: estimating firing rates and evoked synaptic activity from multielectrode recordings in rat barrel cortex. *J Neurophysiol*, 97(3):2174–2190, 2007.

D. R. Euston and T. T. Takahashi. From spectrum to space: the contribution of level difference cues to spatial receptive fields in the barn owl inferior colliculus. *J. Neurosci.*, 22:284–293, 2002.

B. J. Fischer and J. L. Peña. Bilateral matching of frequency tuning in neural cross-correlators of the owl. *Biological cybernetics*, 100(6):521–531, Jun 2009.

F. P. Fischer. Quantitative tem analysis of the barn owl basilar papilla. *Hear Res*, 73(1):1–15, 1994.

W. J. Freeman, L. J. Rogers, M. D. Holmes, and D. L. Silbergeld. Spatial spectral analysis of human electrocorticograms including the alpha and gamma bands. *J Neurosci Methods*, 95(2):111–121, 2000.

P. A. Fuchs. Time and intensity coding at the hair cell's ribbon synapse. *The Journal of Physiology*, 566 (1):7–12, 2005.

I. Fukui and H. Ohmori. Tonotopic gradients of membrane and synaptic properties for neurons of the chicken nucleus magnocellularis. *J Neurosci*, 24(34):7514–23, 2004.

I. Fukui, R. M. Burger, H. Ohmori, and E. W. Rubel. Gabaergic inhibition sharpens the frequency tuning and enhances phase locking in chicken nucleus magnocellularis neurons. *Journal of Neuroscience*, 30 (36):12075–12083, 2010.

K. Funabiki and M. Konishi. Intracellular study of auditory coincidence detector neurons in owls. *Assoc Res Otolaryngol Abs*, 43, 2005.

K. Funabiki, K. Koyano, and H. Ohmori. The role of GABAergic inputs for coincidence detection in the neurones of nucleus laminaris of the chick. *J Physiol*, 508 ( Pt 3):851–69, May 1998.

K. Funabiki, G. Ashida, and M. Konishi. Computation of interaural time difference in the owl's coincidence detector neurons. *J Neurosci*, 31(43):15245–15256, 2011.

S. Gabriel, R. W. Lau, and C. Gabriel. The dielectric properties of biological tissues: Ii. measurements in the frequency range 10 hz to 20 ghz. *Phys Med Biol*, 41(11):2251–2269, 1996.

R. Galambos, J. Schwartzkopff, and A. Rupert. Microelectrode study of superior olivary nuclei. *Am J Physiol*, 197:527–36, 1959.

E. E. Galindo-Leon and R. C. Liu. Predicting stimulus-locked single unit spiking from cortical local field potentials. *J Comput Neurosci*, 29(3):581–597, 2010.

L. Gammaitoni, P. Hänggi, P. Jung, and F. Marchesoni. Stochastic resonance. *Rev Mod Phys*, 70: 223–287, 1998.

W. Gerstner, R. Kempter, J. van Hemmen, and H. Wagner. A neuronal learning rule for sub-millisecond temporal coding. *Nature*, 383:76–81, 1996.

C. Gold, D. A. Henze, C. Koch, and G. Buzsáki. On the origin of the extracellular action potential waveform: A modeling study. *Journal of Neurophysiology*, 95(5):3113–28, May 2006.

C. Gold, D. A. Henze, and C. Koch. Using extracellular action potential recordings to constrain compartmental models. *J Comput Neurosci*, 23(1):39–58, 2007.

J. M. Goldberg and P. B. Brown. Response of binaural neurons of dog superior olivary complex to dichotic tonal stimuli: some physiological mechanisms of sound localization. *J Neurophysiol*, 32(4): 613–36, Jul 1969.

N. Golding, D. Robertson, and D. Oertel. Recordings from slices indicate that octopus cells of the cochlear nucleus detect coincident firing of auditory nerve fibers with temporal precision. *J Neurosci*, 15:3138–3153, 1995.

B. Grothe. New roles for synaptic inhibition in sound localization. *Nat Rev Neurosci*, 4(7):540–50, 2003.

B. Grothe and T. J. Park. Sensitivity to interaural time differences in the medial superior olive of a small mammal, the mexican free-tailed bat. *J Neurosci*, 18(16):6608–22, 1998.

J. Guinan, B. Norris, and S. Guinan. Single auditory units in the superior olivary complex: Ii: Locations of unit categories and tonotopic organization. *International Journal of Neuroscience*, 4(4):147–166, 1972.

W. M. Harmening, M. A. Vobig, P. Walter, and H. Wagner. Ocular aberrations in barn owl eyes. *Vision Res*, 47(23):2934–42, 2007.

N. S. Harper and D. McAlpine. Optimal neural population coding of an auditory spatial cue. *Nature*, 430(7000):682–6, 2004.

K. D. Harris, D. A. Henze, J. Csicsvari, H. Hirase, and G. Buzsáki. Accuracy of tetrode spike separation as determined by simultaneous intracellular and extracellular measurements. *J Neurophysiol*, 84(1): 401–14, 2000.

J. A. Henrie and R. Shapley. Lfp power spectra in v1 cortex: the graded effect of stimulus contrast. *J Neurophysiol*, 94(1):479–90, 2005.

D. A. Henze, Z. Borhegyi, J. Csicsvari, A. Mamiya, K. D. Harris, and G. Buzsáki. Intracellular features predicted by extracellular recordings in the hippocampus in vivo. *J Neurophysiol*, 84(1):390–400, 2000.

N. Hohn and A. N. Burkitt. Shot noise in the leaky integrate-and-fire neuron. *Physical review E, Statistical, nonlinear, and soft matter physics*, 63(3 Pt 1):031902, Mar 2001.

G. R. Holt. *A critical reexamination of some assumptions and implications of cable theory in neurobiology.* PhD thesis, California Institute of Technology, 1998.

G. R. Holt and C. Koch. Electrical interactions via the extracellular potential near cell bodies. *Journal of Computational Neuroscience*, 6:169–184, 1999.

D. Horvath and N. A. Lesica. The effects of interaural time difference and intensity on the coding of low-frequency sounds in the mammalian midbrain. *J Neurosci.*, 31(10):3821—3827, 2011.

J. Hursh. Conduction velocity and diameter of nerve fibers. *Am J Physiol*, 127:131–139, 1939.

J. M. Hurtado, L. L. Rubchinsky, and K. A. Sigvardt. Statistical method for detection of phase-locked episodes in neural oscillations. *J Neurophys*, 91:1883–1898, 2004.

S. R. Jammalamadaka and A. SenGupta. *Topics in circular statistics*. World Scientific, Singapur, 1st edition, 2001.

L. A. Jeffress. A place theory of sound localization. *J Comp Physiol Psychol*, 41(1):35–39, 1948.

S. Jhaveri and D. K. Morest. Neuronal architecture in nucleus magnocellularis of the chicken auditory system with observations on nucleus laminaris: a light and electron microscope study. *Neuroscience*, 7(4):809–36, 1982.

P. X. Joris, P. H. Smith, and T. C. T. Yin. Coincidence detection in the auditory system: 50 years after Jeffress. *Neuron*, 21(6):1235–8, Dec. 1998.

P. X. Joris, B. van de Sande, and M. van der Heijden. Temporal damping in response to broadband noise. i. inferior colliculus. *J Neurophysiol*, 4(93):1857–70, 2005.

P. X. Joris, B. van de Sande, D. H. Louage, and M. van der Heijden. Binaural and cochlear disparities. *Proc Natl Acad Sci USA*, 103(34):12917–22, 2006.

E. Juergens, A. Guettler, and R. Eckhorn. Visual stimulation elicits locked and induced gamma oscillations in monkey intracortical- and eeg-potentials, but not in human eeg. *Experimental brain research Experimentelle Hirnforschung Expérimentation cérébrale*, 129(2):247–59, 1999.

Y. Kajikawa and C. E. Schroeder. How local is the local field potential? *Neuron*, 72(5):847–858, 2011.

S. Katzner, I. Nauhaus, A. Benucci, V. Bonin, D. L. Ringach, and M. Carandini. Local origin of field potentials in visual cortex. *Neuron*, 61(1):35–41, 2009.

C. H. Keller, K. Hartung, and T. T. Takahashi. Head-related transfer functions of the barn owl: measurement and neural responses. *Hear Res*, 118(1–2):13–34, 1998.

R. Kempter, W. Gerstner, J. L. van Hemmen, and H. Wagner. Temporal coding in the sub-millisecond range: Model of barn owl auditory pathway. In D. S. Touretzky, M. C. Mozer, and M. E. Hasselmo, editors, *Advances in Neural Information Processing Systems 8*, pages 124–130. MIT Press, Cambridge, MA, 1996.

R. Kempter, W. Gerstner, and J. L. van Hemmen. How the threshold of a neuron determines its capacity for coincidence detection. *Biosystems*, 48(1–3):105–12, 1998a.

R. Kempter, W. Gerstner, J. L. van Hemmen, and H. Wagner. Extracting oscillations. neuronal coincidence detection with noisy periodic spike input. *Neural computation*, 10(8):1987–2017, 1998b.

R. Kempter, C. Leibold, H. Wagner, and J. L. van Hemmen. Formation of temporal-feature maps by axonal propagation of synaptic learning. *Proc Natl Acad Sci U S A*, 98(7):4166–71, Mar. 2001.

D. Kernell and B. Zwaagstra. Input conductance axonal conduction velocity and cell size among hindlimb motoneurones of the cat. *Brain Res*, 204(2):311–26, 1981.

D. Khimich, R. Nouvian, R. Pujol, S. T. Dieck, A. Egner, E. D. Gundelfinger, and T. Moser. Hair cell synaptic ribbons are essential for synchronous auditory signalling. *Nature*, 434(7035):889–94, 2005.

N. Y.-S. Kiang. *Discharge Patterns of Single Fibers in the Cat's Auditory Nerve*. MIT Press, Cambridge, Massachusetts, 1965.

E. Knudsen and M. Konishi. Mechanisms of sound localization in the barn owl (tyto alba). *Journal of Comparative Physiology A*, 133(1):13–21, 1979.

E. Knudsen, G. Blasdel, and M. Konishi. Sound localization by the barn owl (Tyto alba) measured with the search coil technique. *Journal of Comparative Physiology A*, 133(1):1–11, 1979.

E. I. Knudsen and M. Konishi. A neural map of auditory space in the owl. *Science*, 200(4343):795–7, 1978a.

E. I. Knudsen and M. Konishi. Space and frequency are represented separately in auditory midbrain of the owl. *J Neurophysiol*, 41(4):870–884, 1978b.

M. Konishi. Study of sound localization by owls and its relevance to humans. *Comp Biochem Physiol, Part A Mol Integr Physiol*, 126(4):459–69, 2000.

M. Konishi, W. E. Sullivan, and T. Takahashi. The owl's cochlear nuclei process different sound localization cues. *J Acoust Soc Am*, 78(1 Pt 2):360–4, July 1985.

C. Köppl. Auditory nerve terminals in the cochlear nucleus magnocellularis: differences between low and high frequencies. *J Comp Neurol*, 339(3):438–46, Jan. 1994.

C. Köppl. Frequency tuning and spontaneous activity in the auditory nerve and cochlear nucleus magnocellularis of the barn owl Tyto alba. *J Neurophysiol*, 77(1):364–77, 1997a.

C. Köppl. Phase locking to high frequencies in the auditory nerve and cochlear nucleus magnocellularis of the barn owl, Tyto alba. *J Neurosci*, 17(9):3312–21, 1997b.

C. Köppl and C. E. Carr. Low-frequency pathway in the barn owl's auditory brainstem. *J Comp Neurol*, 378(2):265–82, Feb. 1997.

C. Köppl and C. E. Carr. Maps of interaural time difference in the chicken's brainstem nucleus laminaris. *Biological cybernetics*, 98(6):541–59, Jun 2008.

C. Köppl and G. Yates. Coding of sound pressure level in the barn owl's auditory nerve. *J Neurosci*, 19 (21):9674–86, 1999.

C. Köppl, O. Gleich, and G. Manley. An auditory fovea in the barn owl cochlea. *Journal of Comparative Physiology A: Neuroethology, Sensory, Neural, and Behavioral Physiology*, 171(6):695–704, 1993.

H. Kuba, R. Yamada, I. Fukui, and H. Ohmori. Tonotopic specialization of auditory coincidence detection in nucleus laminaris of the chick. *J Neurosci*, 25(8):1924–34, Feb. 2005.

H. Kuba, T. Ishii, and H. Ohmori. Axonal site of spike initiation enhances auditory coincidence detection. *Nature*, 444(7122):1069–1072, 2006.

M. F. Kubke, D. P. Massoglia, and C. E. Carr. Bigger brains or bigger nuclei? regulating the size of auditory structures in birds. *Brain, Behavior and Evolution*, 69:169–180, 2004.

L. Kuhlmann, A. Burkitt, A. Paolini, and G. M. Clark. Summation of spatiotemporal input patterns in leaky integrate-and-fire neurons: application to neurons in the cochlear nucleus receiving converging auditory nerve fiber input. *J Comput Neurosci*, 12:55–73, 2002.

P. T. Kuokkanen, H. Wagner, C. E. Carr, and R. Kempter. Modelling and analysis of the neurophonic potential in the laminar nucleus of the barn owl. In *Conference abstract*, volume 39, page 259. Society for Neuroscience, 2009.

P. T. Kuokkanen, H. Wagner, G. Ashida, C. E. Carr, and R. Kempter. On the origin of the extracellular field potential in the nucleus laminaris of the barn owl (tyto alba). *J Neurophysiol*, 104(4):2274–2290, 2010.

P. T. Kuokkanen, H. Wagner, C. E. Carr, and R. Kempter. Waveform summation in the owl's brainstem. *In preparation*, 2012.

H. Kushida. A study of cellular swelling and shrinkage during fixation, dehydration and embedding in various standard media. *J Electron Microsc*, 11:135–138, 1962.

E. A. Lachica, R. Rübsamen, and E. W. Rubel. Gabaergic terminals in nucleus magnocellularis and laminaris originate from the superior olivary nucleus. *J Comp Neurol*, 348(3):403–18, 1994.

N. Lautemann, P. T. Kuokkanen, R. Kempter, and H. Wagner. The neurophonic potential in the nucleus laminaris of birds. In *Proc of 6th MEA Meeting*, pages 63–64. MEA Organization, 2008.

C. Leibold, R. Kempter, and J. van Hemmen. Temporal map formation in the barn owl's brain. *Phys Rev Lett*, 87(24):248101, Jan 2001a.

C. Leibold, R. Kempter, H. Wagner, and J. van Hemmen. An interaural time difference map resulting from axonal selection through non-specific learning. *Neurocomputing*, 38:1401–1407, 2001b.

C. Leibold, R. Kempter, and J. L. van Hemmen. How spiking neurons give rise to a temporal-feature map: from synaptic plasticity to axonal selection. *Phys Rev E Stat Nonlin Soft Matter Phys*, 65(5 Pt 1):051915, May 2002.

H. Lindén, K. H. Pettersen, and G. T. Einevoll. Intrinsic dendritic filtering gives low-pass power spectra of local field potentials. *J Comput Neurosci*, 29(3):423–444, 2010.

H. Lindén, T. Tetzlaff, T. C. Potjans, K. H. Pettersen, S. Grün, M. Diesmann, and G. T. Einevoll. Modeling the spatial reach of the LFP. *Neuron*, 72(5):859–872, 2011.

B. Lindner. Superposition of many independent spike trains is generally not a poisson process. *Phys Rev E Stat Nonlin Soft Matter Phys*, 73(2 Pt 1):022901–022901, 2006.

B. Lindner, D. Gangloff, A. Longtin, and J. E. Lewis. Broadband coding with dynamic synapses. *J Neurosci*, 29:2076–2088, 2009.

N. K. Logothetis and B. A. Wandell. Interpreting the bold signal. *Annu Rev Physiol*, 66:735–769, 2004.

N. K. Logothetis, J. Pauls, M. Augath, T. Trinath, and A. Oeltermann. Neurophysiological investigation of the basis of the fmri signal. *Nature*, 412(6843):150–7, 2001.

N. K. Logothetis, C. Kayser, and A. Oeltermann. In vivo measurement of cortical impedance spectrum in monkeys: implications for signal propagation. *Neuron*, 55(5):809–23, 2007.

R. Lorente de Nó. A study of nerve physiology. *Studies from the Rockefeller Institute*, 131 and 132, 1947.

J. Malmivuo and R. Plonsey. *Bioelectromagnetism, Principles and Applications of Bioelectric and Biomagnetic Fields*. Oxford University Press, New York - Oxford, 1. edition, 1995.

P. B. Manis and S. O. Marx. Outward currents in isolated ventral cochlear nucleus neurons. *J Neurosci*, 11(9):2865–80, Sept. 1991.

G. A. Manley. Preferred intervals in the spontaneous activity of primary auditory neurons. *Naturwissenschaften*, 66(11):582–584, 1979.

J. T. Marsh, F. G. Worden, and J. C. Smith. Auditory frequency-following response: neural or artifact? *Science*, 169(951):1222–3, Sep 1970.

J. T. Marsh, W. S. Brown, and J. C. Smith. Differential brainstem pathways for the conduction of auditory frequency-following responses. *Electroencephalogr Clin Neurophysiol*, 36(4):415–24, Apr 1974.

J. A. Mazer. How the owl resolves auditory coding ambiguity. *Proc Natl Acad Sci USA*, 95(18):10932–7, 1998.

M. Mc Laughlin, M. van der Heijden, and P. X. Joris. Phase shifts in monaural field potentials of the medial superior olive. In E. A. Lopez-Poveda, A. R. Palmer, and R. Meddis, editors, *The Neurophysiological Bases of Auditory Perception*, pages 367–378. Springer New York, 2010a.

M. Mc Laughlin, E. Verschooten, and P. X. Joris. Oscillatory dipoles as a source of phase shifts in field potentials in the mammalian auditory brainstem. *Journal of Neuroscience*, 30(40):13472–13487, 2010b.

D. McAlpine. Creating a sense of auditory space. *The Journal of Physiology*, 566(Pt 1):21–8, Jul 2005.

B. McNamara and K. Wiesenfeld. Theory of stochastic resonance. *Phys Rev A*, 39:4854–4869, 1989.

U. Mitzdorf. Current source-density method and application in cat cerebral cortex: investigation of evoked potentials and EEG phenomena. *Physiol Rev*, 65(1):37–100, 1985.

A. Moiseff. Binaural disparity cues available to the barn owl for sound localization. *J Comp Physiol A*, 164(5):629–36, 1989a.

A. Moiseff. Bi-coordinate sound localization by the barn owl. *J Comp Physiol A*, 164(5):637–44, 1989b.

A. Moiseff and M. Konishi. Neuronal and behavioral sensitivity to binaural time differences in the owl. *J Neurosci*, 1(1):40–8, 1981.

A. Moiseff and M. Konishi. Binaural characteristics of units in the owl's brainstem auditory pathway: precursors of restricted spatial receptive fields. *J Neurosci*, 3(12):2553–62, 1983.

P. Monsivais, L. Yang, and E. W. Rubel. Gabaergic inhibition in nucleus magnocellularis: implications for phase locking in the avian auditory brainstem. *J Neurosci*, 20(8):2954–63, 2000.

G. Moushegian, A. Rupert, and M. A. Whitcomb. Brain-stem neuronal response patterns to monaural and binaural tones. *J Neurophysiol*, 27:1174–91, 1964.

G. Moushegian, A. L. Rupert, and J. S. Gidda. Functional characteristics of superior olivary neurons to binaural stimuli. *J Neurophysiol*, 38(5):1037–48, 1975.

K. I. Nagel and R. I. Wilson. Biophysical mechanisms underlying olfactory receptor neuron dynamics. *Nat Neurosci*, 14(2):208–216, 2011.

M. J. Nelson and P. Pouget. Do electrode properties create a problem in interpreting local field potential recordings? *J Neurophysiol*, 103(5):2315–2317, 2010.

H. Neubauer, C. Köppl, and P. Heil. Spontaneous activity of auditory nerve fibers in the barn owl (Tyto alba): analyses of interspike interval distributions. *J Neurophysiol*, 101(6):3169–91, 2009.

C. Nicholson and J. A. Freeman. Theory of current source-density analysis and determination of conductivity tensor for anuran cerebellum. *J Neurophysiol*, 38(2):356–368, 1975.

A. A. Nikonov, J. M. Parker, and J. Caprio. Odorant-induced olfactory receptor neural oscillations and their modulation of olfactory bulbar responses in the channel catfish. *The Journal of Neuroscience*, 22(6):2352–2362, 2002.

E. Nishino, R. Yamada, H. Kuba, H. Hioki, T. Furuta, T. Kaneko, and H. Ohmori. Sound-intensity-dependent compensation for the small interaural time difference cue for sound source localization. *J Neurosci*, 28(28):7153–64, 2008.

R. Norberg. Occurrence and independent evolution of bilateral ear asymmetry in owls and implications on owl taxonomy. *Phil Trans Roy Soc London B*, 280(973):375–408, 1977.

A. Novikov, E. Novikov, D. Shannahoff-Khalsa, B. Schwartz, and J. Wright. Scale-similar activity in the brain. *Phys. Rev. E*, 56(3):R2387–R2389, 1997.

P. L. Nunez and R. Srinivasan. *Electric fields of the brain: the neurophysics of EEG*. Oxford University Press, New York, NY, 2006.

D. Oertel. Synaptic responses and electrical properties of cells in brain slices of the mouse anteroventral cochlear nucleus. *J Neurosci*, 3(10):2043–53, 1983.

D. Oertel, R. Bal, S. M. Gardner, P. H. Smith, and P. X. Joris. Detection of synchrony in the activity of auditory fibers by octopus cells of the mammalian cochlear nucleus. *Proc Natl Acad Sci USA*, 97: 11773–11779, 2000.

E. M. Overholt, E. W. Rubel, and R. L. Hyson. A circuit for coding interaural time differences in the chick brainstem. *J Neurosci*, 12(5):1698–708, May 1992.

A. Papoulis and S. Pillai. *Probability, random variables, and stochastic processes*. McGraw-Hill electrical and electronic engineering series. McGraw-Hill, 2002. ISBN 9780073660110.

R. S. Payne. Acoustic location of prey by barn owls (tyto alba). *J Exp Biol*, 54(3):535–73, 1971.

J. L. Pena and W. M. DeBello. Auditory processing, plasticity, and learning in the barn owl. *ILAR J*, 51(4):338–52, 2010.

J. L. Peña and M. Konishi. Cellular mechanisms for resolving phase ambiguity in the owl's inferior colliculus. *Proc Natl Acad Sci USA*, 97(22):11787–92, 2000.

J. L. Peña, S. Viete, Y. Albeck, and M. Konishi. Tolerance to sound intensity of binaural coincidence detection in the nucleus laminaris of the owl. *J Neurosci*, 16(21):7046–54, Nov 1996.

J. L. Peña, S. Viete, K. Funabiki, K. Saberi, and M. Konishi. Cochlear and neural delays for coincidence detection in owls. *J Neurosci*, 21(23):9455–9, Dec 2001.

K. H. Pettersen and G. T. Einevoll. Amplitude variability and extracellular low-pass filtering of neuronal spikes. *Biophys J*, 94(3):784–802, 2008.

K. H. Pettersen, A. Devor, I. Ulbert, A. M. Dale, and G. T. Einevoll. Current-source density estimation based on inversion of electrostatic forward solution: effects of finite extent of neuronal activity and conductivity discontinuities. *J Neurosci Methods*, 154(1–2):116–133, 2006.

K. H. Pettersen, E. Hagen, and G. T. Einevoll. Estimation of population firing rates and current source densities from laminar electrode recordings. *J Comput Neurosci*, 24(3):291–313, 2008.

K. H. Pettersen, H. Lindén, A. M. Dale, and G. T. Einevoll. Extracellular spikes and current-source density. In R. Brette and A. Destexhe, editors, *Handbook of neural activity measurements*. Cambridge University Press, Cambridge, UK, 2010.

I. Poganiatz, I. Nelken, and H. Wagner. Sound-localization experiments with barn owls in virtual space: influence of interaural time difference on head-turning behavior. *J Assoc Res Otolaryngol*, 2(1):1–21, 2001.

L. Proctor and M. Konishi. Representation of sound localization cues in the auditory thalamus of the barn owl. *Proc Natl Acad Sci USA*, 94(19):10421–5, 1997.

W. Rall. Electrophysiology of a dendritic neuron model. *Biophys J*, 2(2 Pt 2):145–67, Mar 1962.

M. Rasch, N. K. Logothetis, and G. Kreiman. From neurons to circuits: linear estimation of local field potentials. *J Neurosci*, 29(44):13785–1396, 2009.

A. D. Reyes, E. W. Rubel, and W. J. Spain. Membrane properties underlying the firing of neurons in the avian cochlear nucleus. *J Neurosci*, 14(9):5352–64, 1994.

A. D. Reyes, E. W. Rubel, and W. J. Spain. In vitro analysis of optimal stimuli for phase-locking and time-delayed modulation of firing in avian nucleus laminaris neurons. *J Neurosci*, 16(3):993–1007, Feb. 1996.

E. W. Rubel and T. N. Parks. Organization and development of brain stem auditory nuclei of the chicken: tonotopic organization of n. magnocellularis and n. laminaris. *J Comp Neurol*, 164(4):411–33, 1975.

D. W. Schwarz. Can central neurons reproduce sound waveforms? An analysis of the neurophonic potential in the laminar nucleus of the chicken. *The Journal of otolaryngology*, 21(1):30–38, Feb 1992a.

D. W. Schwarz. Sound delay lines in the nucleus laminaris of the chicken. *The Journal of otolaryngology*, 21(3):202–208, Jun 1992b.

L. L. Scott, P. J. Mathews, and N. L. Golding. Posthearing developmental refinement of temporal processing in principal neurons of the medial superior olive. *J Neurosci*, 25:7887–7895, 2005.

L. L. Scott, P. J. Mathews, and N. L. Golding. Perisomatic voltage-gated sodium channels actively maintain linear synaptic integration in principal neurons of the medial superior olive. *J Neurosci*, 30: 2039–2050, 2010.

T. Shimokawa, K. Pakdaman, and S. Sato. Time-scale matching in the response of a leaky integrate-and-fire neuron model to periodic stimulus with additive noise. *Phys Rev E*, 59:3427–3443, 1999.

M. Siegel and P. König. A functional gamma-band defined by stimulus-dependent synchronization in area 18 of awake behaving cats. *J Neurosci*, 23(10):4251–60, 2003.

M. Singheiser, B. J. Fischer, and H. Wagner. Estimated cochlear delays in low best-frequency neurons in the barn owl cannot explain coding of interaural time difference. *J Neurophysiol*, 104(4):1946–1954, 2010.

S. J. Slee, M. H. Higgs, A. L. Fairhall, and W. J. Spain. Tonotopic tuning in a sound localization circuit. *J Neurophysiol*, 103(5):2857–75, 2010.

D. J. Smith and E. W. Rubel. Organization and development of brain stem auditory nuclei of the chicken: dendritic gradients in nucleus laminaris. *J Comp Neurol*, 186(2):213–39, Jul 1979.

D. L. Snyder and M. I. Miller. *Random point processes in time and space.* Springer, New York, NY, 1991.

R. L. Snyder and C. E. Schreiner. The auditory neurophonic: basic properties. *Hear Res*, 15(3):261–80, Sep 1984.

M. W. Spitzer and M. N. Semple. Neurons sensitive to interaural phase disparity in gerbil superior olive: diverse monaural and temporal response properties. *J Neurophys*, 73:1668–1690, 1995.

W. E. Sullivan and M. Konishi. Segregation of stimulus phase and intensity coding in the cochlear nucleus of the barn owl. *J Neurosci*, 4(7):1787–99, July 1984.

W. E. Sullivan and M. Konishi. Neural map of interaural phase difference in the owl's brainstem. *Proc Natl Acad Sci USA*, 83(21):8400–4, 1986.

T. Takahashi and M. Konishi. Selectivity for interaural time difference in the owl's midbrain. *J Neurosci*, 6(12):3413–22, 1986.

T. Takahashi, A. Moiseff, and M. Konishi. Time and intensity cues are processed independently in the auditory system of the owl. *J Neurosci*, 4(7):1781–6, 1984.

T. T. Takahashi and M. Konishi. Projections of the cochlear nuclei and nucleus laminaris to the inferior colliculus of the barn owl. *J Comp Neurol*, 274(2):190–211, 1988a.

T. T. Takahashi and M. Konishi. Projections of nucleus angularis and nucleus laminaris to the lateral lemniscal nuclear complex of the barn owl. *J Comp Neurol*, 274(2):212–38, Aug. 1988b.

Y. Takahashi and M. Konishi. Manipulation of inhibition in the owl's nucleus laminaris and its effects on optic tectum neurons. *Neuroscience*, 111(2):373–8, 2002.

R. Tokioka, H. Kawaguchi, and K. Fukunishi. Spatio-temporal analyses of stimulus-evoked and spontaneous stochastic neural activity observed by optical imaging in guinea pig auditory cortex. *Brain Research*, 861(2):271 – 280, 2000.

S. M. Tomchik and Z. Lu. Modulation of auditory signal-to-noise ratios by efferent stimulation. *J Neurophysiol*, 95:3562–3570, 2006.

L. O. Trussell. Synaptic mechanisms for coding timing in auditory neurons. *Annu. Rev. Physiol.*, 61: 477–96, 1999.

S. Viete, J. L. Peña, and M. Konishi. Effects of interaural intensity difference on the processing of interaural time difference in the owl's nucleus laminaris. *J Neurosci*, 17(5):1815–24, Mar. 1997.

K. Vonderschen and H. Wagner. Tuning to interaural time difference and frequency differs between the auditory arcopallium and the external nucleus of the inferior colliculus. *J Neurophysiol.*, 101(5): 2348–61, 2009.

H. Wagner. On the ability of neurons in the barn owl's inferior colliculus to sense brief appearances of interaural time difference. *J Comp Physiol A*, 170(1):3–11, 1992.

H. Wagner, T. Takahashi, and M. Konishi. Representation of interaural time difference in the central nucleus of the barn owl's inferior colliculus. *J Neurosci*, 7(10):3105–16, Oct. 1987.

H. Wagner, S. Brill, R. Kempter, and C. E. Carr. Microsecond precision of phase delay in the auditory system of the barn owl. *J Neurophysiol*, 94(2):1655–8, 2005.

H. Wagner, S. Brill, R. Kempter, and C. E. Carr. Auditory responses in the barn owl's nucleus laminaris to clicks: impulse response and signal analysis of neurophonic potential. *J Neurophysiol*, 102(2): 1227–40, 2009.

N. M. Weinberger, L. M. Kitzes, and D. A. Goodman. Some characteristics of the "auditory neurophonic". *Experientia*, 26(1):46–8, Jan 1970.

J. S. Wernick and A. Starr. Binaural interaction in the superior olivary complex of the cat: an analysis of field potentials evoked by binaural-beat stimuli. *J Neurophys*, 31:428–441, 1968.

E. G. Wever and C. W. Bray. Action currents in the auditory nerve in response to acoustical stimulation. *Proc Natl Acad Sci USA*, 16(5):344–50, May 1930.

K. Wiesenfeld, D. Pierson, E. Pantazelou, C. Dames, and F. Moss. Stochastic resonance on a circle. *Phys Rev Lett*, 72:2125–2129, 1994.

J. A. Winer and D. T. Larue. GABA and glycine in the auditory thalamus and midbrain of the barn owl (Tyto alba). *Soc. Neurosci. Abstr.*, 22:1069, 1996.

P. Winter and J. Schwartzkopff. [Form and cell number of the acoustic nerve center in the medulla oblongata of the owl (Striges).]. *Experientia*, 17:515–6, 1961.

C. Wirth and H.-R. Lüscher. Spatiotemporal evolution of excitation and inhibition in the rat barrel cortex investigated with multielectrode arrays. *J Neurophysiol*, 91(4):1635–47, Apr. 2004.

F. G. Worden and J. T. Marsh. Frequency-following (microphonic-like) neural responses evoked by sound. *Electroencephalogr Clin Neurophysiol*, 25(1):42–52, 1968.

S. H. Wu. Physiological properties of neurons in the ventral nucleus of the lateral lemniscus of the rat: intrinsic membrane properties and synaptic responses. *J Neurophysiol*, 81(6):2862–2874, 1999.

D. Xing, C.-I. Yeh, and R. M. Shapley. Spatial spread of the local field potential and its laminar variation in visual cortex. *J. Neurosci.*, 29:11540–11549, 2009.

L. Yang, P. Monsivais, and E. W. Rubel. The superior olivary nucleus and its influence on nucleus laminaris: a source of inhibitory feedback for coincidence detection in the avian auditory brainstem. *J Neurosci*, 19:2313–2325, 1999.

T. C. Yin and J. C. Chan. Interaural time sensitivity in medial superior olive of cat. *J Neurophysiol*, 64 (2):465–88, 1990.

T. C. Yin, L. H. Carney, and P. X. Joris. Interaural time sensitivity in the inferior colliculus of the albino cat. *J Comp Neurol*, 295(3):438–48, 1990.

J. H. Zar. *Biostatistical Analysis*. Prentice Hill, 4. edition, 1999.

S. Zhang and L. O. Trussell. Voltage clamp analysis of excitatory synaptic transmission in the avian nucleus magnocellularis. *J Physiol*, 480 ( Pt 1):123–36, Oct. 1994.

# List of Figures

# Acknowledgments

First and foremost, I thank Richard Kempter for excellent supervision, inspiring discussions, support and helpful feedback whenever needed. I furthermore thank Catherine E. Carr and Hermann Wagner for sharing their experimental data and their knowledge, and for the long insightful discussions.

I am thankful for the administrative and technical support of Margret Franke, Elvira Lauterbach and Andreas Hantschmann. For the structural and financial support of my work I thank the Institut for theoretical Biology, the Humboldt Universität zu Berlin and the Bernstein Center for Computational Neuroscience Berlin, as well as the BMBF (Bernstein Collaboration in Computational Neuroscience: Temporal Precision 01GQ07102; 01GQ0410 and 01GQ0972) and the DFG (Emmy Noether KE 788/1-4; Sonderforschungsbereich (SFB) 618 Theoretical Biology).

I thank Jose Donoso, Jorge Jaramillo, Anja Sieber, Urs Bergmann, Nikolay Chenkov and Franziska Witzel for the feedback considering this thesis.

I am grateful for helpful discussions and advise to my colleagues at ITB and elsewhere, including Roland Schaette, Robert Schmidt, Jose Donoso, Jorge Jaramillo, Nikolay Chenkov, Susanne Schreiber, Franziska Witzel, Lovisa Helgadottir, Sandra Brill, Nico Lautemann, Go Ashida, Yu Fukuda, Thomas Künzel, Jose Luis Peña, Christine Köppl and Farzad Farkhooi.

For their help in the process of writing this thesis I thank many good friends, including Patrick Flack, Nina Blom, Ruth Hendus-Altenburger, Andreas Altenburger and Ulrich Reinacher.

I am grateful to my beloved Anja and to my family for their support at all times, and to all my dear friends in Berlin and elsewhere for reminding me of the life besides science.

# Publikationsliste

## Paula Tuulia Kuokkanen

### Artikel

Kuokkanen PT, Wagner H, Ashida G, Carr CE, Kempter R (2010). On the origin of the extracellular field potential in the nucleus laminaris of the barn owl (Tyto alba). J. Neurophysiol. 104, 2274 – 2290

### Vorträge

Minisymposium für Current Source Density -Methoden, Advanced Cource for Computational Neuroscience, Bedlewo, Polen (August 2010). *Extracellular field potential in the nucleus laminaris of the barn owl*

International Conference for Physics Students, Coimbra, Portugal (August 2005). *On the Origin of Tinnitus*

### Ausgewählte Poster

Kuokkanen PT, Carr CE, Wagner H, Kempter R (2011). Origin of the neurophonic: linear summation of the monaural responses predicts the binaural response in the nucleus laminaris of the barn owl. Conference Abstract: 33th Göttingen Neurobiology Meeting

Kuokkanen PT, Carr CE, Wagner H, Kempter R (2010). Origin of the neurophonic: linear summation of the monaural responses predicts the binaural response in the nucleus laminaris of the barn owl. Frontiers in Computational Neuroscience. Conference Abstract: Bernstein Symposium 2010. doi: 10.3389/conf.fncom.2010.51.00011

Carr CE, Ashida G, Shah S, Brill S, Kuokkanen PT, Kempter R, Wagner H (2010). Neurophonic maps of ITD in nucleus laminaris of the barn owl. Conference abstract: 40th SFN Neuroscience Meeting, p. 480.18

Kuokkanen PT, Lautemann N, Carr CE, Wagner H, Kempter R (2009). Signal-to-noise ratio of the neurophonic potential in the laminar nucleus of the barn owl. Conference Abstract: BMC Neuroscience 2009, 10(Suppl 1):P243.

Lautemann N, Kuokkanen PT, Kempter R and Wagner H (2009). Multi-electrode recordings of delay lines in nucleus laminaris of the barn owl. Frontiers in Computational Neuroscience. Conference Abstract: Bernstein Symposium 2009.
doi: 10.3389/conf.neuro.10.2009.14.098

Lautemann N, Kuokkanen PT, Kempter R, Wagner H (2009). Delay lines in the auditory coincidence detector circuit of the barn owl. Conference abstract: 39th SFN Neuroscience Meeting

Kuokkanen PT, Wagner H, Carr CE, Kempter R (2009). Modelling and analysis of the neurophonic potential in the laminar nucleus of the barn owl. Conference abstract: 39th SFN Neuroscience Meeting

Kuokkanen PT, Lautemann N., Wagner H, Kempter R (2009). Analysis and simulation of the neurophonic potential in the laminar nucleus of the barn owl. Abstr. Ass. Res. Otolaryngol. 32:895

Wagner H, Brill S, Kempter R, Kuokkanen PT, Carr CE. (2009). Auditory responses in the owl's nucleus laminaris to clicks: impulse response and signal analysis of neurophonic responses. Abstr. Ass. Res. Otolaryngol. 32:856

Lautemann N, Kuokkanen PT, Kempter R, Wagner H. (2008). The neurophonic potential in nucleus laminaris of birds. Proceedings MEA Meeting, 82–83

Wagner H, Lautemann N, Kuokkanen PT, Kempter R, Carr CE (2008). Microsecond precision in the auditory system of birds: Delay lines in nucleus laminaris. FENS Abstr. Vol. 4 A087.16

Kuokkanen PT, Lautemann N, Wagner H, Kempter R (2007). Microsecond precision in the auditory system of birds. Bernstein Symposium for Computational Neuroscience, Goettingen. T19-8A

Kuokkanen PT, Schaette R, Kempter R (2006). Modeling the Activity of the Auditory Nerve after Hearing Loss, Berlin Neuroscience Forum

# Selbständigkeitserklärung

Ich erkläre, dass ich die vorliegende Arbeit selbständig und nur unter Verwendung der angegebenen Literatur und Hilfsmittel angefertigt habe.

Berlin, den 26.01.2012

(Paula T. Kuokkanen )